High time-resolution observations of convective cloud lifecycles

Sarah Ann Taylor

Oriel College

University of Oxford

A thesis submitted for the degree of

Master of Science by Research

Michaelmas Term 2017

To Chris

High time-resolution observations of convective cloud lifecycles

Sarah Ann Taylor, Oriel College

Submitted for the degree of Master of Science by Research, Michaelmas Term 2017

Abstract

Quantifying the variability of convective cloud is of fundamental importance in order to understand and accurately model global weather and climate systems. While broad features of the diurnal and lifecycles of convective cloud are understood, the spatial and temporal variability of convective properties are not well characterised on the global scale, particularly over large areas of Africa. Due to the complexity of the processes involved, models also struggle to realistically simulate the spatial and temporal variability of convective cloud.

Observations provide insight into the properties of convective cloud and valuable information about avenues for model development. Due to the wide range of spatial and temporal scales involved in convection, the continuous nature of observations from geostationary satellites makes them ideal for investigating convection. This study uses high temporal resolution data from the geostationary Spinning Enhanced Visible and Infrared Imager (SEVIRI) instrument to quantify seasonal and diurnal cycles of cloud top temperature (CTT) and the lifecycle of individually tracked convective clouds over a large area and period of time.

This study demonstrates that biases in SEVIRI CTT retrievals vary from less than 5 K over the southeast Atlantic Ocean, up to 30 K over central Africa at night, while biases can also differ by up to 30 K between night and daytime retrievals. This highlights the importance of considering spatial and diurnal variations in retrieval errors. Keeping these biases in mind, it is shown that the diurnal cycle of cloud tops is measured accurately in regions of stratiform cloud, while quantifying the diurnal cycle over the tropics and regions of desert is more difficult.

SEVIRI observations are used to track individual convective cloud cores and anvils across sub-Saharan Africa. The distributions, diurnal cycles, lifecycles and spatial and seasonal cycles of a number of properties are quantified. Horizontal core and anvil areas are shown to increase with longer cloud lifetimes, while minimum core CTTs are shown to decrease with cloud lifetime. The diurnal cycle in convective activity is shown to have both a morning and an evening peak, while the total anvil coverage peaks in the late afternoon. Seasonal and spatial variations in core and anvil area, CTT, time of convective initiation and dissipation are also quantified.

These results will be of interest to those in the observation and modelling communities, particularly for studies considering the diurnal cycle of convection, or developing new convective cloud process models and parameterisations.

Acknowledgements

I would like to take this opportunity to thank the many people who have helped to make this work possible.

Firstly I would like to thank my supervisor Philip Stier for his support and guidance, as well as Bethan White for all her helpful input.

I would also like to thank Tobias Zinner for his practical advice on use of his cloud tracking program. Stephan Finkensieper and Martin Stengel were of great help in providing access to and advice on the use of the CLAAS-2 cloud top properties dataset.

Finally I would like to thank past and present members of the Climate Processes group at AOPP for their support and for countless useful discussions, in particular Zak Kipling, Ed Gryspeerdt, Natalie Weigum, Max Heikenfeld, Nick Schutgens, Laurent Labbouz, and Duncan Watson-Parris.

Table of Contents

List of Abbreviations

AEJ	African easterly jet
AEW	African easterly wave
AMMA	African Monsoon Multidisciplinary Analyses
CALIOP	Cloud-Aerosol Lidar with Orthogonal Polarization
CALIPSO	Cloud-Aerosol Lidar and Infrared Pathfinder Satellite Observation
Cb-TRAM	Cumulonimbus TRacking And Monitoring
CCN	cloud condensation nuclei
CF	cloud fraction
CLAAS-2	CLoud property dAtAset using SEVIRI, version 2
CMSAF	Satellite Application Facility on Climate Monitoring
COD	cloud optical depth
CPR	cloud profiling radar
CRM	cloud resolving model
CTH	cloud top height
CTP	cloud top pressure
CTT	cloud top temperature
DJF	December, January and February
ECMWF	European Centre for Medium Range Weather Forecasting
EUMETSAT	European Organisation for the Exploitation of Meteorological Satellites
GEOS-5	Goddard Earth Observing System Model, Version 5
GOES-8	Geostationary Operational Environmental Satellite 8
GOES-R	Geostationary Operational Environmental Satellite - R series
GPCP	Global Precipitation Climatology Project
GPM	Global Precipitation Measurement
HRV	high resolution visible
IN	ice nuclei
ITCZ	intertropical convergence zone
JJA	June, July and August
LST	local solar time
MAM	March, April and May
MCS	mesoscale convective system
MODIS	Moderate Resolution Imaging Spectroradiometer
MSG	Meteosat Second Generation
NWCSAF	Satellite Application Facility on Nowcasting

PR	Precipitation Radar
RF	radiative forcing
RMSE	root mean squared error
RTTOV	Radiative Transfer Model for TOVS
SEVIRI	Spinning Enhanced Visible and Infrared Imager
SON	September, October and November
TC4	Tropical Composition, Cloud and Climate
TRMM	Tropical Rainfall Measuring Mission
VOCALS-REx	VAMOS Ocean-Cloud-Atmosphere-Land Study Regional Experiment

1 | Introduction

1.1 Motivation

Convective clouds are one of the core building blocks of tropical weather and climate. They play important roles in large-scale atmospheric circulations, the hydrological cycle, global energy budget and transport of heat, moisture, momentum, aerosols and trace gases throughout the troposphere (Grabowski and Petch 2009). Quantifying the temporal and spatial variability of convective cloud is therefore of fundamental importance in order to understand and accurately model global weather and climate systems.

However, while the broad features of the diurnal cycle and lifecycle of convective cloud, such as the phase of the diurnal cycle over land and ocean, some aspects of convective interaction with local geography, and simple models of convective cloud lifecycles are well understood, the spatial and temporal variability of convective properties are not well characterised on the global scale, particularly over large areas of Africa (Washington et al. 2013). Due to the complexity of the processes involved, general circulation and numerical weather prediction models also struggle to realistically simulate the spatial and temporal variability of cloud (Yang and Slingo 2001; Guichard et al. 2004; Grabowski et al. 2006; Stratton and Stirling 2012). In particular, they fail to capture the diurnal cycle of convection (Yang and Slingo 2001; Guichard et al. 2004; Grabowski et al. 2006; Stratton and Stirling 2012), with convection developing too early and rapidly (Guichard et al. 2004; Stratton and Stirling 2012). On the other hand, cloud resolving models (CRMs) which explicitly resolve convection and have grid scales of around 1 km or less have been shown to be capable of correctly simulating the diurnal cycle (Guichard et al. 2004; Grabowski et al. 2006; Sato et al. 2009).

Observations provide insights into these processes and allow us to consider various mechanisms by which convective cloud properties can be altered. They also give valuable information about avenues for the future development and validation of both convective cloud process models and convective parameterisations.

As spatial scales of convection range from thousands of kilometres for mesoscale convective system (MCS) to less than a kilometre for individual convective plumes, while time scales of convective variability range from minutes through to seasons, the continuous nature of observations from geostationary satellites makes them ideal for investigating the temporal and spatial variability of convection.

This thesis used high temporal resolution data from the geostationary Spinning Enhanced Visible and Infrared Imager (SEVIRI) instrument to quantify spatial and diurnal variability in cloud top temperature (CTT) retrieval biases, investigate seasonal and diurnal cycles of CTT and quantify the lifecycle of individually tracked deep convective clouds over large areas and periods of time.

1.2 Outline

Current scientific understanding of the physical properties of clouds and their importance for global weather and climate is reviewed in Chapter 2. A particular emphasis is placed on satellite observations of cloud properties and on observed properties of convective cloud. Chapter 3 uses high time-resolution data from SEVIRI to quantify the spatial, seasonal and diurnal variability of CTT, while considering the impact of satellite retrieval biases on our ability to accurately capture the details of this variability. Chapter 4 combines data from SEVIRI with cloud tracking software to study the evolution and lifecycle of convective clouds in a Lagrangian framework. A summary of the work presented in this thesis, including general conclusions and suggestions for further work are provided in Chapter 5.

1.3 Publications

The work presented in Chapter 3 of this thesis is based on a paper published in Atmospheric Chemistry and Physics (Taylor et al. 2017).

The work presented in Chapter 3 is my own. Philip Stier and Bethan White provided suggestions for the methodology and discussed results at all stages. Stephan Finkensieper and Martin Stengel developed the SEVIRI cloud top properties dataset and provided advice on its use.

2 | Scientific Background

This chapter aims to review current scientific understanding of the physical properties of clouds and the mechanisms by which they interact with the global climate system. The focus of the work presented in this thesis is satellite observations of convective cloud. More detailed descriptions of satellite observations of cloud properties and on observed properties of convective cloud are therefore given in Sections 2.2 and 2.3 respectively.

2.1 Clouds and climate

2.1.1 Radiative forcing

Clouds cover approximately 70% of the Earth's surface (Berthier et al. 2008) and are of fundamental importance to global climate. They alter the temperature of the Earth's atmosphere and surface by absorbing, reflecting and scattering radiation. The relative importance of the mechanisms through which clouds affect the Earth's climate can be compared using the concept of radiative forcing (RF). RF (measured in Wm^{-2}) is a measure of the impact that a change to any one process has on the Earth's radiation balance. In the case of clouds, it measures the difference between net short and longwave fluxes under clear and cloudy atmospheric conditions. A negative RF therefore indicates a net cooling effect due to the presence of clouds, while a positive RF indicates a net heating effect.

Solar and thermal radiation interacts with clouds due to the absorbing and scattering properties of these water droplets and ice crystals. Clouds account for around three-quarters of the Earth's albedo (Trenberth et al. 2009), with both high and low level clouds scattering shortwave radiation back into space. Optically thick clouds have a higher albedo and therefore have a larger cooling effect than optically thin clouds. The annual global mean shortwave cloud RF is estimated at approximately -50 Wm^{-2} (Boucher et al. 2013). Longwave radiation emitted at the Earth's surface is absorbed and re-emitted by cloud layers. The heating effect of high, cold clouds therefore tends to dominate in the longwave, leading to an annual global mean longwave RF of approximately +30 Wm^{-2} (Loeb et al. 2009; Boucher et al. 2013). While cloud RF varies seasonally, geographically and by cloud type, the net global mean cloud RF of -20 Wm^{-2} therefore indicates a net cooling effect from the presence of clouds (Loeb et al. 2009; Boucher et al. 2013).

However, the response of clouds to anthropogenic perturbations of the climate system remains a source of considerable uncertainty in our understanding of and ability to accurately model the global climate system (Bony et al. 2006; Boucher et al. 2013). In particular the magnitude of the effect of anthropogenic aerosols on cloud properties remains unknown (Norris and Slingo 2009; Forster et al. 2007).

2.1.2 Cloud formation

Clouds are formed when water vapour in the air condenses onto fine solid particles, or liquid droplets in the atmosphere called aerosols, forming either water droplets, or ice crystals (Seinfeld and Pandis 2006). Warm clouds consist of liquid water droplets formed by the condensation of water vapour onto aerosol particles called cloud condensation nuclei (CCN). Cold clouds consist of ice-crystals, formed by the freezing of water onto aerosol particles called ice nuclei (IN). Mixed-phase clouds can contain a mixture of ice crystals and supercooled water droplets.

In order for a cloud to form, it is necessary for a parcel of moist air to be cooled until it is sufficiently supersaturated to activate the available CCN or IN. Saturation vapour pressure varies with temperature. It occurs when the partial pressure of water vapour is in equilibrium with a flat surface, such that the fluxes of molecules escaping and returning to the liquid are equal (Seinfeld and Pandis 2006). An air parcel is defined as supersaturated when the vapour pressure of water in an air parcel is greater than the saturated vapour pressure.

It would therefore seem that cloud droplets should begin to form when the relative humidity is above 100%, since relative humidity is defined as the mixing ratio of a parcel over its saturation mixing ratio value. However, cloud droplets have curved surfaces, and the Kelvin effect (Thomson 1871) tells us that saturation vapour pressure over a curved surface is always higher than that over a flat surface. Supersaturations of more than 10% would therefore be required for water droplets to form under clean air conditions (Seinfeld and Pandis 2006). However, observed atmospheric supersaturations are typically less than 1%.

In order for cloud droplets to form in the atmosphere it is therefore necessary for aerosol particles to serve as CCN or IN onto which water vapour can condense. Raoult's Law states that the presence of dissolved materials lowers the saturation vapour pressure, enabling water droplets to be formed at lower supersaturations (Seinfeld and Pandis 2006).

Kohler theory combines the Kelvin and Raoult effects to calculate the saturation vapour pressure over solutions with a curved surface. It shows that, by acting as a solute and by increasing the size of the initial cloud droplet, aerosol particles can overcome the barriers to droplet formation, resulting in the spontaneous growth of cloud water droplets (Kohler 1936).

2.1.3 Convective cloud

Convective cloud is one of the core building blocks of tropical weather and climate, playing important roles in large-scale atmospheric circulations, the hydrological cycle, the global energy budget and the transport of heat, moisture, momentum, aerosols and trace gases throughout the troposphere (Grabowski and Petch 2009). The temporal and spatial variability of convective cloud are therefore of fundamental importance for global weather and climate systems.

As explained in section 2.1, cloud forms when water vapour condenses to form liquid water drops, or ice crystals. In the case of convective cloud, this condensation is instigated by the vertical motion of moist air rising through cooler air. The atmosphere in the tropics is homogeneous relative to the extratropics, with little change in air density or pressure (Galvin 2015). Convection can therefore be expected wherever there are warm surfaces, moist air and sufficient atmospheric instability to allow for the vertical motion of air parcels.

Shallow convection refers to convective cloud with a limited vertical extent. The tops of these clouds reach only a few kilometres above the surface. As they do not rise above the freezing level, they are made of water droplets only. However, some areas, particularly the equatorial Atlantic, receive most of their cloud cover and precipitation from such clouds (Galvin 2015). Shallow convection is found throughout the tropics, and these clouds are important for the role that they play in mixing heat and moisture throughout the lower troposphere.

Deep convective clouds extend vertically throughout the tropopause, rising well above the freezing level. They are mixed-phase clouds containing both liquid water droplets and ice crystals. Due to the efficient production of rain and hail by ice processes, these clouds bring heavy precipitation. They are also significant contributors to radiative forcing, due to the large areas of anvil cloud detrained once these storms reach the capping layer of the tropopause, which often persist long after the convective storm that generated them has dissipated. Deep convective storms bring intense circulations of air, with updrafts mixing heat and moisture into the upper troposphere and downdrafts bringing cooler and drier air to the surface.

A single cell convective storm is relatively short-lived, sometimes lasting for less than an hour (Galvin 2015). It goes through three main stages in its lifecycle. In the presence of warm and humid air at the surface, if the atmosphere is sufficiently unstable, a trigger, such as orographic lifting, convergence, or surface heating can cause surface air to rise. In the developing stage of its life, a cloud is formed due to the condensation of water vapour. This condensation releases latent heat, enhancing the buoyancy of the rising parcels. In the mature stage of its lifecycle, raindrops begin to form and fall through the cloud, bringing colder air to the surface. Once this cold air reaches the surface, it spreads outwards along the surface. In the dissipating stage, cold air from downdrafts eventually cuts off the supply of warm, moist air to the cloud, killing off the updrafts. The cloud may continue to rain for a while and will dissipate.

Multi-cell storms can be formed in the presence of vertical wind shear, where winds speeds and directions change with altitude. Under these conditions, the developing storm will be tilted vertically, so that the downdraft is skewed to the side of the convective updraft. In this case, when the downdraft hits the surface and spreads out, rather than cutting off the supply of warm moist air, it lifts the boundary layer air as it travels along the surface and may produce new convective cells. Depending on how the winds change with height, these storms may develop into self-generating multi-cell storms.

The largest of the convective cloud systems are MCS. These are generally defined as convective clouds which produce precipitation over an area of at least 100 km in any direction (Zipser 1969, 1977; Houze, R. A. 1993; Houze 2004). MCS are formed by the merging and organisation of smaller convective clouds to form a single cloud system with a large anvil area and several regions of convective updraft. MCS typically live for a few hours, up to days. They are longer-lived than other types of convection, move more slowly and produce more precipitation (Houze 2004). In addition to the important impact they have on the radiation budget and hydrological cycle, MCS are also linked to large-scale atmospheric circulations (Houze et al. 2000; Carbone et al. 2002). MCS are present in a greater magnitude and intensity over tropical continental regions, while in oceanic and subtropical regions they are the major contributors to observed precipitation (Zipser 2003).

Seasonal patterns in tropical convection are largely driven by the movement of the intertropical convergence zone (ITCZ), a region of convergence between trade winds in the southern and northern hemispheres, which is often seen on satellite images as a band of convective cloud (Waliser and Gautier 1993; Yang and Slingo 2001; Schröder et al. 2009). It forms the ascending branch of the Hadley cells, and so is collocated with maximum solar insolation, displaying a distinct annual cycle, moving north and south of the equator throughout the year (Fig. 2.1). However, the exact nature of the ITCZ is still a matter of debate. It is not a permanent band of cloud encircling the globe, but rather a discontinuous band which varies according to geographic location, season, and even exhibits diurnal variation (Buckle 1996). While the classic model set out above explains ITCZ movements over the ocean relatively well (Waliser and Gautier 1993), it is less appropriate over land, where the trade winds are underdeveloped (Nicholson 2009).

In January, the ITCZ can be seen as a band of cold cloud running from equatorial

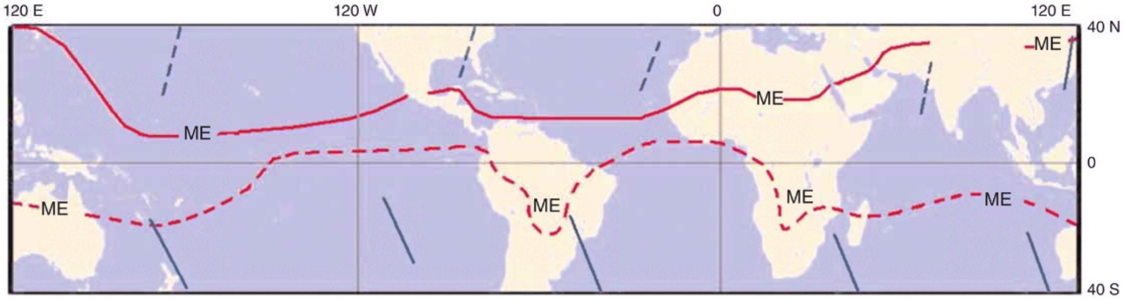

Figure 2.1: Typical seasonal variation in the location of the ITCZ in January (dashed red line) and June (solid red line). Image and citation adapted from (Galvin 2015).

Pacific Ocean through northern Australia, the southern Indian ocean and central Africa (where it crosses the equator) and the West African coast before falling back below the equator, towards South America.

In June, the ITCZ traces a more northerly position, largely located above the equator, stretching from the Gulf States, through the Sahel (a transitional zone between 10 and 15°N, separating the Sahara from the savannas to the south) and trade wind convergence region, towards Venezuela.

2.2 Observations

Observations can improve our theoretical understanding of cloud properties and provide data against which to evaluate the ability of models to represent these properties.

A variety of different observational datasets of cloud properties exist. These can be based on in-situ data, or using remote sensing instruments located either on the surface, or on satellite platforms.

This section introduces a few key cloud properties relevant to the work presented in this thesis and describes the instruments and retrieval methods used to observe them. As the work presented in this thesis aims to take advantage of the availability of the high time-resolution, global coverage and long-term datasets available from satellite remote sensing data, this section will focus on observations of cloud properties from satellite instruments.

2.2.1 Satellite instruments

The following satellite instruments are regularly used for observing cloud properties and will be referred to in the text of this thesis.

SEVIRI (Spinning Enhanced Visible and Infrared Imager) is an imager on the geostationary Meteosat Second Generation (MSG) satellite, which has been gathering data continuously since 2004. Its field of view is centred at approximately 0° longitude, giving it a view of the Atlantic and Indian oceans, the continents of Africa and Europe, as well as the Middle East and parts of South America and Asia. SEVIRI has 12 spectral channels in the visible, near-infrared and infrared. It has a temporal resolution of 15 minutes (5 minutes in rapid scan mode covering a limited area) and a spatial resolution ranging from 3 km at satellite nadir (1 km in its high-resolution visible channel) to 11 km at the edge of its field of view. Data from SEVIRI are mostly used for meteorological forecasting and for studies of the radiation budget and cloud properties.

MODIS (Moderate Resolution Imaging Spectroradiometer) is an instrument which flies on two satellites Aqua (launched in 2002) and Terra (launched in 1999). Aqua is part of the A-Train constellation of satellites, which consists of six satellites flying in formation with the aim of producing complementary datasets. Aqua gathers data at approximately 13:30 and 01:30 local solar time (LST), while Terra collects data at 10:30 and 22:30 LST. MODIS has 36 channels in the visible and infrared. MODIS' orbit repeats every 1-2 days. It has a spatial resolution of between 250 m and 1 km, depending on the channel, and a swath-width of 2330 km (King et al. 1995). Data from MODIS is used for a particularly wide variety of purposes, including observations of global cloud and aerosol properties.

CALIOP (Cloud-Aerosol Lidar with Orthogonal Polarization) is a two-wavelength polarization-sensitive lidar, measuring backscatter ($\mathrm{km}^{-1}\mathrm{sr}^{-1}$). It was launched in 2007 and is able to observe layers of cloud and aerosol in the atmosphere. Vertical profiles of total backscatter (sum of the backscatter in the parallel and perpendicular channels) in both the 532 nm and 1064 nm channels and the perpendicular backscatter at 532 nm are reported (Winker et al. 2009). Measurements of total backscatter are used to find the height of aerosol and cloud features in the atmosphere, depolarization measurements allow the differentiation of ice and water clouds, while the ratio of backscatter signals at the two wavelengths are sued to estimate variables such as aerosol particle size (Winker et al. 2006). CALIOP flies in a sun-synchronous orbit on board Cloud-Aerosol Lidar and Infrared Pathfinder Satellite Observation (CALIPSO). Like Aqua, CALIPSO flies in the A-train constellation of satellites and so gathers data at approximately 13:30 and 01:30 LST. Its orbit repeats every 16 days. CALIOP has a vertical resolution of between 30 and 60 m depending on the altitude (Winker et al. 2006).

CPR (cloud profiling radar) measures the power backscattered by clouds as a function of distance from the radar, which is then converted into radar reflectivity (dBZ). These measurements allow the vertical profiles of cloud liquid water and ice water to be observed, as well as variables including the water and ice content of clouds, the production of rain and the altitude and thickness of cloud layers (Stephens et al. 2002). CPR flies on the CloudSat satellite, as part of the A-Train of satellites and was launched in 2006. It has a vertical resolution of 500 m, a 1.4 km along-track resolution and a 1.7 km across track resolution (Posselt et al. 2008).

PR (Precipitation Radar) is the first satellite instrument to provide three dimensional observations of precipitation (Kummerow et al. 1998). It flew on Tropical Rainfall Measuring Mission (TRMM), a satellite in low earth orbit which flew between 1997 and 2015 with the aim of measuring rainfall in the tropics and extratropics. TRMM's orbit covered the area between 35°N and 35°S. This allowed TRMM to sample positions of the Earth's surface at different LSTs, in order to observe the diurnal cycle of measured properties.

TMI (TRMM Microwave Imager) also flew on board TRMM. It observed water vapour, cloud water, and precipitation over a wider swath than the PR (Kummerow et al. 1998).

2.2.2 Cloud properties

Cloud fraction (CF) is a measure of the fraction of an area covered by cloud. It is calculated by comparing the number of cloudy and clear-sky pixels over a defined region. The initial identification of cloudy, partially cloudy and clear-sky pixels is a crucial first step in retrieving cloud properties. Retrievals of further cloud properties are often only attempted for cloud-filled pixels. The accuracy of cloud detection algorithms is affected by the resolution of the instrument, the retrieval algorithms used and the structure of the cloud field itself.

Cloud optical depth (COD) is a dimensionless measure of the transparency of a cloud layer It is defined as the total extinction, at a given wavelength, in an atmospheric column due to scattering and absorption by cloud liquid droplets and ice particles. Cloud optical depth depends on the depth and microphysical properties of the cloud.

Optically thin clouds can usually be detected by active instruments such as CALIOP. However, the impact of low COD layer on passively measured radiation is very small and thus not properly detected by passive imager sensors such as SEVIRI and MODIS (Heidinger and Pavolonis 2009; Stubenrauch et al. 2010; SAFNWC/MSG 2012). This is a particular issue in the case of pixels containing semi-transparent cloud types, which have very low optical depths, as it is difficult for passive instruments to fully account for contributions from surface radiation, or low cloud layers underneath (Smith and Platt 1978).

Cloud top height (CTH) is the average height above sea level of the cloud in a region. Other frequently used measures of the vertical location of cloud are CTT and cloud top pressure (CTP).

CALIOP retrieves CTH by identification of features in vertical profiles of attenuated backscatter from the CALIOP lidar (Vaughan et al. 2009). SEVIRI employs different retrieval methods for different types of cloud. In the case of optically thick clouds, the vertical position of the cloud top can be calculated from measurements of infrared brightness temperatures in atmospheric window channels by simply correcting for above cloud atmospheric absorption (Smith and Platt 1978). However, in the case of partially cloudy pixels, or semi-transparent cloud, surface radiation may be transmitted through the cloud, or gaps in the cloud cover. In such cases a multi-spectral approach is needed (Smith and Platt 1978; Menzel et al. 1983; Schmetz et al. 1993).

For opaque clouds at all heights, CTP is often diagnosed by comparing observed 10.8 μm brightness temperatures to values simulated by a radiative transfer model. For high, semi-transparent cloud the infrared window intercept (Schmetz et al. 1993), or radiance rationing (Menzel et al. 1983) retrieval methods are attempted.

It should be noted that passive imagers such as SEVIRI observe the radiometric height of the cloud. This differs from the physical cloud top height which can be measured very accurately by active lidar instruments such as the CALIOP even for optically thick cloud (Sherwood et al. 2004).

While the physical cloud top height refers to the boundary between clear air and cloud water droplets at the top of a cloud, the radiometric height is the height from which the infrared signal detected by the imager is emitted (Sherwood et al. 2004; Stubenrauch et al. 2013). This can lie at an optical depth of 1-3 below the physical cloud top (Sherwood et al. 2004).

SEVIRI is therefore expected to underestimate CTP and CTH, and overestimate CTT relative to CALIOP. This is due to differences in the definition of the cloud properties observed by the two instruments, rather than an error in the SEVIRI retrieval.

Although it is often assumed that optically thick clouds have sharp boundaries and can be expected to radiate as black bodies (Sherwood et al. 2004; Stubenrauch et al.

2013), the radiometric height of a cloud may be several kilometres below physical cloud top height depending on its extinction profile at the cloud top and its vertical size (Stubenrauch et al. 2013). In particular, glaciated clouds tend to have poorly defined edges, even when convectively active (Sherwood et al. 2004), and so optical depths increase slowly with distance from the cloud top (Stubenrauch et al. 2013).

Sherwood et al. (2004) found that radiometric cloud tops retrieved from the Geostationary Operational Environmental Satellite 8 (GOES-8) were on average 1 km below, or 5-7 K above, the visible cloud tops observed by NASA's cloud physics lidar. This bias increased to 2 km for the highest cloud tops, and was not found to vary with cloud albedo. Other studies (Heymsfield et al. 1991; Minnis et al. 2008; Stubenrauch et al. 2010, 2013) show similar biases of between 0.5 and 3 km for high clouds in the tropics.

2.2.3 The advantages of high time-resolution observations

In-situ observations require direct sampling of the atmosphere. Instruments may be ground-based, or carried on an aircraft or balloon. Intensive field campaigns such as VAMOS Ocean-Cloud-Atmosphere-Land Study Regional Experiment (VOCALS-REx) (Wood et al. 2011) and African Monsoon Multidisciplinary Analyses (AMMA) (Redelsperger et al. 2006) often involve making in-situ measurements. While in-situ observations allow direct observation, and good spatial and temporal resolution, their spatial and temporal coverage is limited. Data gathered as part of a field campaign often focus on a small geographic area and cover a limited period of time (the most intensive periods of the VOCALS-REx and AMMA campaigns lasted just two months each).

Satellite based remote sensing data provides long term datasets and global coverage. However, there are a number of advantages and limitations to consider when using satellite data. Polar-orbiting satellites provide high spatial and temporal resolution across the entire globe, but are limited in the frequency with which they pass over individual points on the surface. Geostationary satellites cannot provide the same spatial resolution as polar orbiting satellites. Their fields of view cover approximately one quarter of the Earth's surface and due to the viewing geometries involved, they are restricted to latitudes below approximately 70°. However, their field of view does not change, allowing frequent sampling of an individual scene.

Examples of polar-orbiting instruments include vertically profiling sensors such as CPR on board CloudSat and CALIOP on CALIPSO. CPR and CALIOP are able to retrieve vertically resolved distributions of cloud and aerosol properties at a high spatial and temporal resolution, and with greater accuracy than previous generations of instruments. However, in addition to the sampling restrictions laid out above, even CALIOP and CPR are unable to resolve key microphysical cloud properties (Rosenfeld et al. 2012; Rennó et al. 2013).

Unlike CPR and CALIOP, radiometers such as MODIS (polar-orbiting) and SEVIRI (geostationary) are unable to resolve the vertical dimension. Retrieved properties therefore generally relate to the cloud top, or refer to column totals. Radiometers are also unable to retrieve both cloud and aerosol properties simultaneously. If a pixel is identified as cloud contaminated, no aerosol retrieval is made.

While low Earth orbit satellites can provide observations at high spatial resolution, their temporal sampling is limited. Polar-orbiting satellites in sun-synchronous orbit, such as those in the A-Train constellation of satellites, observe any given point (except polar regions, which are observed more often) no more than twice per day and always at the same local solar time. Other low Earth orbit satellites, such as TRMM, are able to sample a given point at varying local solar times, thereby providing statistical observations of the diurnal cycle. Individual low Earth orbit satellites are therefore unable to observe the temporal evolution of individual convective clouds.

In comparison, while the spatial resolution of geostationary satellites is limited, they provide high temporal resolution observations over a large area. The continuous nature of SEVIRI's observations makes them ideal for investigating the temporal and spatial variability of cloud across a large area and period of time.

In order to constrain cloud properties in global climate models, it is necessary to have a long term dataset of observations at sufficiently high spatial and temporal resolution at a global scale (Lohmann et al. 2007). While an analysis of data from multi-spectral sensors such as MODIS and vertical profiling sensors such as CALIPSO and CloudSat can give more accurate retrievals of cloud and aerosol properties, geostationary satellites provide better spatial and temporal coverage. In addition, analysis of data from geostationary satellites can produce insights into the development and lifecycle of convective cloud, because these processes occur on time scales of less than 24 hours (Yang and Slingo 2001; Lohmann et al. 2007).

2.2.4 Tracking convective clouds

The work presented in this thesis makes use of automated tracking of convective clouds. Cloud tracking is a useful way to investigate the lifecycle of individual convective clouds.

This section will give an overview of different approaches to tracking convective cloud and introduce the Cumulonimbus TRacking And Monitoring (Cb-TRAM) program used in this work.

History of convective cloud tracking algorithms

Automatic tracking algorithms have a detection stage, which identifies separate cloud objects at a single time step and a tracking stage, which links the objects from one time step to the next.

The majority of trackers use data from geostationary satellites' infrared channels, in which the cold tops of convective cloud anvils stand out clearly from the surface and from warmer clouds at lower levels. Usually a simple threshold is applied, with the threshold chosen to create a number of separate cloud objects in the resulting image. Thresholds typically range from 208 to 255 K. (Houze et al. 2000; Futyan and Del Genio 2007a; Pope et al. 2008; Tadesse and Anagnostou 2010; Goyens et al. 2012; Bennartz and Schroeder 2012)

A more complex approach is the 'detect and spread' method introduced by Boer and Ramanathan (1997), who use multiple thresholds to first identify areas of very cold cloud and then assign areas of warm cloud to each of the original objects through a series of warmer temperature thresholds. The end result is that the entire field of anvil cloud is divided into trackable objects, with no need for space to exist between cloud objects in order for tracking to be possible.

For the tracking stage, the most common method is to look for the area of maximum overlap between tracked objects at subsequent time steps. This can lead to the creation of too many cases in which convective clouds split or merge with each other (Arnaud et al. 1992; Williams and Houze 1987; Fiolleau and Roca 2013a).

Most cloud tracking algorithms (Schröder et al. 2009; Goyens et al. 2012; Fiolleau and Roca 2013a) are only able to predict the displacement of large-scale cloud objects. For example the tracking algorithm of Schröder et al. (2009) can only track cloud objects with an area greater than 900 km^2, while Goyens et al. (2012) are limited to objects greater than 30,000 km^2.

The Cb-TRAM program

Cb-TRAM (Mannstein et al. 2013) uses the high time-resolution observations provided by SEVIRI to track convective clouds across the SEVIRI's field of view (referred to here as the SEVIRI 'disc'). By constructing a motion vector field to forecast the movement of cloud objects over the 15 minute SEVIRI time step, Cb-TRAM is able to track exceptionally small cloud cells compared to other cloud tracking algorithms.

Full documentation of the Cb-TRAM program can be found in Zinner et al. (2008) and Merk and Zinner (2013), but an outline of the processes involved is given below.

Cb-TRAM combines observations from the high resolution visible (HRV) channel, 6.2 μm and 7.3 μm water vapour channels, and the 10.8 μm and 12.0 μm infrared channels to detect convective cloud objects at three distinct stages of their lifecycle. Stage 1 clouds are characterised by strong vertical and horizontal growth in the lower troposphere, which is measured by a combination of fast cloud top cooling in the infrared channels and increased reflectivity in the visible channels.

Stage 2 clouds are characterised by rapid development in the upper troposphere, measured by a cooling in the 6.2 μm water vapour field. For both stage 1 and 2, clouds with an HRV channel reflectivity < 0.5 are likely to be cirrus, and so are excluded.

Stage 3 clouds are mature thunderstorms. They are identified by looking for structures in difference field between the 6.2 μm and 10.8 μm channels. A positive difference between these two fields indicates that water vapour has been pushed into the stratosphere by towering convective plumes. In addition, a local standard deviation threshold is applied, using the HRV channel in the daytime and the 6.2 μm channel at night. A high local standard deviation is indicative of turbulent cloud top structures. In the case of stage 3 cloud, cirrus is excluded by applying a threshold based on the difference field between the 10.8 μm and 12.0 μm fields.

Cloud objects are created by merging any pixels identified by the methods outlined above which are closer than 2 SEVIRI pixels (a distance of approximately 8 km for most of the SEVIRI disc). A cloud must have an area of more than two connected SEVIRI pixels before it is tracked. This results in a minimum cloud object size of 18 km^2 at satellite nadir, rising to 32 km^2 for most of the SEVIRI disc. This is significantly smaller than the systems tracked by the algorithms introduced in Section 2.2.4.

In order to track such small cloud objects over periods of time as large as 15 minutes, Cb-TRAM derives a high-resolution motion vector field, which allows both the displacement of identified cloud objects, and also changes in cloud area, or shape to be predicted from one time step to the next.

The method of constructing this field is illustrated in figure 2.2. The process begins with two images showing bright structures of two squares on a random background (figure 2.2a.i and ii). These images could, for example, represent brightness temperature fields for two SEVIRI pixels at two successive time steps. These two images are compared in order to produce a disparity vector field, defined at each pixel position. The first image is moved ±2 pixels in each direction. The squared difference between the intensities are compared in each case, in order to find the best fit between the warped version of image 2.2a.i and the original image 2.2a.ii.

In order track such small clouds over a relatively long period of time (15 minutes),

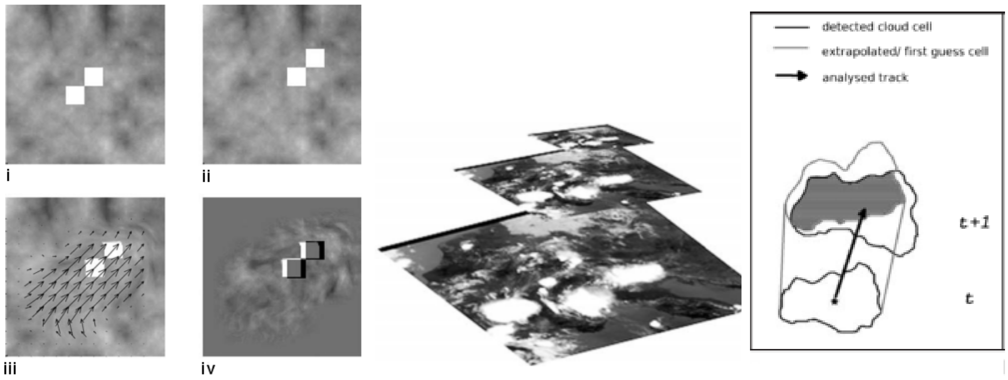

(a) (b) (c)

Figure 2.2: Illustration of the Cb-TRAM algorithm. Panel a: the initial step uses two consecutive images (i, ii) to determine a motion vector field (plotted in iii) which best describes how to warp (i) onto (ii) while minimising the remaining difference field (iv). Panel b: this vector field is constructed successively at three resolutions, (moving from low to high). Panel c: a cell object detected at time t is recovered at time t+1, using the motion vector field to determine overlap between objects at successive time steps. Figures and caption adapted from Zinner et al. (2008).

this process is repeated three times, at increasing resolutions (figure 2.2b), until the difference between the warped version of image 2.2a.i and the original version of image 2.2a.ii is minimal (figure 2.2b.iv). The final result is a vector field (figure 2.2a.iii) which describes the warping of one of the images onto the other.

By repeating the process at three successive levels of resolution, a shift of up to 32 SEVIRI pixels during a single time step can be detected. The process is carried out at high resolution first, as the motion of small scale features is often dominated by large-scale flows. As mentioned above, this motion field not only allows the prediction of displacement at a higher resolution than an algorithm based on average wind vectors, it also accounts for changes in shape and area.

Finally, the motion vector field is used to forecast the future position of cloud objects detected at time step t, and match them to cloud objects detected at time t=1. Objects are matched by looking for the maximum overlap between an object detected at time t=1 and the forecast position of an object detected at time t (figure 2.2c).

In cases where a detected object at time t overlaps with more the extrapolated location of more than one object from time t-1 the tracking is continued for the largest object only. The other cell patterns are considered to have merged with the largest object and are not tracked further. This results in a higher number of shorter-lived cores than would be the case if all instances of convective cloud merging were removed from this study. It should be noted therefore that short cloud lifetimes do not always correspond to the dissipation of convection, but also to cases where cloud cores merge.

In cases when the extrapolated location of an object at time t overlaps with the location of more than one object detected at time t+1 the object with the largest overlap area inherits the tracking history. The original core is considered to have split, and any other cell patterns are initialised as new convective cores. This also results in a higher number of shorter-lived cores than would be the case if all instances of convective core splits were removed from the dataset. It should be noted that when considering the spatial distribution and diurnal cycle of the initiation of convection, cases of initiation due to splitting of convective cloud cores will be included in these figures.

2.3 Observations of convective cloud

2.3.1 Diurnal cycle

The diurnal cycle of tropical convection, driven by variations in solar forcing, is among the strongest and most fundamental modes of variation in the global weather and climate systems (Hendon and Woodberry 1993; Yang and Slingo 2001; Levizzani et al. 2010; Venugopal et al. 2016). A large number of observational studies using data from rain gauges (Wallace 1975; Gray and Jacobsen 1977), surface weather reports (Dai 2001) and both polar-orbiting (Nesbitt and Zipser 2003; Yang et al. 2008; Stratton and Stirling 2012) and geostationary (Meisner and Arkin 1987; Janowiak et al. 1994; Chen and Houze 1997; Yang and Slingo 2001; Schröder et al. 2009) satellites have attempted to quantify the diurnal cycle of convection over land. These studies found an early afternoon maximum in convective precipitation, followed by a minimum in cloud top temperature approximately three hours later. The two features are thought to correspond to the beginning and end of the mature stage of convection (Schröder et al. 2009).

However, these large-scale features, driven by insolation, display regional and seasonal variations (Yang and Slingo 2001; Schröder et al. 2009) and can be overridden by other factors such as orography (Yang and Slingo 2001; Nesbitt and Zipser 2003; Vondou et al. 2010), land-sea breezes (Chen and Houze 1997; Yang and Slingo 2001; Halladay et al. 2012) and the organisation of convection (Nesbitt and Zipser 2003).

The diurnal cycle of the intensity of convection follows a similar pattern, with a sharp peak at 17:00 UTC over land and a broad peak at 07:00 over the ocean (Zipser et al. 2006). While the timing of the peak over land is similar to that measured by precipitation the peak in convective intensity is sharper.

The amplitude of the diurnal cycle of convection is smaller over the ocean than over land (Harrison et al. 1988), due to the ocean's higher heat capacity, and because ocean mixing distributes incoming solar radiation away from the surface. Most studies show a substantial pre-dawn peak in convective cloud over the oceans (Janowiak et al. 1994; Yang and Slingo 2001; Nesbitt and Zipser 2003; Bain et al. 2010; Stengel et al. 2014). The mechanisms responsible for this overnight peak in convective cloud remain uncertain (Bain et al. 2010), but are thought to be related to atmospheric instability caused by night time radiative cooling (Randall et al. 1991) and to the presence of a larger number of MCS during the night (Chen and Houze 1997; Nesbitt and Zipser 2003).

However, general circulation and numerical weather prediction models which parameterise convective processes fail to capture the observed diurnal cycle of convective cloud (Yang and Slingo 2001; Guichard et al. 2004; Grabowski et al. 2006; Stratton and Stirling 2012). This is generally the result of convection initiating shortly after sunrise, which develops to rapidly, quickly reaching the tropopause and producing precipitation (Guichard et al. 2004; Stratton and Stirling 2012).

Studies by Guichard et al. (2004); Grabowski et al. (2006) and Sato et al. (2009) show that in some cases, CRMs, which explicitly resolve convection, are capable of correctly predicting the amplitude and phase of the diurnal cycle in convection. Over land, this accuracy is strongly dependent on horizontal resolution, requiring grid lengths of around 1 km (Guichard et al. 2004), or 500 m (Grabowski et al. 2006) in order to represent key convective processes, such as radiative effects and transport of heat, moisture and momentum, over land. Over the ocean, horizontal resolution appears to be less important, which is likely due to differences in predominant cloud types and lifecycles (Sato et al. 2009).

2.3.2 Lifecycle

This section will review the literature on lifecycles of deep convective cloud and will highlight some of the open questions which will be addressed in Sections 3 and 4 of this thesis. As discussed in Section 2.1.3, the broad features of convective cloud lifecycles have been observed and are generally consistent with current understanding of the physics of convection. However, the variability of convective lifecycles, including such properties as time of convective initiation, cloud lifetime, speed of development and organisation are not well characterised on the global scale. Studies of convective cloud lifecycles provide insights into these processes and also allow us to consider various mechanisms by which these properties can be altered. In addition, quantifying the characteristics of convective clouds across their lifecycle provides valuable information about avenues for future development and validation of both convective cloud process models and convective parameterisations.

However, only in recent decades has it become possible to observe the complete lifecycle of individual convective clouds in a Lagrangian framework, over a large area and period of time. Spatial scales of convection range from thousands of kilometres for MCS to less than a kilometre for individual convective plumes, while time scales of convective variability range from minutes through to seasons. A Lagrangian approach to the study of convective cloud lifecycles therefore requires high spatial and time-resolution data from geostationary satellites, as well as the development of cloud tracking tools and sufficient computing resources to apply these tools to a large amount of data.

Aspects of the lifecycle of convective cloud can be studied in an Eulerian framework, using static datasets such as those available from low Earth orbit satellites. Due to the higher spatial resolution of low Earth orbit satellites and the computational expense of running cloud tracking software, the majority of published studies on convective cloud lifecycles are based on static datasets. These datasets are only able to sample an individual cloud once during its lifecycle. However, by making a large number of observations, some insights into the lifecycle of convection can be gained. Other studies have attempted to observe dynamic convective cloud lifecycles by tracking individual convective clouds. These studies are often limited to a small area and period of time. In some cases they comprise a case study of a single cloud.

Many studies of convective cloud lifecycles discuss the intensity of convection. However, there is no generally accepted measure of convective intensity. Intensity can be approximated by many measures, including cloud top temperature, lifetime, precipitation (Zipser et al. 2006), updraft speed (Chong et al. 1987; Chalon et al. 1988), rate of horizontal expansion (Futyan and Del Genio 2007a), number of overshooting cloud tops (Liu and Zipser 2005), or frequency of lightning (Orville 1981; Zipser et al. 2006; Futyan and Del Genio 2007a; Tadesse and Anagnostou 2010).

The most intense convection (as measured by CTT, overshooting cloud tops, lightning and rate of horizontal expansion) is found over land (Liu and Zipser 2005; Zipser et al. 2006; Futyan and Del Genio 2007a; Tadesse and Anagnostou 2010). By creating composites of convective storms over different surface types, Futyan and Del Genio (2007a) show that convective storms over land are generally colder, deeper, have more lightning and are more intense (where intensity is measured by the speed of expansion and cloud height) than those over ocean. Storms over the ocean are found to be larger, with a bigger precipitating area. These differences between land and ocean convection are thought to be due to the stronger diurnal cycle of convection over land, with conditions becoming much more favourable for convection during the daytime due to solar forcing (Futyan and Del Genio 2007a; Houze 2004).

Bouniol et al. (2016) track MCS in West Africa, the adjacent Atlantic Ocean and the open Indian Ocean. They find that continental convection is more intense, as measured by variability in CloudSat reflectivities and the amount of ice lifted to high altitudes in the cloud, than oceanic convection. Larger and denser hydrometeors are found at the start of the convective lifecycle over land, with intensity dropping off later into the cloud's life. The intensity of convection over ocean is lower, but also more uniform over the cloud's lifetime, again, likely due to the stronger diurnal cycle over land.

Amazon and Indonesia have the highest concentration of moderately intense convective events, while equatorial Africa has the most extreme convection (Zipser et al. 2006). The highest counts and density of lightning are found in Africa, which sees twice as many, and twice as dense, lightning flashes as the Amazon region. The maritime continent receives little lightning (McCollum et al. 2000; Williams and Stanfill 2002). Using data from the Special Sensor Microwave Imager, Zipser et al. (2006) shows that extreme convective events are also found at higher latitudes, including Canada and Russia. Although these storms are neither as frequent, nor as intense as those in the tropics.

Using data from CALIOP and the CloudSat CPR, Peng et al. (2014) show that the greatest concentration of deep convection (defined regions of cloud which are strongly developed in the vertical direction) in central and southern Africa, northern South America and Tibet (Peng et al. 2014). Overshooting cloud tops are also concentrated disproportionately in central Africa, with large numbers also observed in Indonesia and South America (Liu and Zipser 2005).

The area expansion rate during the developing stages of convection is another metric used to provide an estimate of the intensity of convection. Tadesse and Anagnostou (2010) show that a rapid rate of area expansion of a convective system is correlated with a longer lifetime and a larger horizontal size.

Thunderstorms expand faster, and are on average have double the horizontal cloud area as rainstorms (defined as deep convective systems without lightning) (Tadesse and Anagnostou 2010). Using lightning data from the long-range lightning detection network ZEUS and geostationary infrared data to track convective cloud systems across much of the African continent, Tadesse and Anagnostou (2010) show that 93% of tracked thunderstorms and 97% of rainstorms live for less than 8 hours. For the thunderstorms, the lightning is concentrated in the growth stage of the cloud's lifecycle, with lightning strikes rapidly decreasing towards zero in the dissipation stage.

Continental African storms move from convectively active systems with lightning in their growth stage, to more stratiform conditions in the dissipation stage. However, the convectively active fraction of storms over the Atlantic ocean remains relatively constant throughout all development stages, while the occurrence of lightning peaks later on in the lifecycle (Futyan and Del Genio 2007a). This indicates that there are important differences between the lifecycles of convection over land and ocean, likely driven by differences in the sustainability of convection over different surfaces (Futyan and Del Genio 2007a).

While most convection tracking studies focus on the movement of entire convective systems, a few differentiate between the convective core and anvil. Bedka et al. (2010) characterized the locations, diurnal cycle and cloud top properties of deep convective cores and anvils during the 2007 Tropical Composition, Cloud and Climate (TC4) field campaign in Costa Rica. They show that deep convection occurred within the anvil area for approximately 60% of the storms' lifetime, with the updraft area accounting for approximately 24% of the storm's area. Maximum core CTH occurred 20% into cloud lifetime, with COD peaking 20% into lifetime for core and 20-50% of lifetime for the anvil.

Many studies have used CloudSat CPR to study the relationship between the extent of MCS anvils and cores.

Yang et al. (2013) proposes 'anvil productivity' as a measure of the ratio of the horizontal area of the raining cloud core to that of the anvil and shows that this ratio decreases as the overall scale of the convective system increases. Anvil productivity is shown to depend on convection scale, its point in its lifecycle, the intensity of convection and the large-scale environment (Deng et al. 2016). The anvil section of MCS is generally limited to between 1.5 and 2 times the radius of the core, although this increases to 5 times the radius over the western tropical Pacific warm pool (Yuan and Houze 2010).

Igel et al. (2014) use CloudSat data to develop a dataset of cloud objects which are divided into anvil and core regions. They investigate the dependence of anvil morphology on sea surface temperature and find that anvil thickness increases, anvil width decreases and cloud top temperature cools at higher sea surface temperature. Convection is further observed to be invigorated in the presence of higher levels of convective available potential energy, aerosol optical depth and upward mid-level vertical velocities (Igel and van den Heever 2015). High wind shears are correlated with wider, but shallower clouds (Igel and van den Heever 2015).

2.3.3 Convection over Africa and the Atlantic

Much of the work presented in this thesis will focus on high time-resolution observations of tropical convective clouds over the continent of Africa and the Atlantic Ocean. As discussed above, tropical Africa is a hot spot for convective activity, producing the most numerous and intense convective storms on Earth. Some of these storms propagate out into the Atlantic ocean, although convective clouds can also generate over the ocean surface.

In order to give a larger-scale context for convection in tropical Africa and the Atlantic ocean, a brief overview of the geography, climate and meteorology of the region is presented here.

The African continent is located primarily in the tropics, with two-thirds of its landmass between 30°N and 30°S. Within the tropical and subtropical latitudes of Africa the diurnal variation in temperature (10-15K outside of desert regions) is greater than the annual variation (less than 10K south of the Sahara) (Nicholson 2001). Annual mean temperatures are generally high with the cooler conditions associated with mid-latitude depressions only observed in the far north and south. However, these high temperatures are moderated in the highland plateaus of eastern, central and southern Africa (Leroux 1983).

Topographic height across Africa and the Arabian Peninsula is illustrated in figure 2.3, using data from the Shuttle Radar Topography Mission in 2000 (NASA 2004). central Africa is dominated by the Great Rift Valley, which runs from the Red Sea in the north to Lake Malawi in the south and splits into two sections around lake Victoria, where it encloses the East African plateau. The Congo basin, a shallow feature surrounded by highlands, lies to the west. Southern Africa is covered by a

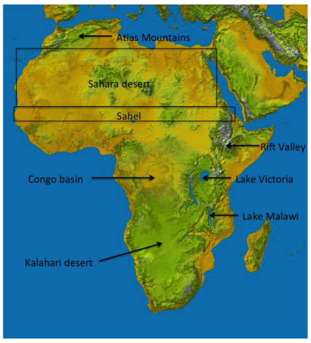

Figure 2.3: Digital elevation map of Africa and the Arabian Peninsula. Colour-coding is directly related to topographic height, with brown and yellow at the lower elevations, rising through green, to white at the highest elevations. Blue areas on the map represent water. Elevation data used in this image were acquired by the Shuttle Radar Topography Mission aboard the Space Shuttle Endeavour during February 2000. Figure and caption adapted from NASA (2004). ©NASA/JPL/NIMA 2004.

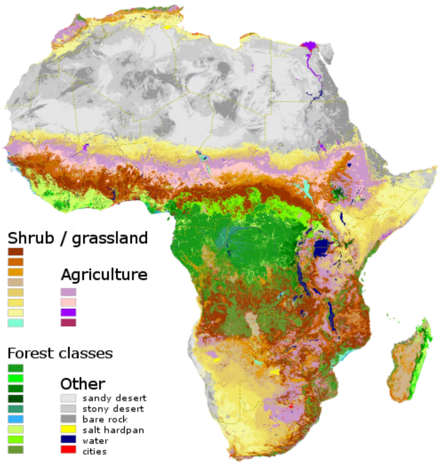

Figure 2.4: Land cover classification produced from data acquired in 2000 from the SPOT VEGETATION instrument. Yellow-brown colours are shrub or grassland, green colours are forested areas, pink-purple colours are agricultural, grey areas are desert or rock, bright yellow are salt hardpans and red areas are cities. Dark blue areas represent water. A detailed description of the different categories is available from Mayaux et al. (2003). Image and caption adapted from Mayaux et al. (2003). ©European Commission 2003.

large plateau, with the semi-desert of the Kalahari surrounded by a mountainous fringe and a thin coastal plain (NASA 2004). Convection, and MCS in particular, are often triggered in the lee of such high terrain. The northern part of the continent consists of a mixture of plateaus and the sand-filled basins which form the Sahara. In the northeast, the Atlas Mountains separate the Sahara from the more Mediterranean climates of the Maghreb (NASA 2004).

Figure 2.4 shows land cover types across Africa. A full description of the nuanced categories displayed is not presented here, but is available from Mayaux et al. (2003). Broadly, yellow-brown colours are savanna, shrub or grassland, green colours are forested areas, pink-purple colours are agricultural, and grey areas are desert (a major source of dust aerosol) or rock (Mayaux et al. 2003).

Africa's symmetrical location with respect to the equator, combined with an absence of large, high mountain ranges to inhibit air flow results in a remarkable lack of climactic divides across the continent. Its meteorology and climate are therefore more heavily influenced by major planetary circulations than other tropical continents, with symmetric patterns apparent in the northern and southern hemispheres (Buckle 1996).

In the absence of clear climactic divides, African climate regimes are largely differ-

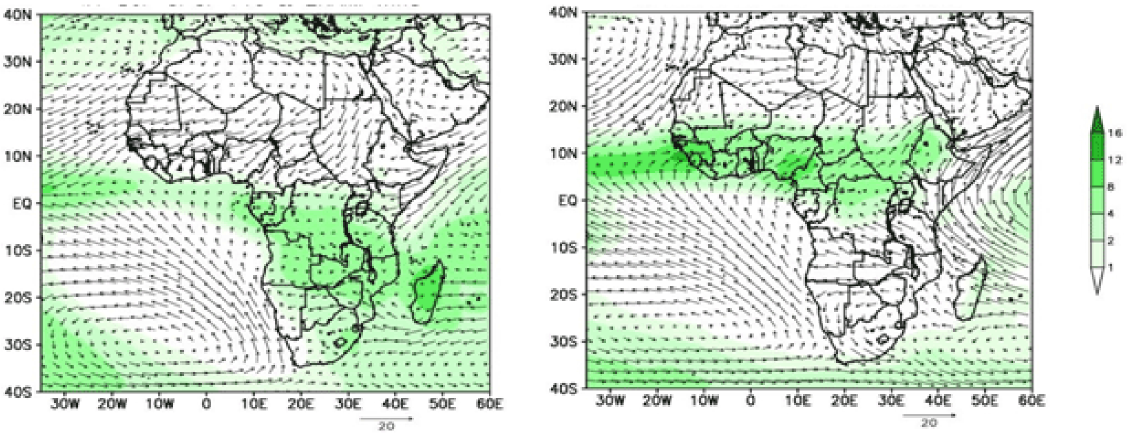

Figure 2.5: Average observed 1989-2005 precipitation (in mm/day) from GPCP, with 925 hPa wind vectors from ERA Interim Reanalysis superimposed. Left: DJF, right: JJA. Image and caption adapted from (Sylla et al. 2009).

entiated by the amount of precipitation they receive (Buckle 1996). The seasonal movement of the ITCZ is the classic explanation for the presence of one or two rainy seasons per year over much of the African continent. Figure 2.5 shows mean observed annual precipitation, from data gathered by the Global Precipitation Climatology Project (GPCP) for the months of December, January and February (DJF) and June, July and August (JJA). Comparing the two images it is obvious that some areas, such as the Saharan and Kalahari deserts, receive little to no rain while others, such as the Congo basin and the west coast of Madagascar, are wet all year round. Some regions are seasonally dry, receiving rain during one or two rainy seasons each year (Nicholson 2001).

The other key large-scale circulation in this region are the tropical jets. The tropical easterly jet is a region of intense winds lying in the upper troposphere and extending from Asia to West Africa (Galvin 2015). Although the intensity of this jet has been linked to changes in precipitation in West Africa (Kanamitsu and Krishnamurti 1977; Grist and Nicholson 2001), it is generally viewed as less important to African weather and climate than the weaker African easterly jet (AEJ).

The AEJ is an area of strong easterly winds in the tropical mid-troposphere (Galvin 2015). It forms in the northern hemisphere summer, due to the temperature contrast between the Sahara and the cooler conditions in the Gulf of Guinea (Cook 1999). Disturbances in the AEJ are thought to generate African easterly waves (AEWs) (Burpee 1972, 1974), although the mechanisms involved remain uncertain (Hsieh and Cook 2005; Nicholson et al. 2007). These waves are located in the mid-troposphere and found close to the equator in West and central Africa during the summer months. They have a short wavelength and a period of 3-5 days. AEWs propagate towards the west, producing divergence aloft and convergence at the surface which can cause MCS to form at or ahead of AEW troughs over both land (Reed et al. 1977; Duvel 1990; Fink 2003) and ocean (Burpee 1974). These waves are important for the formation of convective storms both over land and over the

Atlantic ocean, accounting for much of the annual precipitation received in the Sahel (Gaye et al. 2005), central and West Africa (Galvin 2015).

With the exception of the southern and northern extremities of the continent, weather patterns over Africa are governed by two types of air mass: tropical continental and tropical marine. Tropical continental air masses originate from high pressure systems over the Saharan, Arabian and Kalahari deserts and transport hot, dry and stable air, bringing little cloud or rain. Such air masses bring suppressed convection, and high concentrations of dust aerosol. From December to March, tropical continental air is transported by the 'Harmattan' wind which flows into the Sahara and can reach south to the coast of West Africa and parts of East Africa (Buckle 1996).

Tropical maritime air, originating from the subtropical highs of the Atlantic and southern Indian Ocean, brings warm, moist air to the continent. However, atmospheric stability differs between the east and west coasts. To the west, this air mass is trapped in a thin layer by the trade wind inversion, while cold sea surface temperatures, caused by the upwelling Benguela and Canary currents, serve to reinforce the stable atmospheric profile (Buckle 1996). Tropical maritime air therefore brings little cloud or precipitation along the west coast. On the east coast, the major subtropical high is known as the Mascerene. From May to October, the Mascerene is situated at approximately 30°S and 70°E, and the resulting trade wind inversion reduces instability, suppressing precipitation. However, from November to April, the Mascerene weakens, and retreats to the East, allowing the inversion to lift and bringing a deep layer of warm, moist air to the east coast, particularly Madagascar (see figure 2.5). Rainfall is enhanced by the warm Agulhas Current running along the west coast. Tropical maritime air masses acquire increasing amounts of moisture as they move towards the equator and the ITCZ, where surface heating and orographic forcing can easily initiate convection (Buckle 1996). These air masses bring the majority of tropical Africa's rainfall. (Buckle 1996).

3 | Evaluating Convective Variability

3.1 Introduction

In order to study the lifecycle of convection, it is first necessary to know something about the spatial and temporal variability of convective clouds. As discussed in Section 2.3.1, many previous studies have attempted to quantify aspects of this variability. However, the high time-resolution and continuous nature of recently developed datasets from SEVIRI provide a new opportunity to investigate convective variability across large areas and periods of time.

This section uses SEVIRI CTT data to quantify the spatial, seasonal and diurnal variability of convective cloud. This study aims to consider the impact of retrieval biases on SEVIRI's ability to accurately capture the details of this variability. It will also identify regions of strong convective activity.

The new SEVIRI datasets are introduced in Section 3.2. Based on this data, spatial and seasonal patterns in CTT are examined in Section 3.3.1. In Section 3.3.2 the SEVIRI cloud top temperature data is compared to CALIOP measurements, extending on existing validation analyses in order to consider the implications of spatial and diurnal variations in retrieval bias for the SEVIRI-based diurnal cycles of CTT. In Section 3, the diurnal variability of cloud top temperature is quantified across the SEVIRI disc. Conclusions are presented in Section 3.4.

3.2 Data

The analysis presented in this section uses cloud top property data from SEVIRI. These data were obtained from the EUMETSAT Satellite Application Facility on Climate Monitoring (CMSAF)'s recently updated twelve year dataset of cloud top properties based on SEVIRI measurements, named the CLoud property dAtAset using SEVIRI, version 2 (CLAAS-2) (Benas et al. 2016). CLAAS-2 contains the only retrieval of cloud top properties currently available at full SEVIRI spatial and temporal resolution and over a period of several years. The specific dataset used in this study is the instantaneous cloud top parameters product (CTX version 002) (Benas et al. 2016). The dataset is available for the period 2004-2015 and retrieved at full SEVIRI spatial and temporal resolution.

The retrieval algorithm applied to produce the CLAAS-2 dataset was developed in the framework of the European Organisation for the Exploitation of Meteorological Satellites (EUMETSAT) Satellite Application Facility on Nowcasting (NWCSAF). The full algorithm (NWCSAF/MSGv2012) is documented in Derrien (2013). To summarize, a multi-spectral threshold method, applying a variety of threshold tests in different channels, is used to obtain a pixel-resolution cloud mask. These tests vary according to conditions such as solar illumination, satellite angle and surface type. Cloud type and cloud top properties are also retrieved for pixels classed as fully cloudy. No further retrievals are made for clear sky pixels, or pixels classified as containing broken clouds.

The NWCSAF/MSG retrieval calculates the vertical placement of clouds for fully cloudy pixels via a CTP retrieval, which varies according to cloud type, atmospheric conditions, and the data available.

In the case of optically thick clouds, the vertical position of the cloud top is calculated from brightness temperatures by accounting for above cloud atmospheric absorption. A multi-spectral approach is used for partially cloudy pixels, or semi-transparent cloud.

For opaque clouds at all heights, CTP is diagnosed by comparing observed 10.8 μm brightness temperatures to values simulated by the Radiative Transfer Model for TOVS (RTTOV) radiative transfer model. For high, semi-transparent cloud the infrared window intercept, or radiance rationing retrieval methods are attempted. Full details of the retrieval algorithm in the case of other cloud classification types can be found in Derrien (2013).

Finally, for all cloud types, CTT and height are calculated from cloud top pressure using input from ERA Interim Reanalysis fields.

This study also used CLAAS-2 monthly mean diurnal cycle CTT products to quantify the diurnal cycle of CTT across the SEVIRI disc. These data are provided at a spatial resolution of 0.25° and a temporal resolution of one hour.

All SEVIRI data used in this study are drawn from the CLAAS-2 CTT dataset, retrieved from SEVIRI observations using the NWCSAF/MSGv2012 algorithm (Benas et al. 2016). For clarity, the term 'SEVIRI' will be used to refer to these datasets in this section.

Finally, instantaneous SEVIRI data are validated against CALIOP, in order to investigate the implications of both the spatial and diurnal variability in SEVIRI's retrieval bias for the accurate quantification of diurnal cycles in CTT. The CALIOP dataset used in this study is the same product used in the CLAAS-2 validation report (Benas et al. 2016), the Lidar, Level 2, 5 km Cloud Layer, Validated Stage 1 Version 3 product (CAL LID L2 05kmCLay-ValStage1-V3-01) (NASA 2013).

3.3 Results

3.3.1 Mean cloud top temperature

Seasonal mean SEVIRI cloud top temperatures for the period 2005-2015 are shown in Fig. 3.1. As expected, the warmest CTTs are observed over the ocean and the coldest over land, where a strong diurnal cycle in land surface temperatures drives convective initiation. Typical cloud regime patterns, showing deep convection over land in the region of the ITCZ, shallower convection over the central Atlantic ocean in the trade wind convergence zone and stratocumulus cloud in the southeast Atlantic ocean are evident.

Seasonal patterns in convection, driven by the movement of the ITCZ (Waliser and Gautier 1993; Yang and Slingo 2001; Schröder et al. 2009) can be clearly seen. In DJF, the ITCZ is shown as a band of cold cloud running from the southern Indian ocean, through central Africa (where it crosses the equator) and the West African coast before falling back below the equator, towards South America. In JJA, the ITCZ traces a more northerly position, largely located above the equator, stretching from the through the Sahel and trade wind convergence region, towards Venezuela.

In all seasons, regions with the coldest clouds have seasonal mean CTTs 0 K and 240 K, indicative of persistent deep convection in these areas. These clouds are concentrated in central Africa, the Amazon and the West African coast. The warmest CTTs are found in the region of persistent stratocumulus cloud in the southeast Atlantic Ocean, where seasonal mean CTTs range between 270 K and 290 K.

The position of the central Atlantic trade wind convergence zone is closely related to the seasonal movement of the ITCZ. Cloud top temperatures in this region fall to between 230 K and 250 K, with particularly cold clouds observed in March, April and May (MAM) and September, October and November (SON) due to the passage

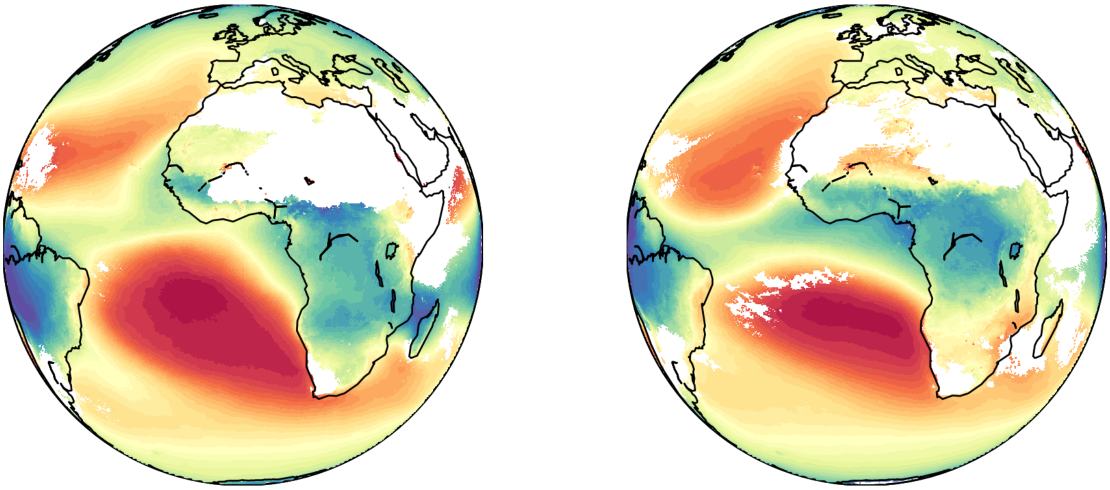

(a) DJF

(b) MAM

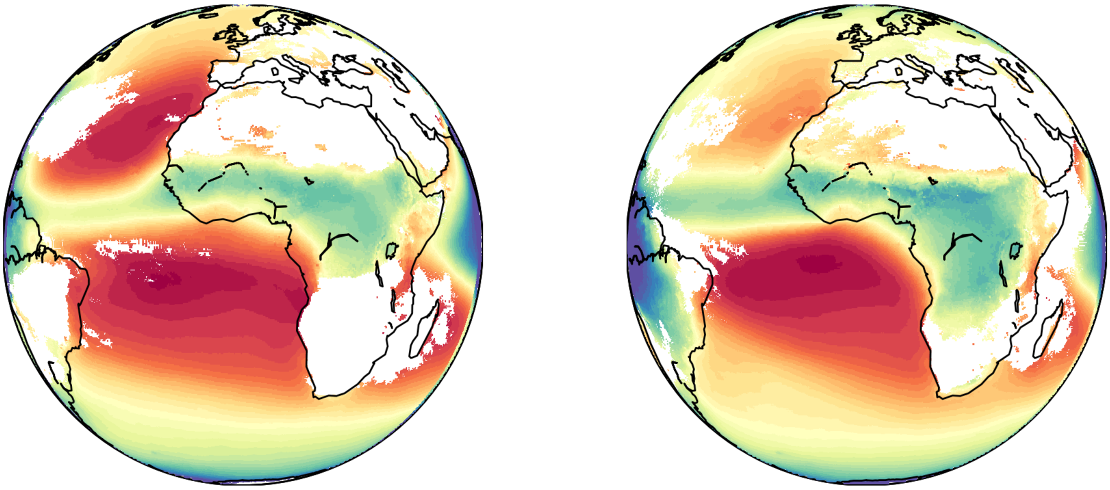

(c) JJA

(d) SON

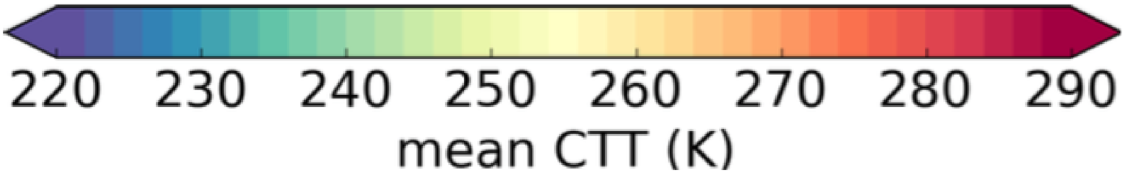

Figure 3.1: Seasonal mean SEVIRI cloud top temperatures for the period 2005-2015. Values are shown for all regions where cloud is observed for at least 10% of possible retrievals.

of the ITCZ. This indicates the presence of shallower convective cloud, initiated by the convergence of northern and southern hemisphere winds.

The concentration of cold clouds in Central and West Africa suggests that the absolute diurnal cycle of convection (the mean change in CTT throughout the day) is likely to be strongest in these regions, due to the strong vertical development of deep convective clouds. However, before attempting to quantify the diurnal cycle of CTT using SEVIRI data, it is necessary to consider the impact of spatial and diurnal variations in retrieval biases, which may have a significant impact on the diurnal cycle derived from this dataset.

3.3.2 Evaluation of SEVIRI cloud top temperature retrievals with CALIOP data

Biases in the CTT retrieval can be expected to display significant temporal and spatial variation. For example, Fig. 3.1 shows clear spatial and seasonal patterns in cloud type, while surface emissions of longwave radiation also display spatial and temporal variations, particularly over land (Harrison et al. 1990; Wild et al. 2014). The implications of cloud type and land surface emissivity for the accuracy of cloud top property retrievals from SEVIRI were discussed in Section 2.2.2.

In the validation report for the CLAAS-2 dataset, Benas et al. (2016) compare the CLAAS-2 CTT data to measurements from the CALIOP instrument between 2006 and 2015. The comparison is made for the CALIOP cloud layer at which the vertically integrated COD is at least 0.2. For this setting they find a mean bias of 2.1 K and a bias-corrected root mean squared error (RMSE) of 16.3 K. Bias and RMSE amount to 11.4 K and 22.1 K when no COD thresholds are applied.

This study considers the implications of both the spatial and diurnal variability in retrieval bias for the accuracy of diurnal cycle measurements across the SEVIRI disc. To this end one year of SEVIRI and CALIOP CTT retrievals were compared across the SEVIRI disc. This analysis was carried out using data from 2007, the first full year for which CALIOP data are available. Data was processed for a single year of the twelve year CLAAS-2 dataset, balancing the need to process sufficient data points to be able to examine the spatial variability of retrieval bias with the considerable computational expense of collocating two large datasets.

Collocation

Although CALIOP provides a limited number of observations compared to SEVIRI, it provides a very accurate measurement of CTH, and hence CTT, due to its active measurements. It is therefore an excellent dataset for assessing the accuracy of SEVIRI cloud top retrievals. CALIOP also offers the advantage of a long-running dataset (2006 - present) and global coverage, allowing data to be compared across the entire SEVIRI disc over a long period of time.

CALIOP measures CTH and subsequently uses the Goddard Earth Observing System Model, Version 5 (GEOS-5) atmospheric global climate model to convert from CTH to CTT (NASA 2013). This conversion can be seen as a potential source of uncertainty in the CALIOP CTT representation, since the model has a coarser vertical and horizontal resolution than CALIOP, with values reported at six hourly intervals.

Abbreviation	**Symbol**	**Collocation window (mins)**	**Layers included**	**COD threshold**
60-ML-0	□	60	multi	none
15-ML-0	×	15	multi	none
60-SL-0	◊	60	single	none
60-ML-03	+	60	multi	> 0.3
60-ML-1	∇	60	multi	> 1.0
60-ML-2	△	60	multi	> 2.0
60-SL-1	●	60	single	> 1.0

Table 3.1: Descriptions of the seven sets of collocation criteria to be evaluated, the abbreviations by which they are referenced in the text and the symbols by which they are referenced in figures.

Additionally, rising air parcels (such as those found in convective clouds) are usually warmer than the surrounding air, as represented by the grid mean temperature of the model fields.

As CALIOP is capable of detecting cloud layers with optical depths as low as 0.01, while SEVIRI's detection efficiency decreases at low optical depths, it is necessary to exclude very thin cloud layers from this comparison. Previous comparisons of SEVIRI and CALIOP data have excluded all cloud with an optical depth of less than 0.3 (Kniffka et al. 2013), 0.2, (Benas et al. 2016) and 0.1 (Stubenrauch et al. 2010; SAFNWC/MSG 2012), while others have not excluded thin cloud at all (Reuter et al. 2009). In this analysis, mean statistics were calculated for a number of different collocation criteria. Due to the computational expense of collocating the datasets, different collocation criteria were tested using data for every 10th day in 2007.

Table 3.1 contains information on the seven different sets of collocation criteria tested. It indicates the maximum time window during which retrievals could be collocated, whether multi-layer clouds were included in the comparison and what COD threshold was used. Each set of criteria is identified by an abbreviation, used to refer to individual scenarios in the text and by a symbol, used to refer to scenarios in the figures.

The mean bias and RMSE for each of the collocation criteria in Table 3.1 are shown in Fig. 3.2. Statistics are plotted separately for all collocated data points and also for land retrievals only and ocean retrievals only. The number of SEVIRI CTT retrievals collocated with CALIOP for each of the sets of criteria and the number of land and ocean retrievals are shown in Fig. 3.3.

Adjusting the maximum time window for collocation from 60 to 15 minutes (60-ML-0 and 15-ML-0) does not have a large effect on the mean bias and RMSE (Fig. 3.2). However, Fig. 3.3 shows that a 15 minute collocation window reduces the number of collocated retrievals by 50%. The insensitivity of the bias to changes in

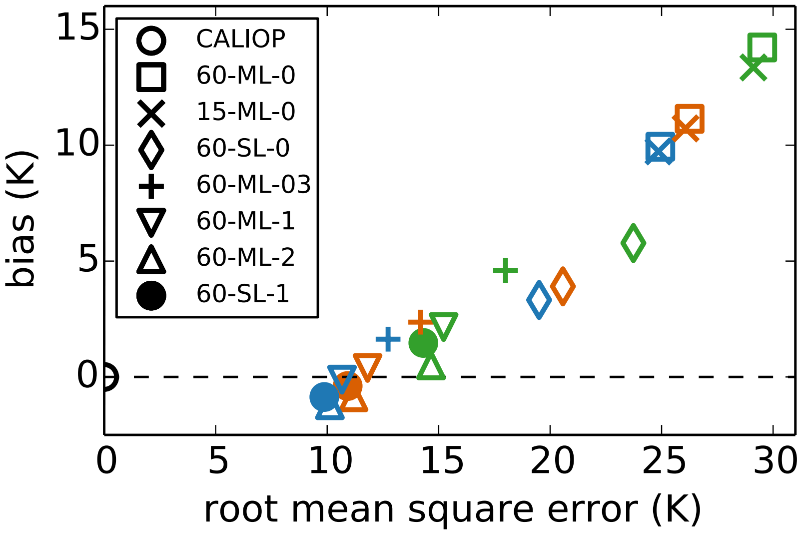

Figure 3.2: Bias (SEVIRI minus CALIOP CTT) versus root mean square error of SEVIRI cloud top temperature retrievals. Symbols refer to the different sets of collocation criteria, defined in Table 3.1. Green symbols show retrievals over land, blue over ocean and orange over both. The 'CALIOP' point on the left-hand side indicates where a retrieval which perfectly reproduced the CALIOP observations would be located.

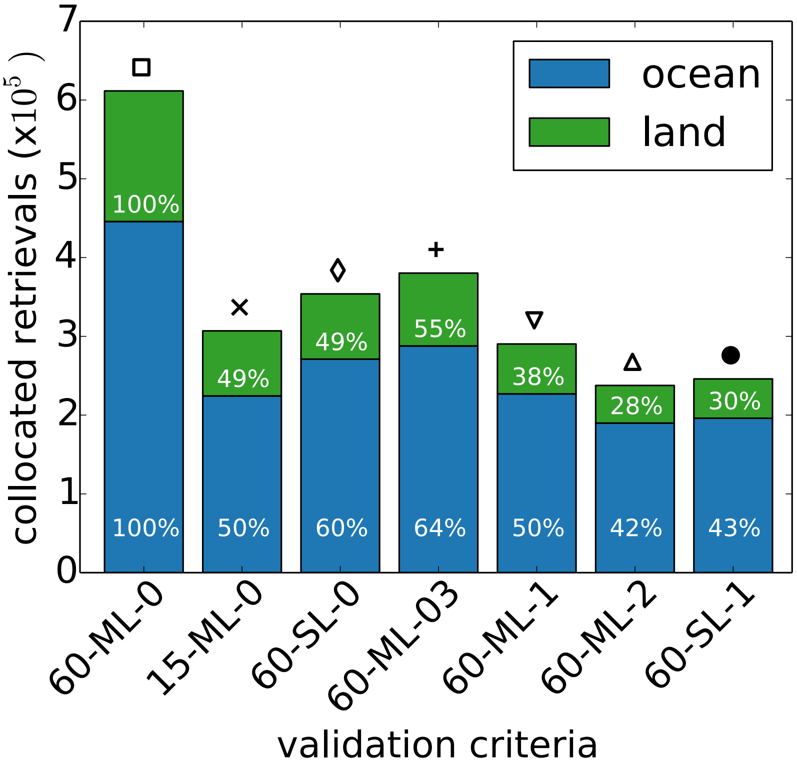

Figure 3.3: Number of SEVIRI and CALIOP retrievals collocated in 2007 for each of the collocation criteria defined in Table 3.1. Collocation criteria are identified by both text abbreviation and symbol. Colours show the division between land (green) and ocean (blue) retrievals. Percentages show what fraction of the total number of available retrievals are processed for each set of collocation criteria.

the time window for collocation is initially surprising, due to the observed speed of evolution of cloud properties. Additional SEVIRI and CALIOP CTTs were therefore collocated, for the full year of 2007, using both 60-ML-0 and 15-ML-0 collocation criteria. The 60-ML-0 criteria result in a maximum temporal distance between SEVIRI and CALIOP retrievals of 30 minutes, while the 15-ML-0 criteria result in a maximum temporal distance between retrievals of 7.5 minutes.

There is no significant change in either the magnitude or spatial distribution of the observed biases between the two cases (Fig. 3.4). However, by reducing the collocation window to 15 minutes, the number of collocated data points is reduced and the spatial patterns become less clear.

The biases shown in Fig. 3.4 consist of biases due to differences in the retrieval processes of the SEVIRI and CALIOP datasets (the retrieval bias) and to spatial and temporal differences in the scenes observed by the two instruments (the collocation bias).

If the size of the retrieval bias increased when moving from a 15-ML-0 to 60-ML-0, it would be expected that either the mean biases in Fig. 3.8 would be larger than those shown in Fig. 3.4, or, if the mean values are obscuring compensating errors (for example from observations before and after the CALIOP overpass), that the standard deviation of the retrieval biases in the 60 minute case would be larger than those in the 15 minute case. However, there is little difference between the two sets of maps (Fig. 3.5). This indicates that the size of the collocation biases does not increase significantly when using a 60 minute time window in place of a 15 minute window.

There are many reasons to think that the collocation bias may be small relative to the large retrieval biases seen in many parts of the SEVIRI disc. For example, over areas of stratiform cloud, CTT is unlikely to change significantly over the space of the extra 22.5 minutes allowed by a 60 minute collocation window. In more

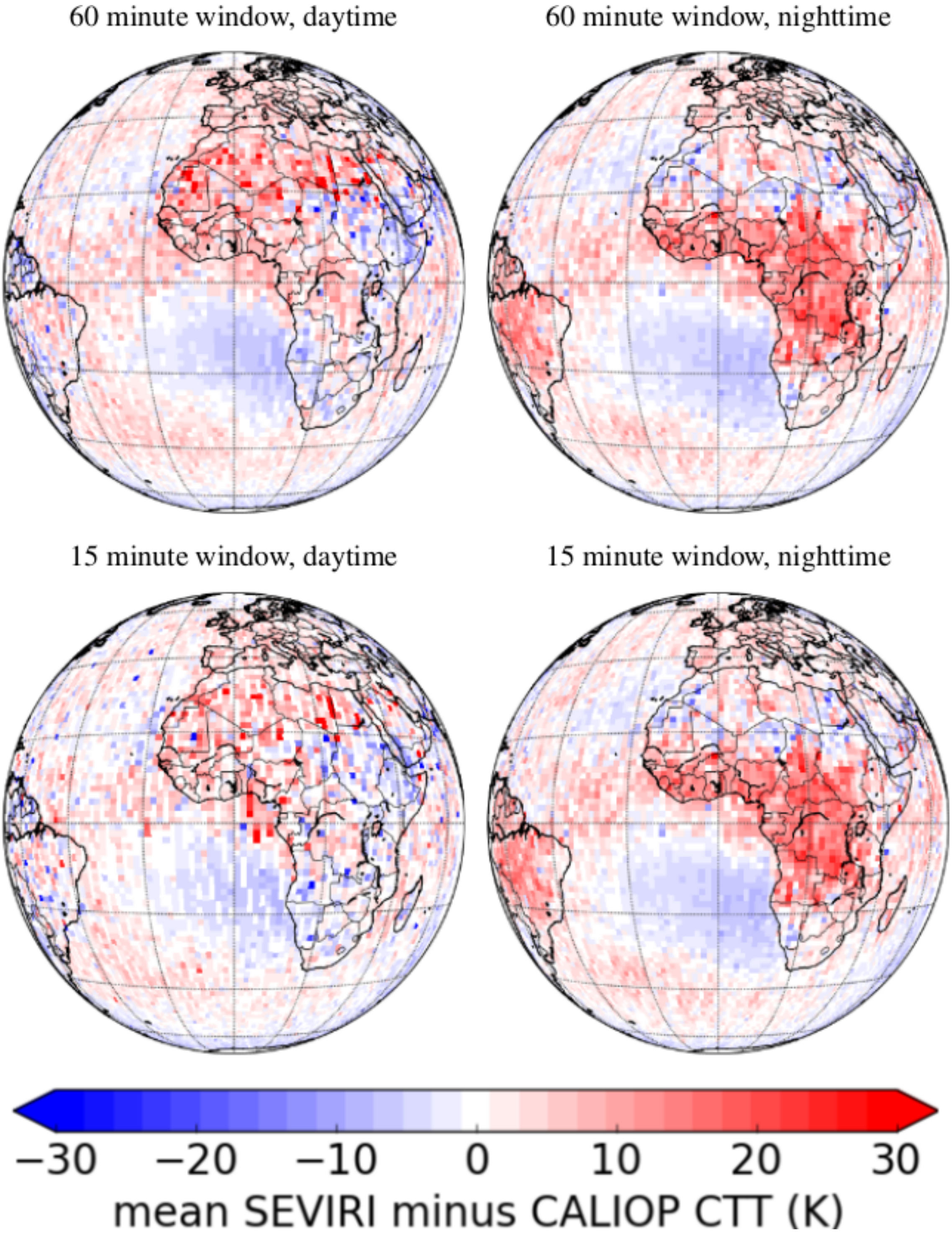

Figure 3.4: Spatial distribution of the bias in SEVIRI cloud top temperature retrievals during 2007, using a 15 minute collocation window. Biases are shown separately for both the day (13:30 LST CALIOP overpass) and nighttime (01:30 LST CALIOP overpass), using a 60 minute collocation window and a 15 minute collocation window.

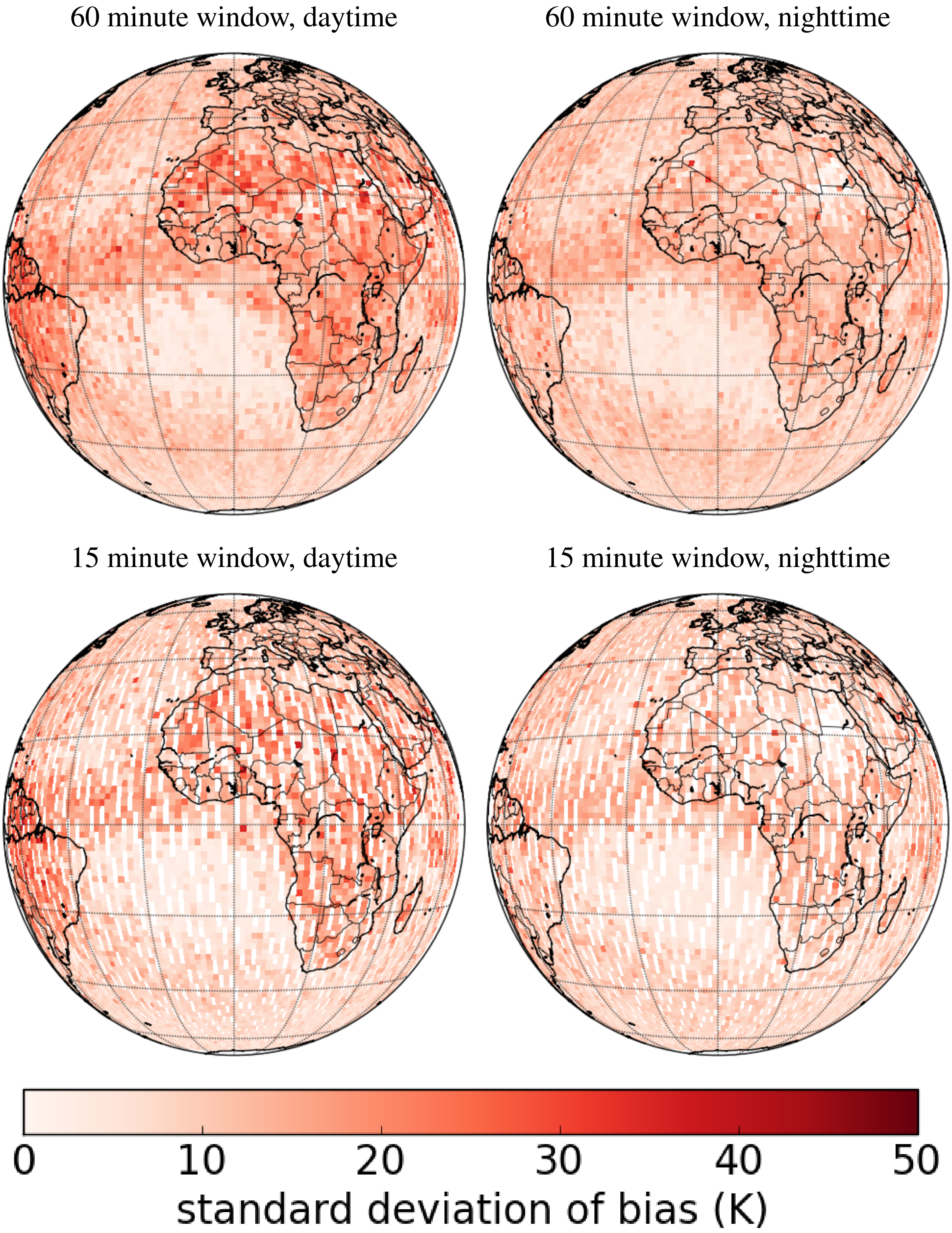

Figure 3.5: Spatial distribution of the standard deviation of the biases in SEVIRI cloud top temperature retrievals during 2007. Data are shown for both the day (13:30 LST CALIOP overpass) and nighttime (01:30 LST CALIOP overpass), using a 60 minute collocation window and a 15 minute collocation window.

convective areas, some clouds may develop significantly over the course of the larger time window, but the CTT of mature convective cloud systems and convective anvils will be more stable over time.

Additionally, as discussed in Section 3.3.2, the use of temperature profiles from reanalysis datasets in converting between CTH and CTT may introduce large biases between the two datasets. It is possible that the small difference in biases noticed between the two temporal collocation windows is due to the large contribution of this conversion process to the total bias observed.

As the size of the collocation bias does not increase significantly when using a 60 minute collocation window, and due to the significant reduction in the number of data points available for further analysis when using a 15 minute window, a temporal collocation window of 60 minutes was therefore chosen for this analysis.

The effects of applying different COD thresholds (60-ML-0, 60-ML-03, 60-ML-1, 60-ML-2) (in order to account for differences in the sensitivity of the SEVIRI and CALIOP instruments to low cloud optical depths) were also considered. It should be noted that these thresholds do not affect biases between the radiometric cloud top observed by SEVIRI and the physical cloud top observed by CALIOP.

Thresholds were applied to the COD of the top cloud layer as measured by CALIOP and scenes for which this top layer did not meet the threshold value were excluded from the analysis. This differs from the approach implemented by Benas et al. (2016), who compared CTT values for the first CALIOP layer at which the top-down, vertically integrated cloud optical depth exceeded the threshold value. The number of scenes containing cirrus cloud is therefore reduced in this analysis compared to that of Benas et al. (2016). This is likely to increase the weighting of statistics presented in Section 3.3.2 towards the southeast Atlantic ocean, where there are few cirrus clouds. However, it does not impact the weighting of statistics elsewhere in this study, where the data is not limited to retrievals which can be collocated to a

CALIOP overpass.

A comparison of mean SEVIRI day and nighttime retrieval biases (Fig. 3.6) with a similar plot in Benas et al. (2016) (Fig. 6-15, row 3, column 3) indicates that this difference in methodology does not lead to a large difference in the spatial distribution of the mean retrieval biases.

When no COD threshold is used, the mean bias for combined land and ocean data is 11 K (Fig. 3.2). This is reduced to a mean bias of 2.4 K when using a threshold of 0.3, a mean bias of 0.4 K for a threshold of 1 and a mean bias of -0.9 for a threshold of 2 (Fig. 3.2). Similar decreases in the RMSE were observed (Fig. 3.2).

The total mean and ocean-only biases are negative for the 60-ML-2 collocation criteria, while the land values display a slight positive bias (Fig. 3.2). This is due to the fact that the majority of the clouds in this dataset are located in the southeast Atlantic Ocean (Fig. 3.7), a region of prevalent subtropical subsidence inversions. In the presence of a low level thermal inversion there are two possible solutions to the problem of inferring the vertical placement of cloud tops from observed bright-

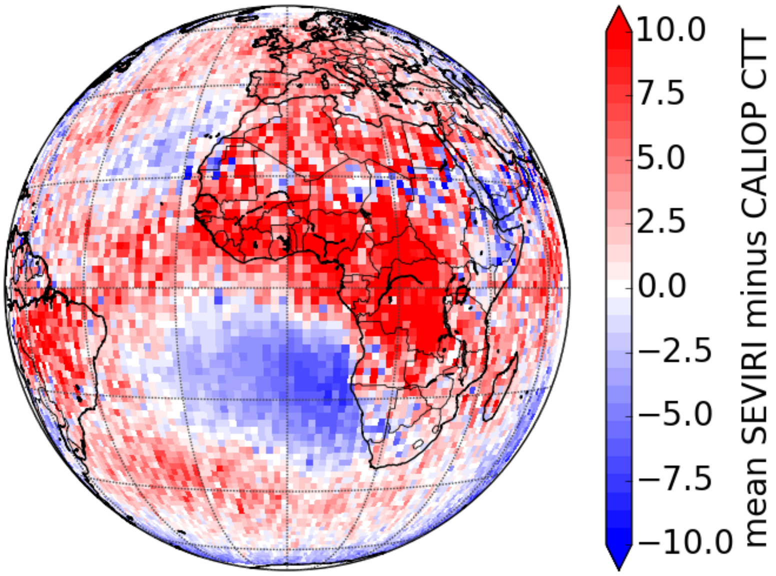

Figure 3.6: Spatial distribution of mean daytime (13:30 LST CALIOP overpass) and nighttime (01:30 LST CALIOP overpass) bias in SEVIRI CTT retrievals during 2007. This plot is the same as the 'Day and night' plot in Fig. 3.8, but plotted using the same scale as Fig. 6-15 in Benas et al. (2016) for ease of comparison.

ness temperatures. As explained in Section 3.2, the SEVIRI retrieval algorithm (NWCSAF/MSGv2012) places the cloud top for low clouds at the pressure level which corresponds to the best fit between observed and simulated brightness temperatures. In cases of low level thermal inversions, the SEVIRI retrieval generally places the cloud above the thermal inversion (Derrien 2013) and may therefore underestimate CTT in these areas. However, the CALIOP retrieval of CTT is based on direct observations of CTH and is therefore not subject to uncertainty with respect to the vertical placement of the cloud top in the first place (NASA 2013; Hamann et al. 2014). However, the vertical resolution of the model fields used to convert CALIOP CTH to CTT is relatively coarse, which may introduce some uncertainty in the CALIOP values themselves. If the latter effect is small, the difference in approach to the vertical placement of clouds in the presence of inversions would result in a systematic negative bias in the SEVIRI retrieval in this region.

Finally, the impact of excluding multi-layer cloud from the collocation is considered (60-ML-0, 60-SL-0, 60-ML-1 and 60-SL-1, Table 3.1). Excluding multi-layer cloud when no COD is used (60-SL-0) results in the mean bias falling from 11.1 K to 3.9 K and the mean RMSE falling from 26.3 K to 20.6 K (Fig. 3.2), indicating that in the case of multi-layer cloud scenes, observed cloud top brightness temperatures are likely contaminated by longwave emissions from lower-level clouds. However, once a COD threshold of 1.0 is applied, excluding multi-layer cloud (60-SL-1) results in a much smaller change in the bias from 0.4 K to -0.4 K, with the mean RMSE falling from 11.8 K to 10.9 K (Fig. 3.2). This shows that, when the top cloud layer observed by CALIOP has a COD greater than one, the brightness temperatures observed by SEVIRI are no longer significantly contaminated by longwave emissions from lower-level clouds. CALIOP scenes containing multiple layers of cloud were therefore included.

To summarize, for all further analyses presented in this paper, SEVIRI and CALIOP data were collocated using the 60-ML-1 criteria, consisting of a 60 minute collocation window, inclusion of scenes with multiple layers of cloud, and a COD threshold of 1.0. The resulting CTT retrievals from SEVIRI and CALIOP were compared for the full year of 2007, as follows. For each 5 by 5 km CALIOP pixel within the SEVIRI disc:

- the highest reported CALIOP cloud layer was selected;
- the SEVIRI pixel with the closest latitude and longitude to that of the CALIOP pixel was selected;
- for this pixel, the nearest SEVIRI retrieval in time (within the allowed 60 minute time window) was identified;
- if multiple CALIOP retrievals fell within a single SEVIRI pixel, the values were averaged. This was only necessary towards the edges of the disc, beyond approximately 50°E and 50°W;
- the retrieval bias (calculated as SEVIRI minus CALIOP CTT) was calculated for each instance of collocated data.

Retrieval biases

The annual mean bias in SEVIRI CTT, calculated across the entire SEVIRI disc from January to December 2007, combining both daytime and nighttime conditions, is 0.44 K with a standard deviation of 11.7 K (Table 3.2). This is smaller than the 2.1 K mean bias calculated by Benas et al. (2016). The difference is likely due to the fact that a less stringent COD threshold of 0.3 was applied by Benas et al. (2016), compared to the threshold of 1.0 used in this study.

Statistics calculated over both land and ocean, and under both day and nighttime conditions, show small mean biases and large standard deviations. Over the ocean the mean bias in SEVIRI CTT is -0.12 K, with a standard deviation of 10.5 K, but over land the mean bias rises to 2.38 K, with a standard deviation of 14.9 K (Table 3.2).

It should also be noted that the sign of the mean bias is negative over the ocean for both daytime and nighttime retrievals, although the bias is always positive over land. As discussed in Section 3.2, even once clouds with a low optical depth are filtered out, observations from SEVIRI are expected to detect a warmer radiometric CTT as compared to the colder physical CTT observed by CALIOP.

The spatial distribution of the number of fully cloudy pixels for which SEVIRI retrieved a CTT value and for which a corresponding CALIOP value was available during 2007 are shown in Fig. 3.7. Collocated retrievals are concentrated in the southeast Atlantic Ocean (Fig. 3.7), an area of almost perpetual cloudiness, where atmospheric inversions are prevalent. The negative biases over the ocean are again due to the different retrieval processes for SEVIRI and CALIOP with regard to the vertical placement of clouds in regions of atmospheric inversions (as discussed in Section 3.3.2).

Figure 3.8 shows the spatial distribution of mean SEVIRI minus CALIOP CTT for daytime, nighttime, day and nighttime combined, and the difference between night

Surface type	**Time of day**	**Number of retrievals (10^6)**	**Mean bias (K)**	**Standard deviation of bias (K)**
land and ocean	day and night	2.79	0.44	11.7
	day	1.34	0.05	12.2
	night	1.45	0.80	11.2
land	day and night	0.63	2.38	14.9
	day	0.32	0.72	16.0
	night	0.31	4.11	13.5
ocean	day and night	2.16	-0.12	10.5
	day	1.02	-0.16	10.7
	night	1.14	-0.10	10.4

Table 3.2: Summary of evaluation results for the 60-ML-1 collocation criteria, showing: number of collocated SEVIRI retrievals, mean bias (SEVIRI minus CALIOP CTT) and standard deviation of the bias. Statistics are reported separately for day, night, land and ocean retrievals.

and daytime biases. It can immediately be seen that for both day and night time retrievals, there are large areas of very high mean bias, although, due to compensating biases, these are obscured in some areas when day and nighttime biases are plotted together (Fig 3.8). SEVIRI is shown to generally overestimate CTT over land, by between approximately 10 and 20 K during the day and between 15 and 25 K (or more) at night (Fig. 3.8). These values are larger than those reported by Benas et al. (2016) who do not consider day and nighttime biases separately. However, these biases are in agreement with the expected discrepancy of 0.5-3.0 km (approximately 3-20 K assuming a 6.5 K/km lapse rate) between radiometric and physical cloud top height (as discussed in Section 2.2.2).

Over the ocean, biases are relatively small. Under both day and nighttime conditions CTT is underestimated by between 5 and 10 K over large areas of the Atlantic ocean, while in other areas, such as the region of trade wind convergence, SEVIRI

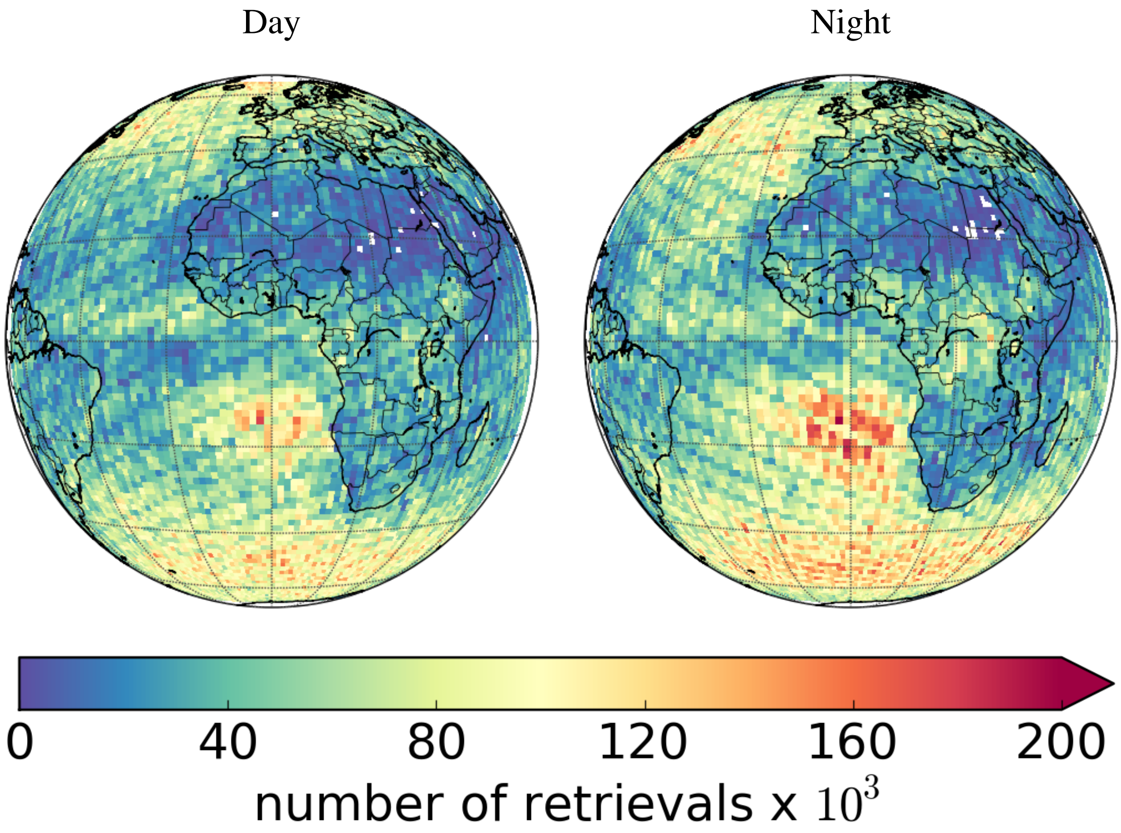

Figure 3.7: Spatial distribution of the number of collocated SEVIRI and CALIOP retrievals in 2007, shown separately for daytime and nighttime conditions.

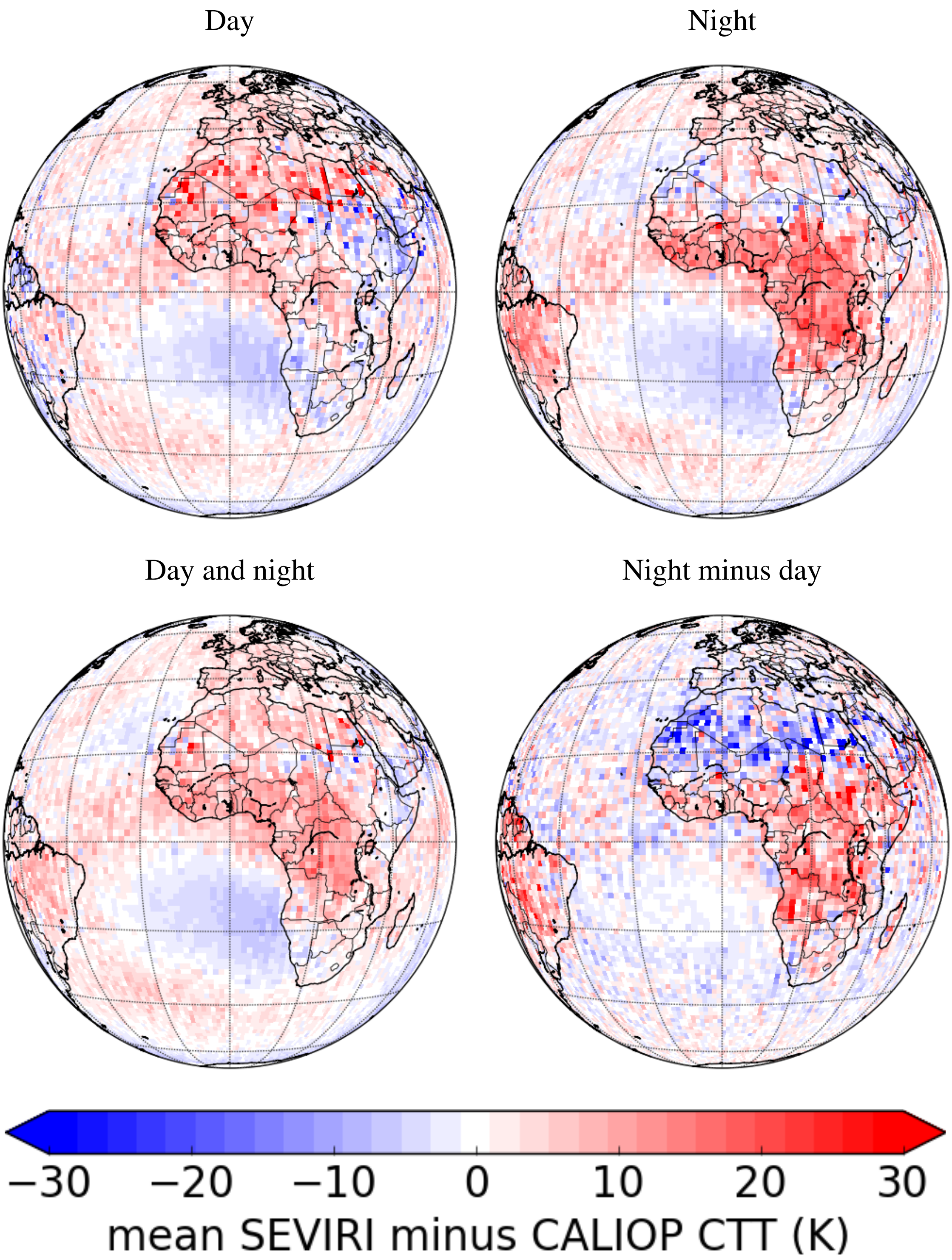

Figure 3.8: Spatial distribution of the bias in SEVIRI cloud top temperature retrievals during 2007. Biases are shown for the day (13:30 LST CALIOP overpass), night (01:30 LST CALIOP overpass), mean of both day and night biases, and for the difference (night minus day) between night and daytime biases.

overestimates CTT by between 5 and 15 K (Fig. 3.8).

The large areas of slightly negative bias in the Atlantic ocean correspond to areas of persistent atmospheric inversion. As explained previously, the small systematic bias in the SEVIRI CTT retrieval in this region is due to its treatment of subsidence inversions. As can be seen from Fig. 3.7, the majority of the collocated retrievals are located in this region. Therefore, the mean biases presented in Table 3.2 are heavily weighted towards the small negative biases in this region.

The difference in the magnitude of the biases over land and ocean is likely due to differences in the most common cloud regimes, with deep convection being more common over land and stratiform cloud more common over the ocean (Yang and Slingo 2001; Schröder et al. 2009), as well as the greater difficulty in accounting for variations in surface emissivity over land (Derrien 2013). As suggested by Sherwood et al. (2004) and Stubenrauch et al. (2013), the differing extinction profiles and vertical heights of convective and stratiform clouds results in larger differences between the radiometric and physical cloud top for tall convective clouds.

Unfortunately, it is not possible to fully characterize the diurnal variation in bias, as CALIOP data is only available for comparison at 01:30 and 13:30 LST. However, the two CALIOP overpasses can give at least an estimate of the potential size of this variation. For the purposes of this study, a bias in CTT which remained constant throughout the day would not be a barrier to quantifying either the amplitude of the diurnal cycle in CTT, or the average time of minimum CTT. However, the fact that biases can change dramatically from the day to nighttime overpasses of CALIOP is more problematic.

Both the mean values and the spatial distribution of the biases change significantly from day to night. Differences between mean nighttime and daytime biases in the SEVIRI CTT retrieval can be as large as 30 K in some areas (Fig. 3.8). There are strong positive differences over Sub-Saharan Africa and South America, with strong negative differences over the Sahara. Differences between night and daytime biases are generally smaller over the ocean and over Europe. In areas where the difference between daytime and nighttime biases (Fig. 3.8) is greater than, or equal to the observed magnitude of the diurnal cycle in CTT, the diurnal cycle observed from the retrieval may be a product of diurnal variability in the accuracy of the retrieval. It will therefore be necessary to consider the diurnal variability in retrieval bias when quantifying the diurnal cycle of CTT.

3.3.3 Diurnal cycle of cloud top temperature

The CLAAS-2 monthly mean diurnal cycle product was used to calculate three-month mean diurnal cycles of CTT across the SEVIRI disc. Data were averaged for the period 2005-2015 to produce a climatological diurnal cycle with a temporal resolution of one hour, on a spatial grid of 0.25°. Ten years of data were required in order to produce relatively smooth diurnal cycles, particularly over land, where cloud retrievals were relatively sparse.

An example of the resulting diurnal cycle in CTT is shown in Fig. 3.9 for a grid box centred on 3.1°S, 16.4°E, (western Democratic Republic of the Congo, see cross in Fig. 3.13) for the months of September, October and November (SON). The amplitude of the diurnal cycle in CTT was calculated as the maximum minus minimum diurnal mean CTT, as shown by the arrow indicating an amplitude of 30 K. The local solar time of the minimum CTT was defined as the time at which the minimum daily mean CTT occurred, as shown by the dashed line at 19:00 local solar time (LST).

While the averaging process produced a coherent diurnal cycle in the majority of cases, the calculated diurnal cycle remained very noisy in a few areas, particularly during seasons when very few clouds were retrieved. The number of CTT retrievals is greatest over areas of the ocean where large, homogeneous stratiform cloud fields result in a large number of cloud-filled pixels and hence a large number of SEVIRI CTT retrievals, and in the region of the ITCZ, where convective cloud is concentrated (Fig. 3.10). In areas with very few cloud retrievals, such as the Sahara in all seasons and parts of southern Africa in JJA (Fig. 3.10), it will not be possible to accurately calculate a diurnal cycle of convection.

Maps of the amplitude of the diurnal cycle in SEVIRI CTT (Fig. 3.11), calculated as shown in Fig. 3.9, show the smallest amplitudes located over the southeast Atlantic ocean in all seasons. Over the course of a typical day, stratocumulus cloud tops vary by less than 5 K in this region. Amplitudes increase to between 20 K and 30 K in the trade wind region, where there are more convective clouds. Over Africa and South America amplitudes generally range between 20 K and 50 K, with the seasonal changes tracking the movement of the ITCZ, seen as a migrating band of cold cloud tops in Fig. 3.1. The diurnal cycle is smaller in Europe where amplitudes

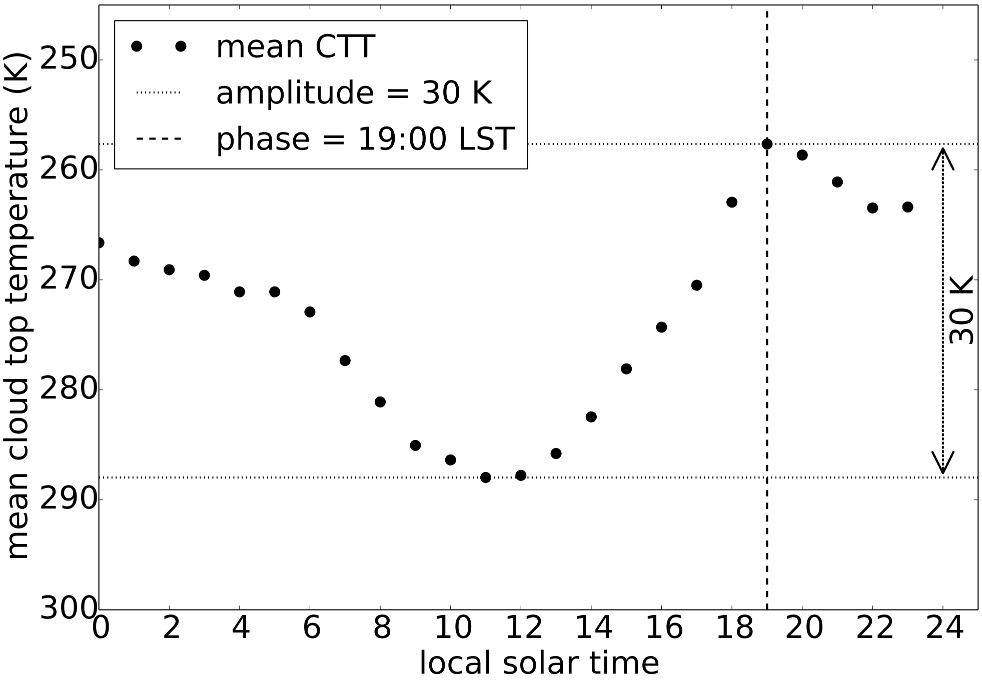

Figure 3.9: Seasonal mean climatological (September, October, November, 2005 - 2015) diurnal cycle of CTT at 3.1°S, 16.4°E, (western Democratic Republic of the Congo, see cross in Fig. 3.13). The amplitude of the diurnal cycle (defined as minimum minus maximum CTT) and the phase (defined as the local solar time (LST) of minimum CTT) are also illustrated.

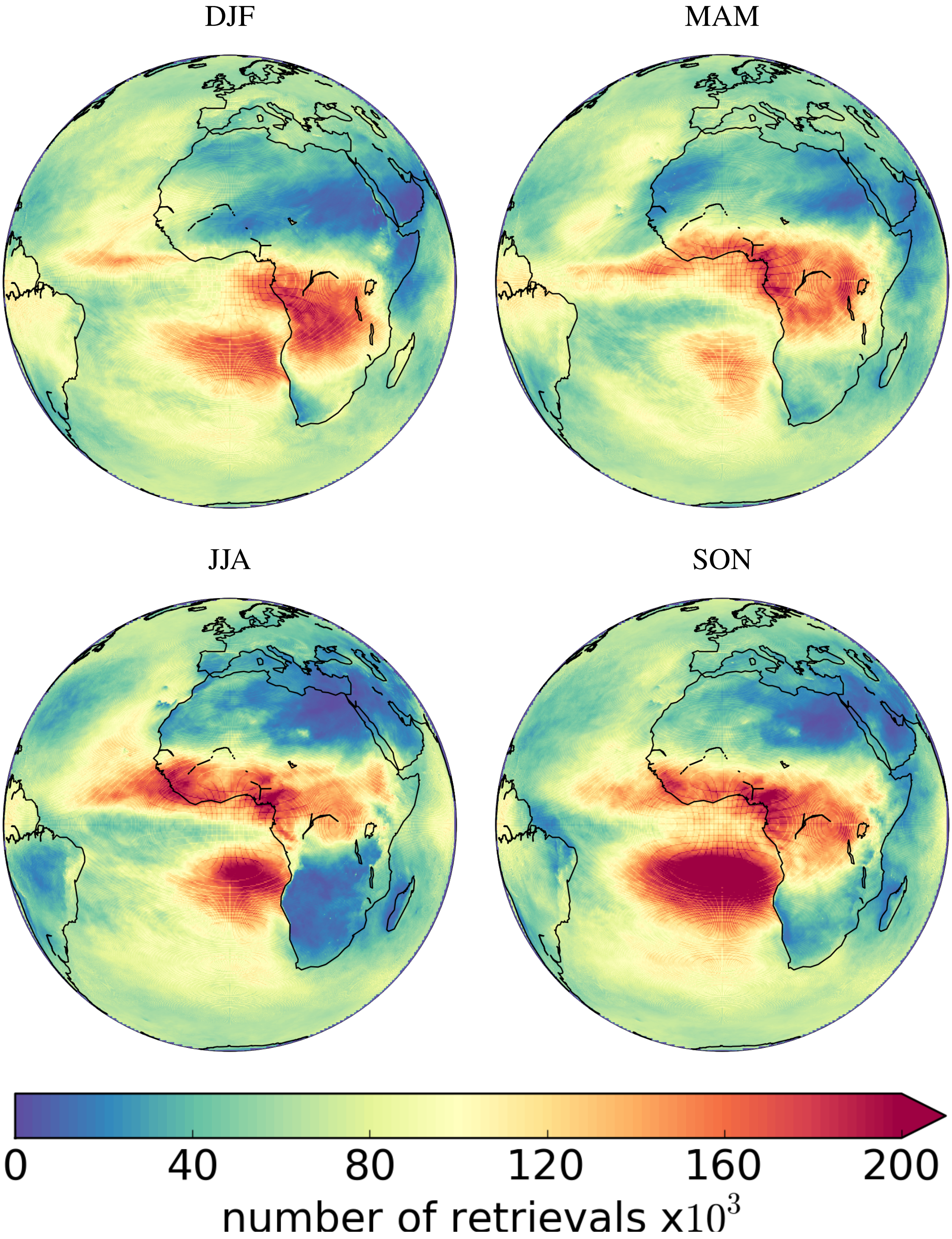

Figure 3.10: Spatial distributions of the total number of SEVIRI cloud top temperature retrievals available from the CLAAS-2 dataset during the period 2005-2015. Values are shown for each season.

range from 15 K in the north during DJF to 50 K in the Mediterranean during JJA.

For illustrative purposes, amplitudes of the diurnal cycle in CTT were plotted for areas with few CTT retrievals, but regions with retrievals at less than 15% of the processed time steps are indicated (Fig. 3.11). With the exception of southern Africa in JJA, these regions correspond to areas of predominantly desert and calculated amplitudes tend to be very large. Amplitudes exceed 60 K in areas of the Sahara and Namibian deserts in all seasons, as well as in Somalia during the December to March dry season (Higgins et al. 1978) and southern Africa during the May to September dry season (Higgins et al. 1978) (Fig. 3.11). The large amplitudes observed in these areas are likely to be caused by a mixture of insufficient data (Fig. 3.10) and, particularly in the Sahara, by a large variation in the size of the retrieval bias between night and daytime conditions (Fig. 3.8).

In order to consider the effects of systematic differences in day and nighttime CTT retrieval biases in the SEVIRI dataset, the ratio of the amplitude of the diurnal cycle (Fig. 3.11) to the diurnal variability in the retrieval bias (Fig. 3.8) was calculated. In regions where this ratio is low, differences between systematic retrieval biases under day and nighttime conditions may contribute strongly to the amplitude of the observed diurnal cycle in CTT. A threshold value of 5 was chosen for this ratio, as indicative of regions in which observed diurnal cycles in CTT may simply be artefacts of the diurnal variation in retrieval errors. Areas for which the ratio falls below this threshold are indicated in Fig. 3.11.

Maps of the phase of the diurnal cycle, defined at each grid box as the local solar time at which the minimum three-monthly mean CTT occurs (Fig. 3.9) are shown in Fig. 3.12. Regions with few clouds, or where diurnal variability in retrieval bias may significantly contribute to the observed diurnal cycle are illustrated in Fig. 3.12, as described for Fig. 3.11.

Over large areas of the ocean, minimum CTTs are observed at around 16:00 (Fig.

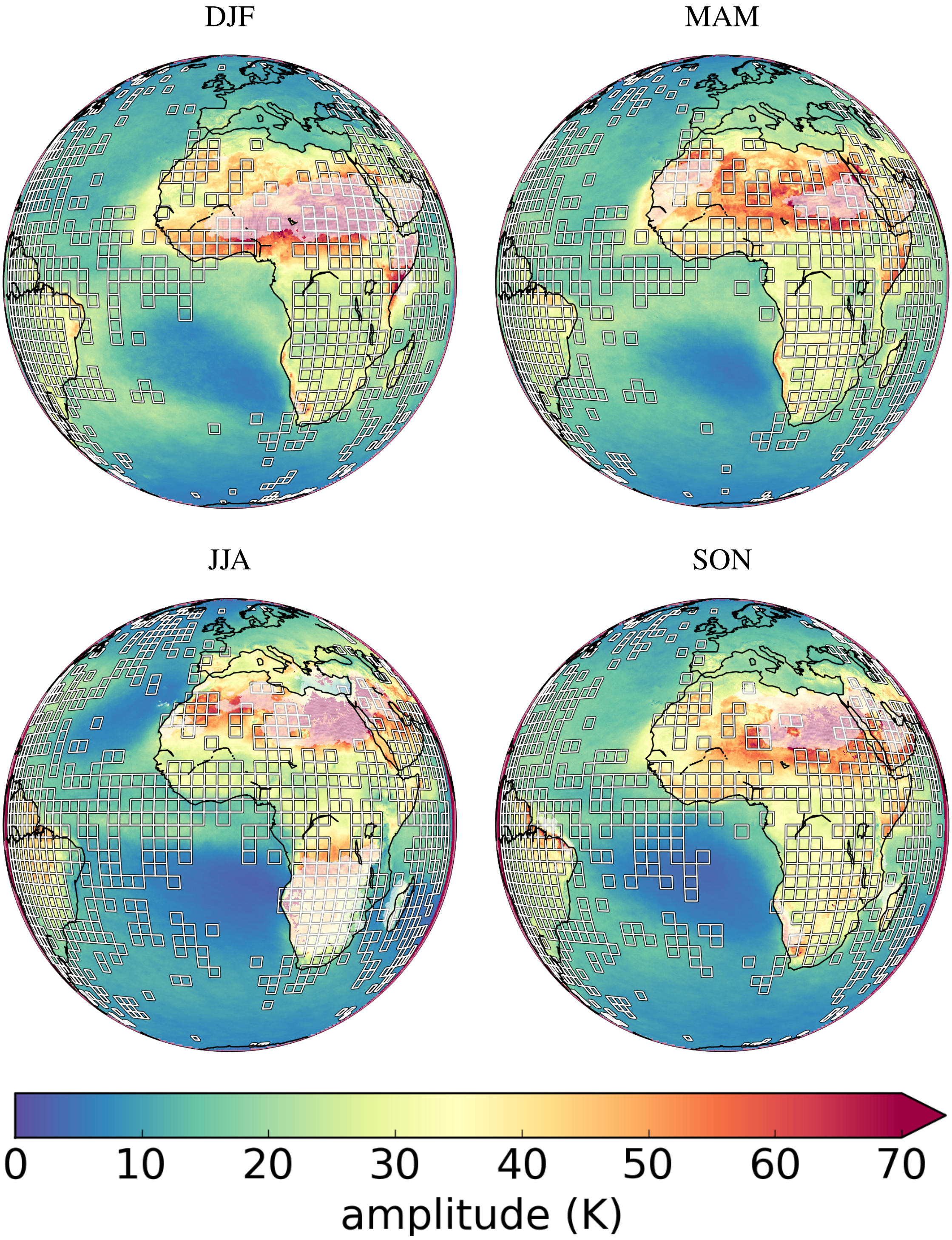

Figure 3.11: Seasonal mean amplitude of the diurnal cycle in SEVIRI cloud top temperature for the period 2005-2015. The white overlay indicates regions where retrievals are available for fewer than 15% of the processed timesteps. Squares indicate regions where the ratio of the amplitude of the diurnal cycle in CTT to the diurnal variability in CTT retrieval bias is less than 5.

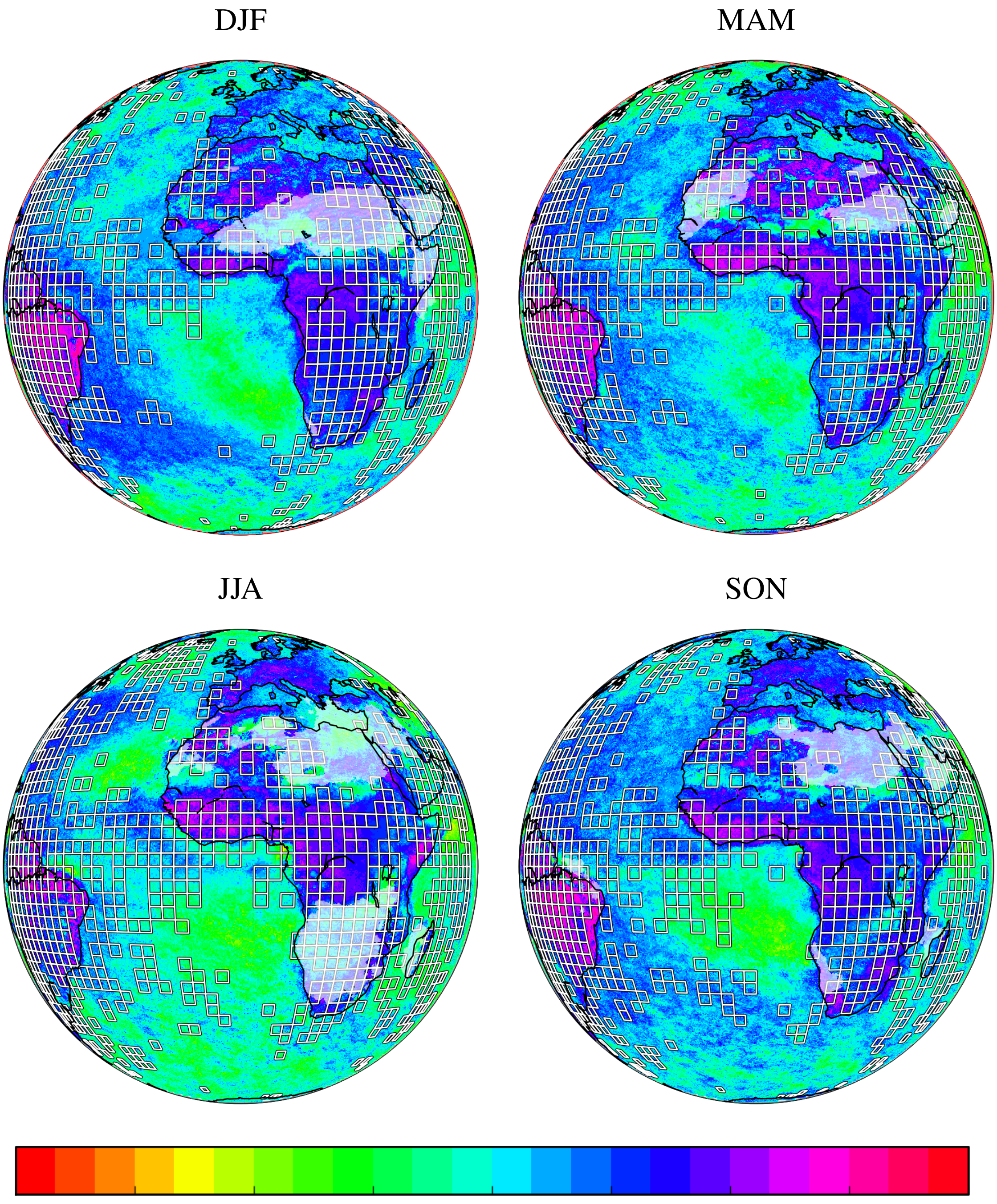

Figure 3.12: Seasonal mean phase (local solar time of minimum climatological mean CTT) of the diurnal cycle in cloud top temperature for the period 2005-2015. The white overlay indicates regions where retrievals are available for fewer than 15% of the processed timesteps. Squares indicate regions where the ratio of the amplitude of the diurnal cycle in CTT to the diurnal variability in CTT retrieval bias is less than 5.

3.12), possibly due to the initiation of convective cloud in the afternoons. In the southeast Atlantic however, where the predominant cloud type is stratiform, the minimum is observed in the morning, at around 09:00 (Fig. 3.12).

In South America, minimum CTT generally occurs at around 20:00. Over Sub-Saharan Africa and Europe the minimum is generally observed at around 16:00, with some areas, particularly West Africa, the Sahel and parts of the Congo Basin, showing later peaks at around 18:00. These later peaks broadly track the movement of the ITCZ (Fig. 3.1) and could be due to more vigorous convection, persisting until later in the day. It could also be due to a mixture of different convective cloud types, including organised MCSs which can persist until the early morning and more isolated local convective cells which peak in the afternoon (Rickenbach et al. 2009; Pfeifroth et al. 2016).

Areas with few cloud retrievals, such as the Sahara desert in all seasons, and southern Africa in JJA, are noisier (Fig. 3.12). This may be due to the fact that there is simply not enough data in these regions to meaningfully diagnose the phase of the diurnal cycle in CTT. However, the regions with the fewest retrievals (Fig. 3.7 and Fig. 3.12) do not match exactly the regions of noise in Fig. 3.12. This indicates that the noise may also be caused by a mixture of different cloud types with different diurnal cycles.

The relationship between the observed amplitude and phase of the diurnal cycle and the retrieval biases presented in Section 3.3.2 were examined in more detail over the Sahara, central Africa and southeast Atlantic ocean. These areas were chosen because they all exhibit fairly consistent patterns of both retrieval bias and observed diurnal cycle properties and were designed to cover approximately $9\text{x}10^6$ km^2 each. They also provide examples of desert, rainforest and ocean surface types. The locations of these three areas are illustrated in Fig. 3.13.

Seasonal mean SEVIRI diurnal cycles and retrieval biases for each of the regions in

Fig. 3.13 were compared (Fig. 3.14). It has already been shown that the SEVIRI dataset has different retrieval biases under daytime and nighttime conditions (Section 3.3.2), due to differences in solar illumination, cloud types, the availability of visible channel observations and, subsequently the exact retrieval algorithms used. Seasonal mean times of sunrise and sunset are therefore indicated for each region and mean retrieval biases, as calculated in Section 3.3.2 for the year 2007, are shown for both day and nighttime CALIOP overpasses.

In the southeast Atlantic Ocean, the bias is shown to be very small with no apparent diurnal cycle in the bias (Fig. 3.14). Mean CTTs reach a minimum at around 09:00 and persist until 16:00 in the DJF and March, April and May (MAM) seasons. In JJA the cold clouds are more short-lived and in SON CTTs remain constant throughout the day. Mean CTTs are warm at around 280 K in JJA and SON and 270 K in DJF. However, mean CTTs are colder, at around 250 K in MAM. The cold

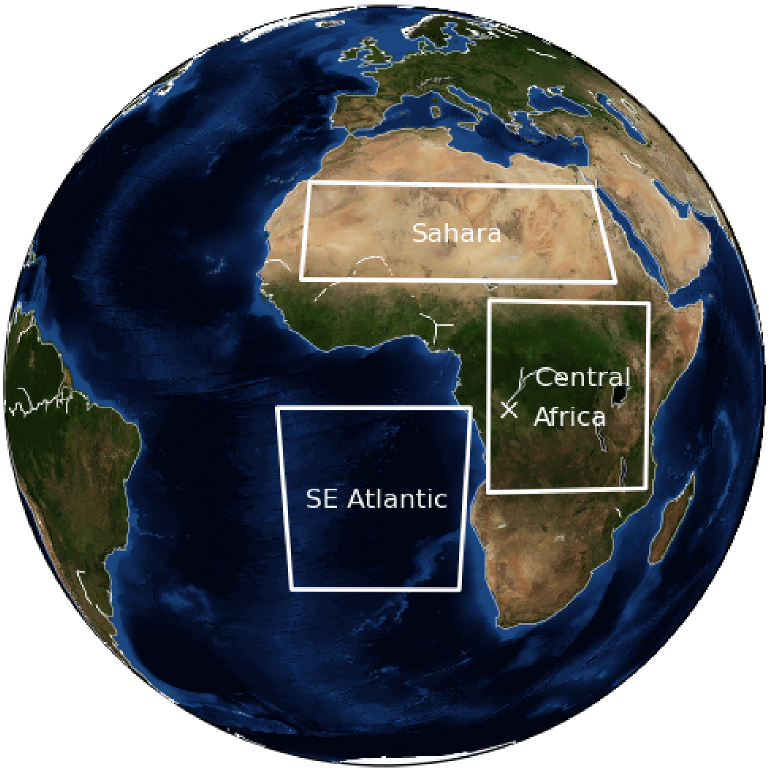

Figure 3.13: Map of the area observed by SEVIRI showing true-colour surfaces, major rivers and lakes. Labelled boxes show the locations of the regions used in Fig. 3.14. The white cross shows the location of the data used in Fig. 3.9.

mean temperatures in MAM and to a lesser extent, those in DJF may be due to the inclusion of regions with large numbers (Fig. 3.1) of cold clouds (Fig. 3.10) in the region defined as the southeast Atlantic for the purposes of this study (Fig. 3.13). Fig. 3.1 shows that seasonal mean CTTs in the centre of the southeast Atlantic region are closer to 280 K in all seasons.

In the Sahara, the amplitude of the diurnal cycle is almost 20 K, with a small diurnal cycle in the bias of around 5 K (Fig. 3.14). The warmest CTTs are observed at 05:00 and at noon, with the coldest cloud at 07:00 and 18:00. Although the diurnal cycle in the bias is less than the amplitude of the diurnal cycle, the bias results in CTTs retrieved during the day being too warm, indicating that a significant fraction of the amplitude observed over the Sahara may be due to differences between the day and nighttime conditions and hence the differences in the retrieval algorithms

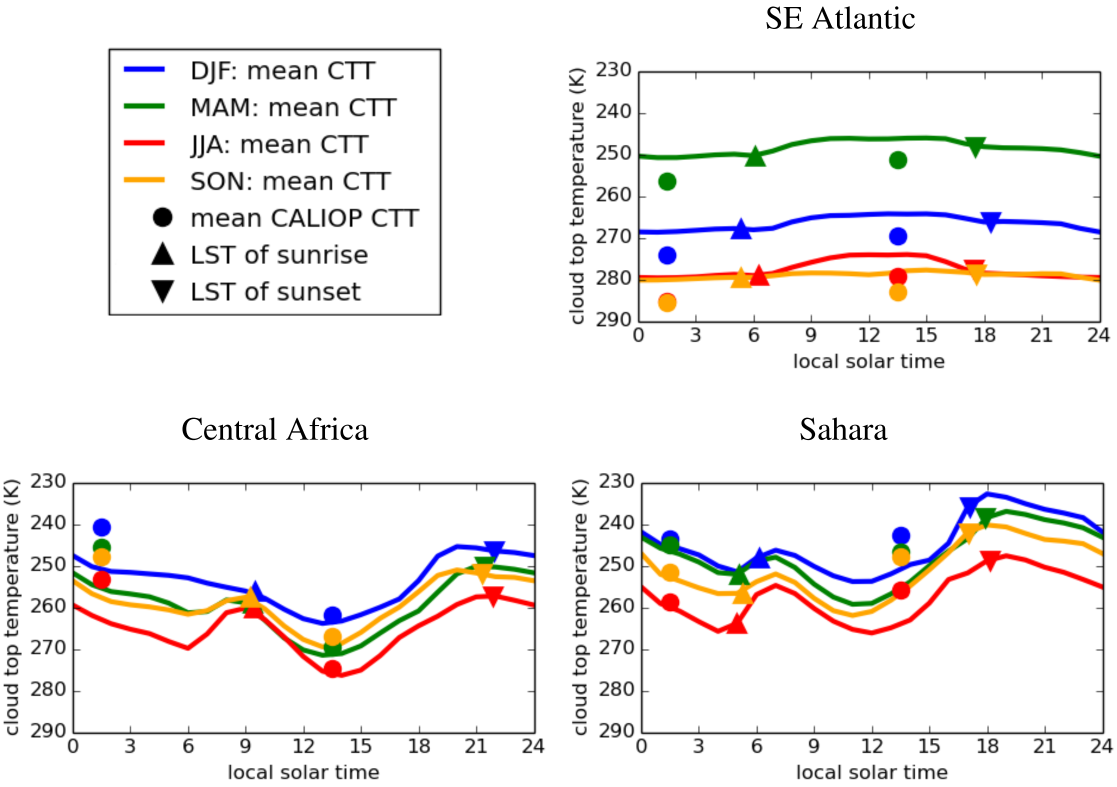

Figure 3.14: Seasonal mean diurnal cycles of SEVIRI CTT calculated over the period 2005-2015 (solid lines) and mean 2007 SEVIRI minus CALIOP retrieval bias (vertical distance between coloured circles and corresponding coloured lines). Biases are shown at the mean LST for the day and nighttime CALIOP overpasses. Also shown are the local solar times of sunrise (triangles) and sunset (nablas) for each region and season.

applied. Sudden changes in mean CTT around the times of sunrise and sunset in the Sahara are also seen in Fig. 3.14. In all seasons there is a secondary minimum in cold CTTs at around 06:00, about an hour before sunrise. This secondary minimum may indicate the presence of MCSs, or simply a change in values due to the change in retrieval algorithm at this point.

In central Africa, the diurnal cycle in the bias is around 7 K and the amplitude of the diurnal cycle is around 15 K throughout the year (Fig. 3.14). The warmest cloud is observed at 14:00, with the coldest cloud between 20:00 in DJF and 22:00 in JJA. There is a secondary minimum at 09:00 in all seasons except DJF, which may be caused by the presence of MCS, although it is also possible that this secondary peak is produced by the switch from night to daytime retrieval conditions. In contrast to the Sahara however, the diurnal cycles in retrieval bias create a smaller amplitude of the diurnal cycle in CTTs than would otherwise be observed. This size of the bias during the early morning may indicate a larger difference between the radiometric cloud top measured by SEVIRI and the physical cloud top measured by CALIOP due to differences in cloud types throughout the day. While the ratio of the diurnal cycle in mean CTT to the difference in retrieval biases is small, it appears that in this region the difference in the retrieval bias is acting to reduce, rather than increase, the observed diurnal cycle in CTT.

It is interesting to note that the broad shape of the diurnal cycle curves in the Sahara and central Africa are similar, although the post-sunrise increase in CTT is delayed in central Africa relative to the Sahara. However, the reasons for the time lag between diurnal cycles of CTT in central Africa and the Sahara are not known.

3.4 Conclusions

This chapter evaluated SEVIRI CTT data against CALIOP and attempted to quantify spatial and diurnal variabilities in retrieval biases. The amplitude and phase of the diurnal cycle in CTTs, as observed by SEVIRI were also quantified. Comparing measurements of the diurnal cycle in mean CTT and retrieval bias, it is shown that diurnal variations in the retrieval bias are often of the same order of magnitude as the amplitude of the observed diurnal cycle. This indicates that observed diurnal cycles may be artefacts of retrieval bias in some regions. Areas in which there was insufficient data to accurately calculate the diurnal cycle in CTT, or in which the observed cycle was an artefact of retrieval biases, were identified.

SEVIRI and CALIOP data were collocated using a 60 minute collocation window and a COD threshold of 1.0. Scenes with multiple layers of cloud were included. By collocating SEVIRI and CALIOP CTT retrievals for the whole year of 2007, it is shown that mean errors in the SEVIRI retrieval can vary from less than 5 K to more than 30 K across the SEVIRI disc, and by up to 30 K between the daytime and nighttime overpasses of CALIOP. However, mean errors across the SEVIRI disc are small, at approximately 0.44 K with a standard deviation of 11.7 K. This shows the importance of considering spatial and diurnal variations in retrieval error when using this dataset.

This study shows that the difference between the radiometric cloud tops observed by SEVIRI and the physical cloud tops observed by CALIOP may account for a significant fraction of the biases found in this analysis. As explained in Section 2.2.2, previous studies indicate that biases of less than 0.5-3.0 km (approximately 3-20 K) could potentially be explained by this difference, even for optically thick clouds. As cloud layers with an optical depth of less than 1.0 were not included in the comparison of SEVIRI and CALIOP CTT data, biases are expected to be largest in the case of optically thick clouds with poorly defined edges, such as glaciated clouds. In addition, the small negative bias observed over the southeast Atlantic Ocean is likely related to uncertainties introduced by the use of models to estimate the vertical placement of clouds for both SEVIRI and CALIOP datasets. Additional biases described in this paper may be due to retrieval errors included in the SEVIRI dataset, or due to the introduction of errors due to the use of reanalysis dataset temperature profiles to convert between CTH and CTT. As discussed in Section 3.3.2 this conversion may introduce significant errors in the vertical positioning of cloud layers and could potentially by the dominant source of bias. It is however outside the scope of this study to quantify this potential bias.

Keeping these uncertainties in mind, the seasonal, diurnal and spatial variation of CTTs were quantified across the SEVIRI disc. By analysing the seasonal mean amplitude and phase of the diurnal cycle in CTT, it is shown that SEVIRI is able to capture details of the diurnal cycle of convection, across several continents. It is shown that the CLAAS-2 dataset measures the diurnal cycle of cloud tops accurately in regions of stratiform cloud such as the southeast Atlantic and Europe, where retrieval biases are small and exhibit limited spatial and temporal variability. Quantifying the diurnal cycle over the tropics and regions of desert is more difficult, as biases are larger and more variable.

Looking at three areas in detail (the southeast Atlantic Ocean, the Sahara desert and Central Africa), the relationships between the diurnal cycle in CTT and retrieval biases is analysed. It is shown that retrieval biases in the southeast Atlantic are small enough to detect a small but persistent diurnal cycle of approximately 5 K in the area, with cold clouds peaking between 11:00 and 15:00 local solar time. However, the CLAAS-2 dataset is shown to be of limited skill in measuring the diurnal cycle over the Sahara, which may be due to generally low cloud cover in desert regions and a possible dominance of optically thin clouds such as cirrus outflow from tropical convection when clouds are present. In the Sahara, variability in the bias appears to contribute to an excessively large amplitude of the diurnal cycle, with a large amount of spatial and seasonal variability in the phase. In tropical regions such as Central Africa, a relatively large variability in the retrieval biases appears to dampen the signal from a very strong observed diurnal cycle, with minimum CTTs occurring consistently between 20:00 and 22:00.

While this study highlights the importance of considering spatial and diurnal variations in retrieval errors when using SEVIRI data, it is also the case that observations from passive imagers in geostationary orbit provide valuable observations of the temporal and spatial variability of cloud on scales which are not available from polar-orbiting satellites such as CALIOP. These results should therefore be seen as guidance for the observation and modelling communities when using SEVIRI cloud top properties, particularly for studies considering the diurnal cycle of cloud top properties.

4 | The Lifecycle of Convective Cloud Cores and Anvils

4.1 Introduction

As discussed in Section 2.3.2, while the broad features of convective cloud lifecycles are well understood, the variability of convective cloud properties such as time of convective initiation, cloud lifetime, and speed of development are not well characterised on the global scale. This is particularly true over the African continent, where observational data on convection is sparse (Washington et al. 2013).

The majority of published studies on convective cloud lifecycles are based on static datasets (Peng et al. 2014, 2016; Zipser et al. 2006; Igel et al. 2014; Igel and van den Heever 2015; Deng et al. 2016), while those studies which focus on dynamic convective cloud lifecycles are often limited to a small area, or period of time (Bouniol et al. 2016; Fiolleau and Roca 2013b; Tadesse and Anagnostou 2010; Futyan and Del Genio 2007b; Bedka et al. 2010). However, new convection-tracking tools, using the high time-resolution data available from SEVIRI make it possible to study the lifecycle of individual convective cloud objects.

This section uses the cloud tracking algorithm Cb-TRAM (introduced in Section 2.2.4) to study the evolution and lifecycle of convective cloud cores and, through the use of a watershedding technique, their associated anvils. It aims to quantify the lifecycle of convective cloud and the evolution of convective cloud properties over a large area (sub-Saharan Africa) and period of time (four months in 2007).

The data and methodology used to create a dataset of tracked convective cloud cores and anvils are introduced in Section 4.2. An overview of the resulting dataset is given in Section 4.3.1. The evolution of convective cloud morphology is examined in Section 4.3.2 and the lifecycle of convective clouds is examined in Section 4.3.3. Conclusions are presented in Section 4.4.

4.2 Method

The Cb-TRAM algorithm (Zinner et al. 2008; Merk and Zinner 2013) (introduced in Section 2.2.4) was used to locate and track areas of cloud which display rapid vertical development over the 15 minute timestep observed by SEVIRI. It should be noted that the tracked objects relate to regions of vertically developing cloud, at a scale resolvable by the Cb-TRAM algorithm, which has a minimum resolution of 2 SEVIRI pixels, or around 32 km^2. Therefore, these tracked objects do not correspond to individual convective updrafts, which are too small to be resolved by the SEVIRI instrument. At the same time, a large, organised convective system is likely to have multiple regions of convective updraft, which may interact with each other. As long as these regions of updraft are separated by at least two SEVIRI pixels, Cb-TRAM will consider these regions of updraft as separate objects.

The objects tracked by Cb-TRAM should therefore be understood as regions of contiguous convective updraft, rather than convective cloud systems, or individual convective updrafts. For clarity these tracked objects will be referred to in this section as ‘cores’.

Cb-TRAM further classifies its cores into three stages of development. Stage one corresponds to initiating convective cloud, exhibiting rapid development in the lower troposphere, stage two refers to developing convection, showing rapid development in the upper troposphere, while stage three corresponds to cores which have reached the tropopause and potentially developed regions of anvil outflow. For the subset of tracked cores which reach stage three, a watershedding technique was used to assign regions of anvil cloud to each tracked core. Convection at all three stages of development is considered in the following analysis. However, clouds are only assigned an anvil component during the stage three phase of their development.

The watershedding technique (Bradski 2000) is applied to the 10.8 μm brightness temperature field (Fig. 4.1a). Areas of cloud are identified by applying the cloud mask from the CLAAS-2 product (Benas et al. 2016) to SEVIRI's 10.8 μm brightness temperature field (Fig. 4.1b). Areas of warm cloud are excluded by applying a threshold of 260 K to this field (Fig. 4.1c).

Previous studies have used a variety of brightness temperature thresholds, typically between 208 K and 255 K, to distinguish regions of anvil cloud (Houze et al. 2000; Futyan and Del Genio 2007a; Pope et al. 2008; Tadesse and Anagnostou 2010; Goyens et al. 2012; Bennartz and Schroeder 2012). In combination with the CLAAS-2 cloud mask, the 260 K threshold chosen for this study allows for the inclusion of as large an area of potential anvil cloud as possible at this stage in the watershedding process, while still excluding brightness temperatures which clearly correspond to warmer cloud types, or areas of surface.

The resulting field of cold cloud (Fig. 4.1c) is divided up among the stage three cores tracked by Cb-TRAM. This is achieved by treating the brightness temperature field as a topographic surface, where cold pixels correspond to topographical minima. The locations of the stage three cores from Cb-TRAM are used as markers, identifying some of these local minima as belonging to specific cloud cores (Fig. 4.1d).

The watershedding process can most easily be understood by considering each local minima as the bottom of a basin. For any basin containing a Cb-TRAM core, the

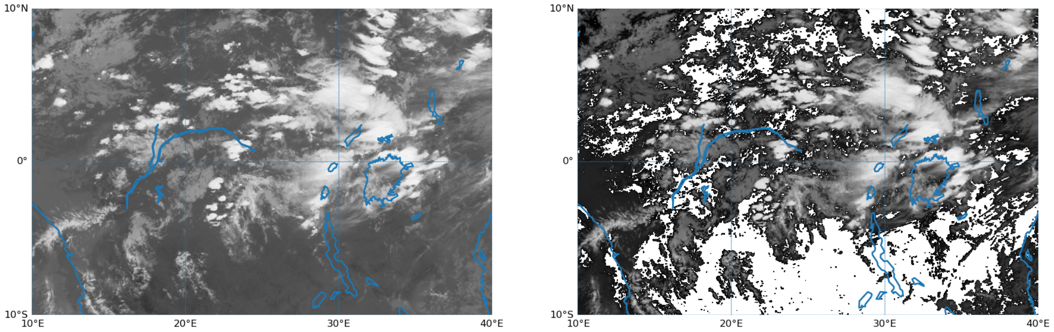

(a) 10.8 μm brightness temperatures (b) CLAAS-2 cloud mask

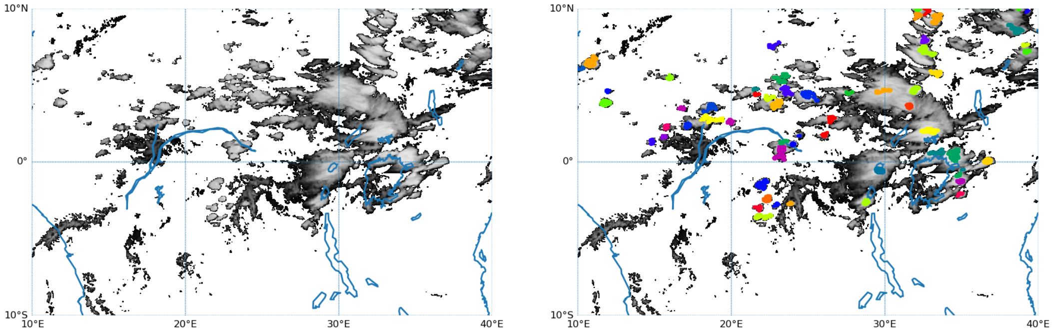

(c) 260 K threshold (d) Markers: stage 3 Cb-TRAM cores

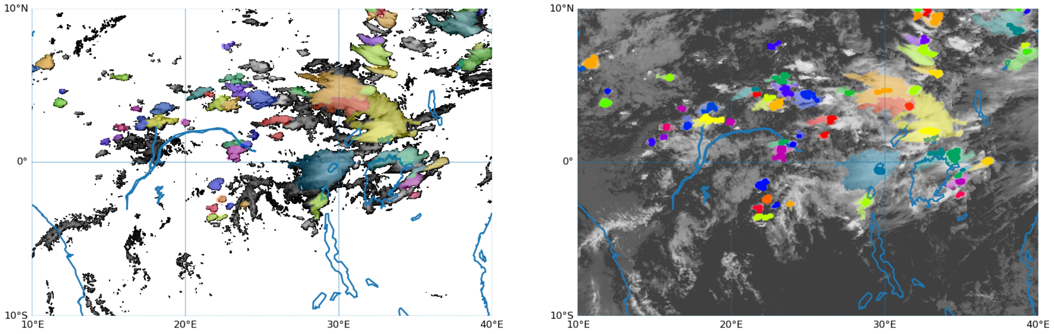

(e) Anvils (f) Cores and associated anvils

Figure 4.1: Illustration of the watershedding process at 14:15 UTC on 15-06-2007. a) 10.8 μm brightness temperature field from SEVIRI. b) pixels not classified as cloud by the SEVIRI CLASS-2 product are removed. c) pixels with a 10.8 μm brightness temperature > 260 K are removed. d) the location of the watershed markers (all stage 3 Cb-TRAM cloud cores detected at this timestep). e) the location of the anvil objects produced by the watershedding process. f) the location of stage 3 Cb-TRAM cores and their associated anvil objects.

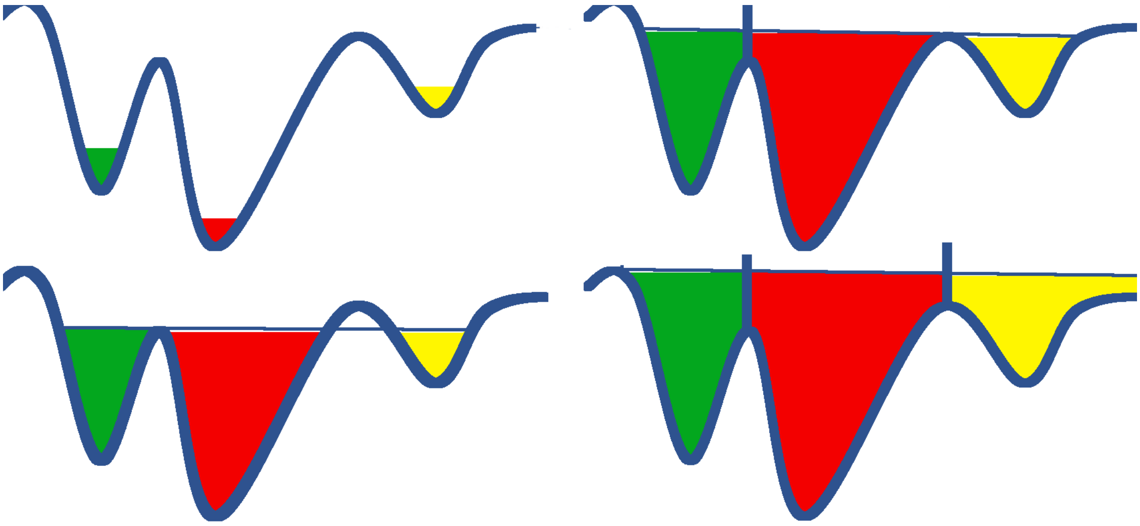

Figure 4.2: Illustration of the segmentation process. Brightness temperatures (curved blue line) are interpreted as a topographic field. Where basins in this field coincide with tracked cores from Cb-TRAM, a different colour of water is added to each basin. The water is then allowed to rise up, following the contours of the topographic field. The image is segmented at the points where two basins of water meet.

pixels associated with the core are assigned an identifying number. These numbers can be considered to correspond to different colours of water. Each basin containing a core is initialised with coloured water (Fig. 4.2). Any minima which are not collocated with a core are ignored.

The water in these basins is then allowed to rise, following the topography of the brightness temperature field (Fig. 4.2). As the water rises, basins with different coloured water will begin to merge. The image is then segmented where the basins of coloured water merge.

This allows the brightness temperature field in Fig. 4.1c to be divided up among the cores, with divisions following the gradient of the rate of change of brightness temperatures (Fig. 4.1e). Any area of cold cloud which is not connected to a Cb-TRAM core is discarded. These pixels are likely to be cirrus cloud, or regions of anvil outflow which have detached from a previously existing region of convective updraft and are not tracked in this study.

The watershedding process therefore identifies regions of cold cloud associated with each of the stage three cores tracked by Cb-TRAM. These regions will be referred to in this section as ‘anvils’.

Cb-TRAM was used in combination with the watershedding technique described above to track convective ‘cores’ and ‘anvils’ across sub-Saharan Africa for the months of March, June, September and December 2007. The year 2007 was chosen in order to allow a comparison with the results presented in Section 3. The individual months were chosen in order to both generate a dataset large enough to allow the study of convective cloud properties across different seasons and to minimise the amount of missing data in the SEVIRI’s 10.8 μm brightness temperature dataset.

4.3 Results

4.3.1 Overview of tracked cloud dataset

During the months of March, June, September and December 2007, Cb-TRAM tracked 2,016,325 convective cloud cores over sub-Saharan Africa. This study will focus on convection over land and so only the 1,176,116 cores which pass over land at some point during their lifetime are included in this study. 213,794 of these cores were assigned an anvil by the watershedding process described above. Figure 4.3 shows the number of cores and anvils tracked in each month. Note that the number of anvils is equal to the number of cores which, at some point during their lifetime, are designated as stage three cores by the Cb-TRAM tracking algorithm. Those cores that do not reach this development stage are not assigned an anvil by the watershedding process, as described above.

The location of all tracked cores in each month is shown in Fig. 4.4. These maps show a similar pattern to that seen in Fig. 3.1, giving an overview of the seasonal changes in convective activity, driven largely by changes in the location of the ITCZ

(Yang and Slingo 2001; Schröder et al. 2009).

While the trail of cores stretching north from Madagascar in June and September (Fig. 4.4) corresponds with the prevailing winds in the region (Fig. 2.5), the straight-edged band of cores seen in December and to a lesser extent in March (Fig. 4.4) is likely a retrieval artefact. This feature, composed of a relatively small number of cores, may be the result of an issue with the Cb-TRAM tracking algorithm, or the use of a relatively coarse grid to mask out those cores which do not pass over land at some point in their lifetime. These cores are a small fraction of the dataset presented here, but it should be noted that the spatial distribution of cores in this region in March and December may be subject to retrieval artefacts.

It should be noted that this map shows the number of individual convective cloud cores resolved by the Cb-TRAM tracker. Areas with fewer convective cloud cores may therefore experience very intense convective events, due to the presence of a few, very large convective clouds, while those with many convective cores may experience

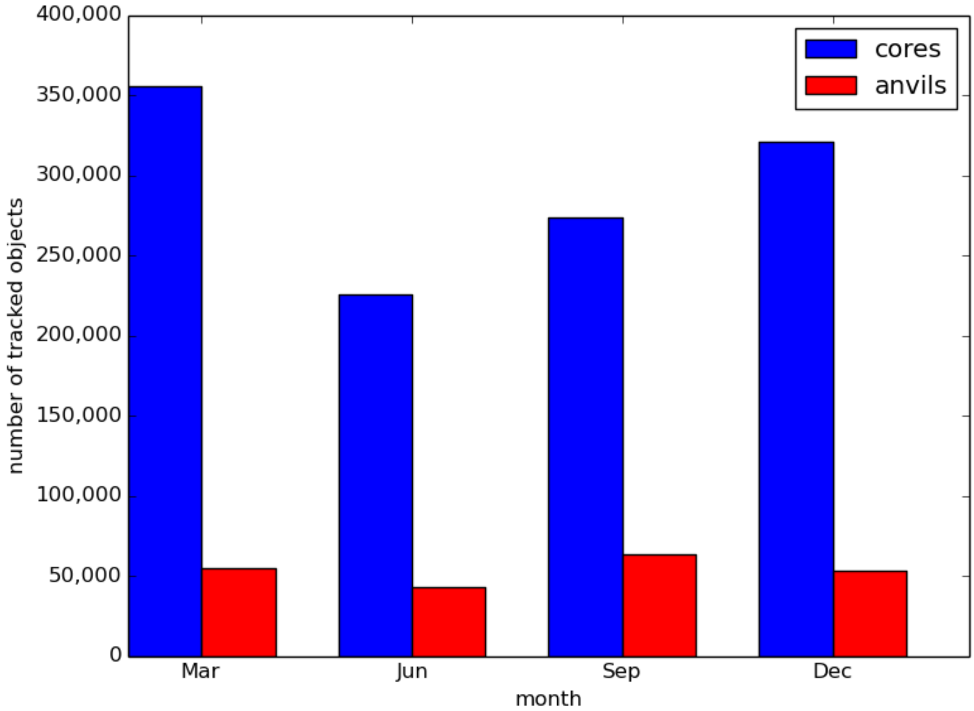

Figure 4.3: The total number of cores tracked by Cb-TRAM and the total number of anvils produced by the watershedding process, for individual months in 2007.

a large number of smaller, more isolated convective events. Alternatively, areas with many convective cloud cores may indicate the presence of large convective cloud systems with many embedded convective cores.

Figure 4.5 shows the distribution of times for which Cb-TRAM was able to track cloud cores. It can be seen that the majority of cores were detected, and therefore tracked, for periods of less than an hour, with the number of tracked cores falling off rapidly with increasing lifetimes. As clouds with longer lifetimes are likely to display different features to the majority of short-lived clouds, and as longer lived clouds can be expected to contribute significantly to observed mean cloud properties across

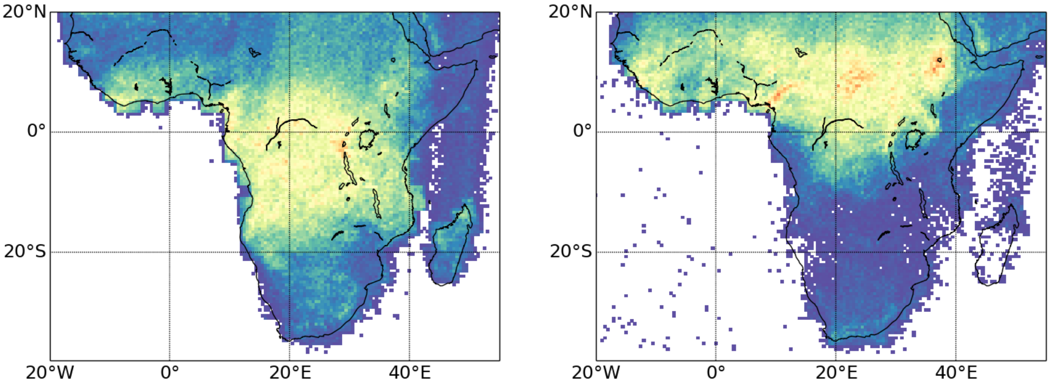

(a) March (b) June

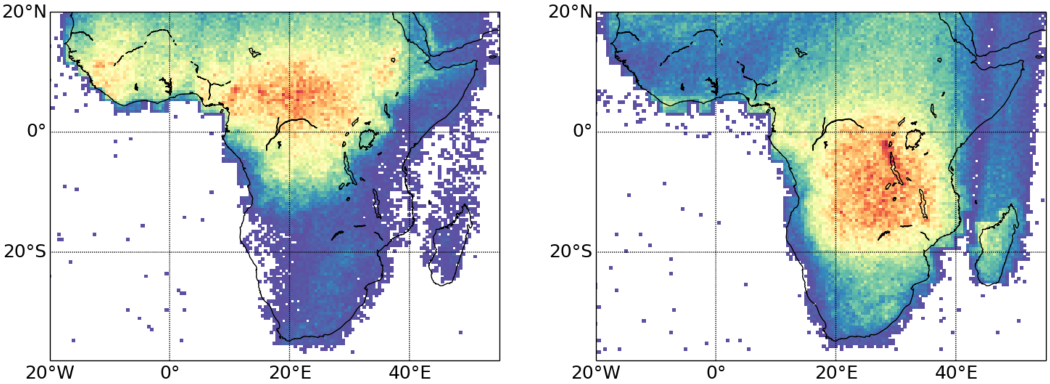

(c) September (d) December

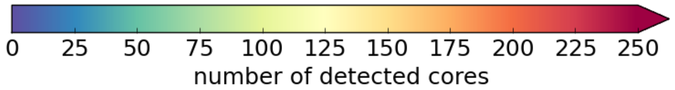

Figure 4.4: Maps showing the location of all convective cores detected by Cb-TRAM during individual months of 2007. Cores are included in this plot for each timestep at which they are detected.

sub-Saharan Africa, the following analysis will be broken down by cloud lifetime. It is however important to note that, as discussed in Section 2.2.4 cloud cores are considered to initiate when one core splits and to dissipate when multiple cores merge.

Where appropriate, results in this study will be divided by total cloud lifetime and by season. For clarity, table 4.1 shows the number of cores tracked in each month, as well as how many of these cores fall into each of the four lifetime categories used. As shown in Fig. 4.5, it can be seen that the majority of the cores were tracked for periods of time less than three hours.

In Section 4.3.2, the combined datasets of tracked convective cloud cores and anvils, will be used to quantify the horizontal and vertical development of convective cloud across sub-Saharan Africa.

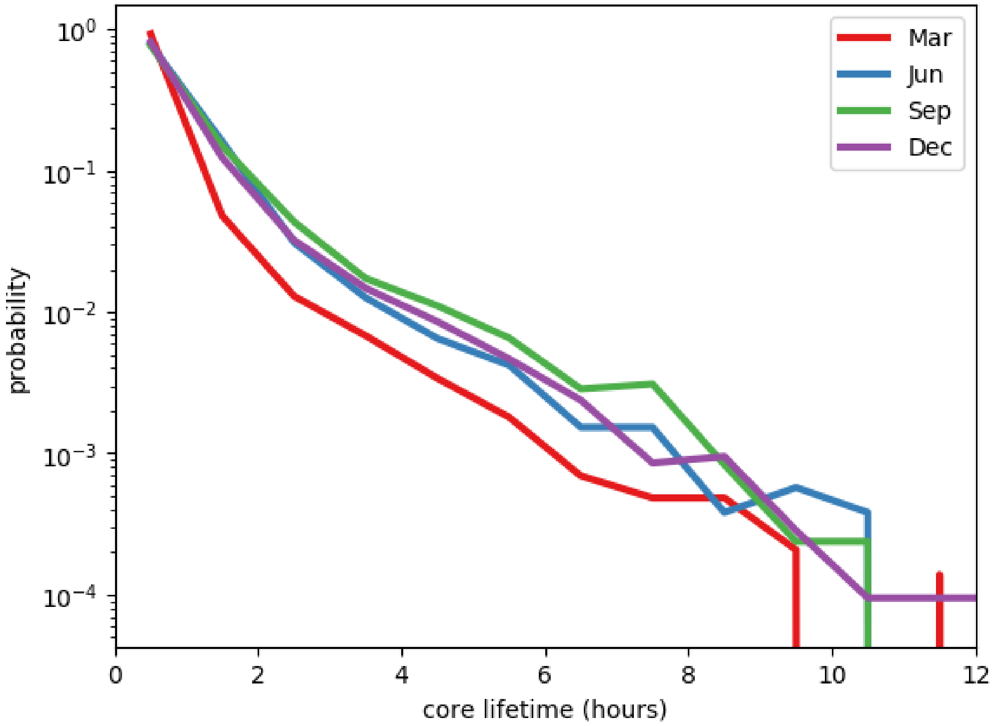

Figure 4.5: Distributions of the time for which each core in the Cb-TRAM dataset was tracked during individual months of 2007.

Core Lifetime	**March**	**June**	**September**	**December**
All	355,722	225,580	274,036	320,778
< 3 hours	350,005	219,560	265,111	313218
3-6 hours	4,702	4,909	7,201	6,492
6-9 hours	830	856	1,367	861
> 9 hours	185	255	357	207

Table 4.1: The total number of cores tracked by Cb-TRAM. Figures are given for individual months in 2007 and for each of the four core-lifetime categories referred to in this study.

4.3.2 Convective cloud morphology

This section aims to quantify the evolution of the morphology of convective cloud cores and anvils over the convective lifecycle. Plots in this section are shown for different total cloud lifetimes and for individual months where appropriate. Although these breakdowns are not shown in cases where there is little variability between clouds with different lifetimes, or during different seasons. As shown in Table 4.1, it is important to note that the vast majority of tracked cores persist for less than three hours.

Convective clouds which persist for longer periods of time have a larger horizontal core (Fig. 4.6a) and anvil (Fig. 4.6b) areas. This may be due to local environmental factors limiting the growth, and hence lifetime, of small convective systems, as well as due to the presence of larger organised convective systems, in which individual convective updrafts may not be resolved by SEVIRI and the Cb-TRAM algorithm. Due to the very large number of short-lived clouds in this dataset, smaller, shorter-lived clouds contribute significantly to the total area covered by convective cloud cores (Fig. 4.6a) and, to a lesser extent to the total anvil area (Fig. 4.6b).

Convective cloud cores which persist for between zero and three hours are also warmer than those that persist for more than three hours, with the distribution of observed minimum core CTT peaking at around 235 K (Fig. 4.7). Longer-lived cores have colder CTTs and are most commonly observed to have minimum CTT of around 210 K. Although these temperatures do not continue to fall with

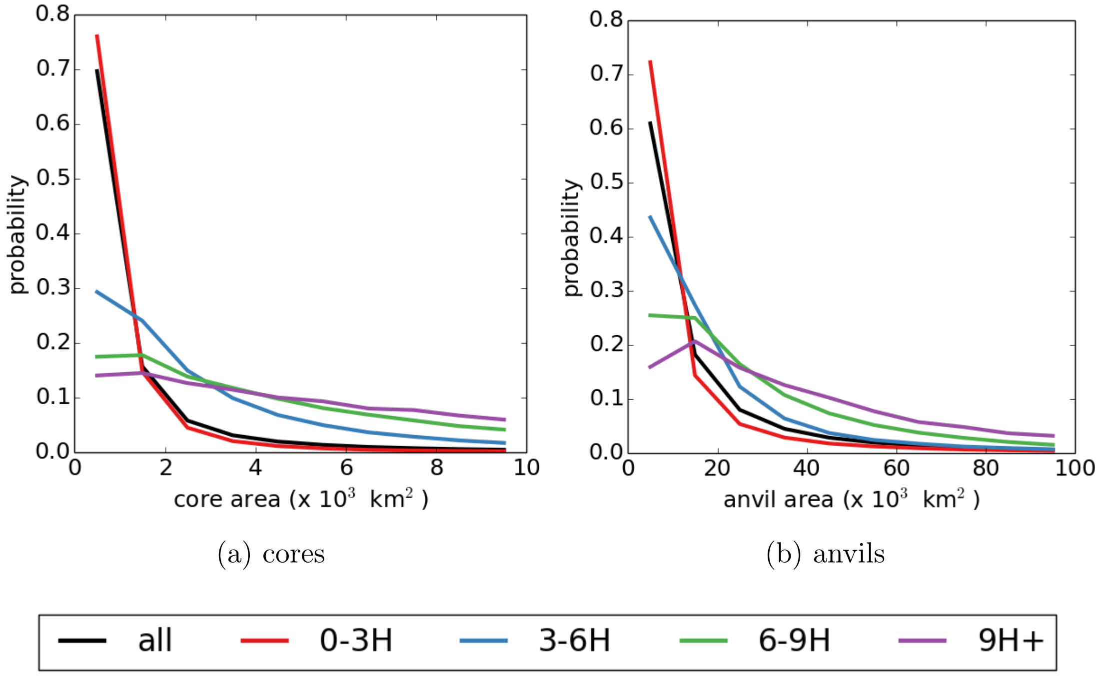

(a) cores

(b) anvils

Figure 4.6: Distribution of horizontal core and anvil areas over land in sub-Saharan Africa during the combined months of March, June, September and December 2007. Distributions are shown separately for all tracked clouds, as well as for clouds which live for different periods of time.

cloud lifetime, as developing cores quickly reach the tropopause and stop developing vertically.

There is very little seasonal variation in the overall distributions of detected minimum core CTTs, or horizontal core and anvil areas. Figs. 4.7 and 4.6 therefore show distributions for the combined months of March, June, September and December 2007.

Monthly mean maps of the spatial distribution of horizontal core and anvil areas show mean core areas as large as 500 km^2 (Fig. 4.8) and anvils as large as 100,000 km^2 (Fig. 4.9). Larger cores with a mean horizontal area of around 350 km^2 are also seen in central Africa during March, with the largest cores observed in the Sahel and West Africa in June and September and southern Africa in December (Fig. 4.8). Larger anvils are concentrated in central Africa in March, in the Sahel in June and over Madagascar in December (Fig. 4.9).

Due to the fact that individual anvil objects have been defined for each resolvable stage three cloud core, the anvil areas shown in Fig. 4.9 are smaller than the anvil areas reported in studies which define an anvil to be an area of cloud where the outgoing longwave radiation is below a certain threshold. In this study each anvil is associated, by definition, with a single convective core. Anvils defined using an outgoing longwave radiation threshold often have multiple embedded convective cores.

The spatial distribution of large convective cloud cores (Fig. 4.8) and anvils (Fig. 4.9) follows the broad seasonal patterns of the ITCZ and hence the large-scale movement of intense convection discussed in Section 3.3.1. This same seasonal pattern of convection is also seen in the monthly mean maps showing the spatial distribution of minimum core CTT (Fig. 4.10). The coldest cores, with mean minimum core CTTs of around 210 K, are concentrated in central Africa during March and December, while the warmest cores, with mean CTTs above 250 K are concentrated in West

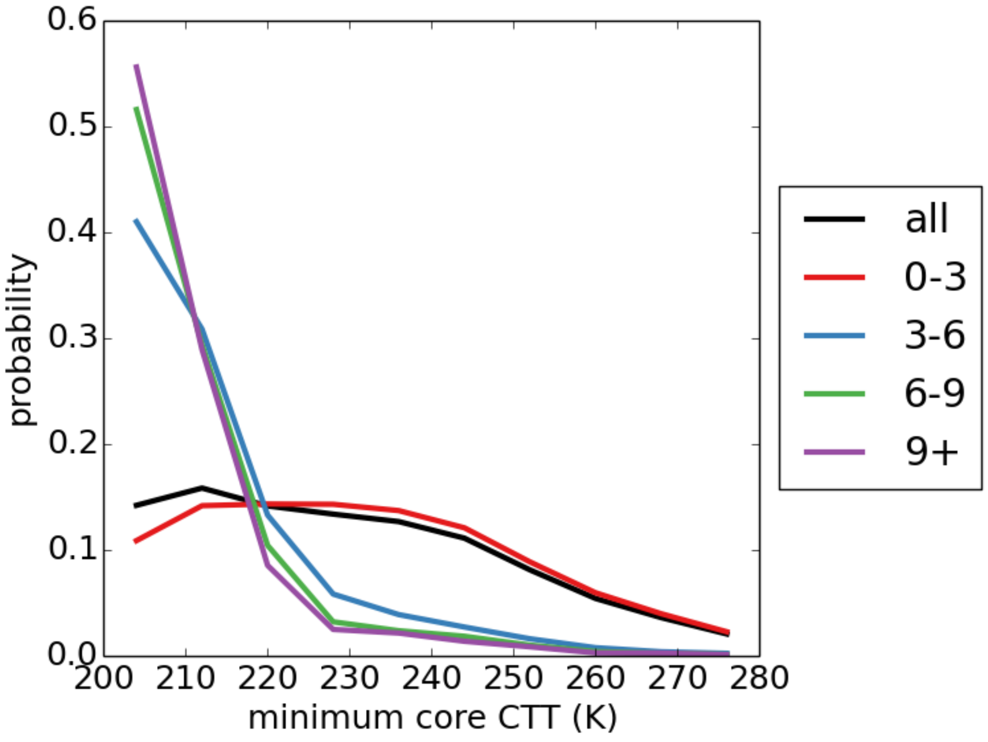

Figure 4.7: Distribution of minimum core cloud top temperatures over land in sub-Saharan Africa during the combined months of March, June, September and December 2007. Distributions are shown separately for all tracked cores, as well as for cores which live for different periods of time.

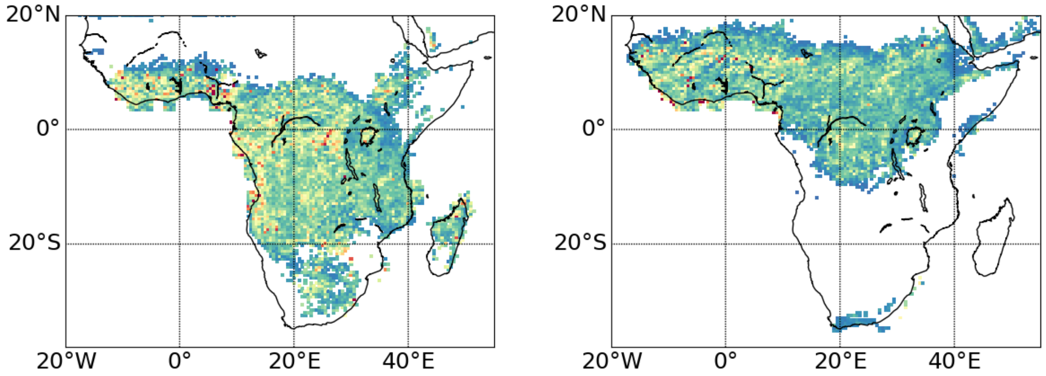

(a) March (b) June

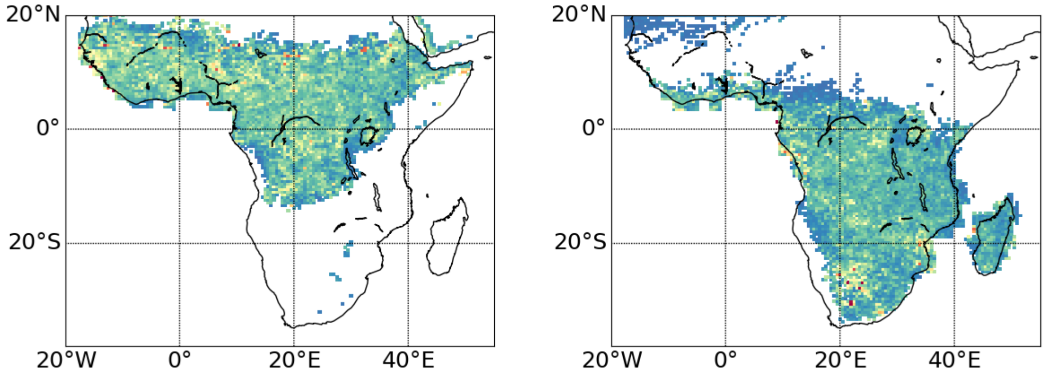

(c) September (d) December

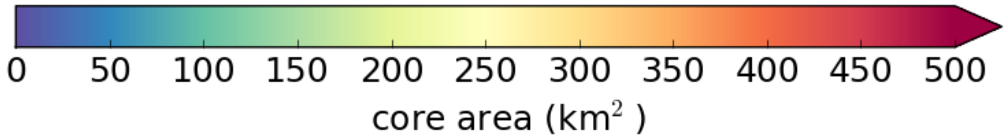

Figure 4.8: Seasonal and spatial distribution of mean core area (defined as the mean area of all cores whose centre of mass falls within a grid box) across sub-Saharan Africa during 2007. Values are shown for regions where at least 100 cores were detected during the month plotted.

Africa during March and in southern Africa in all seasons, but particularly during June (Fig. 4.10).

A clear diurnal cycle in the number of convective cloud cores detected by Cb-TRAM is observed (Fig. 4.11). There are two peaks in the number of detected cores, the first between 05:00 and 07:00 LST and the second between 15:00 and 18:00 LST. While the broad shape of the diurnal cycle is the same for short and long-lived convective clouds, it is notable that the earlier peak in the number of cloud cores

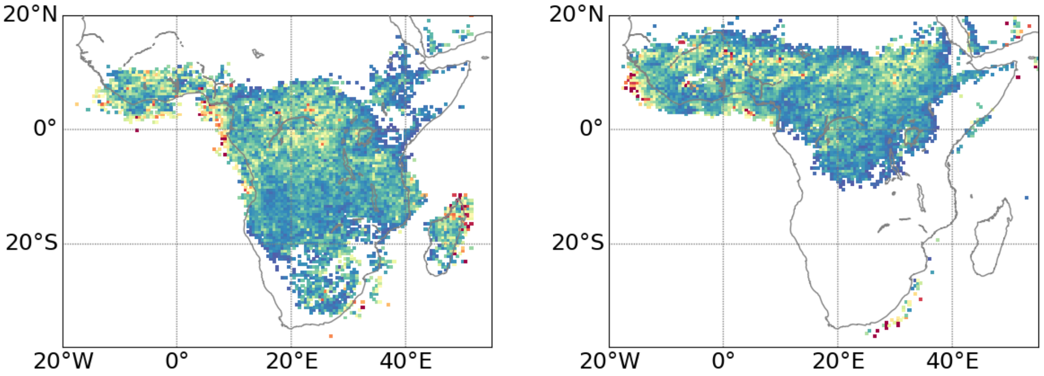

(a) March (b) June

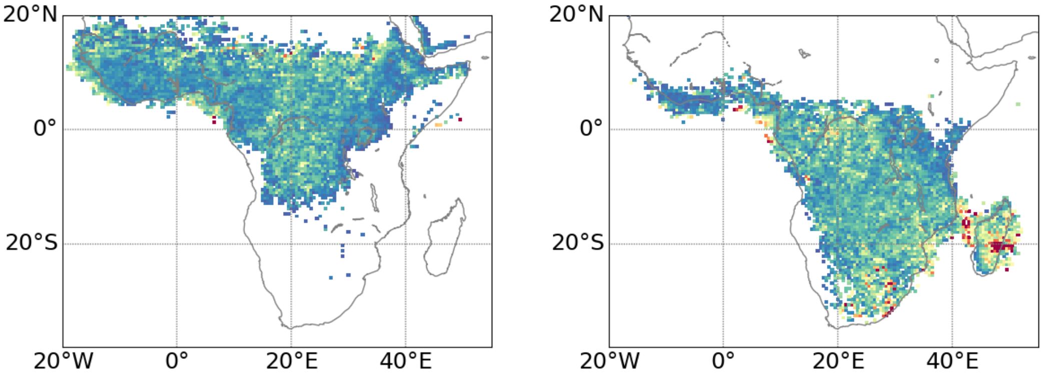

(c) September (d) December

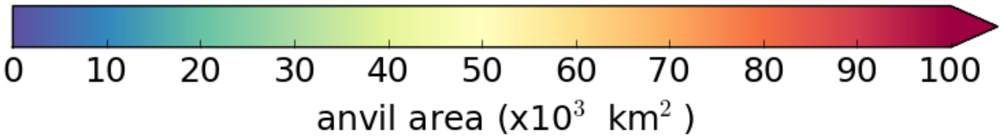

Figure 4.9: Seasonal and spatial distribution of mean anvil area (defined as the mean area of all anvils whose centre of mass falls within a grid box) across sub-Saharan Africa during 2007. Values are shown for regions where at least 10 anvils were detected during the month plotted.

becomes less distinct as total cloud lifetime increases. In addition, the timing of the peaks shifts to later in the day for longer-lived convective clouds (Fig. 4.11). The magnitude of the diurnal cycle is also greater for longer lived clouds, indicating that shorter-lived clouds are more likely to be present at all times of day, while the presence of long-lived clouds is more strongly correlated with diurnal variability in solar insolation.

Monthly mean diurnal cycles of horizontal core and anvil areas show distinct seasonal changes (Fig. 4.12), with the strongest magnitude seen in March and the weakest in December. The diurnal cycle in core area shows a clear bimodal distribution for longer-lived cores, although there is little diurnal cycle in core area for clouds living for less than three hours. This bimodal distribution peaks at around 05:00 LST and again at around 18:00 LST. Although the peaks are much stronger in March and weaker in December, likely due to the fact that many more individual convective cores are identified by Cb-TRAM in central Africa in December than in March (Fig. 4.4). The late afternoon peak likely corresponds to the growth of convective cloud

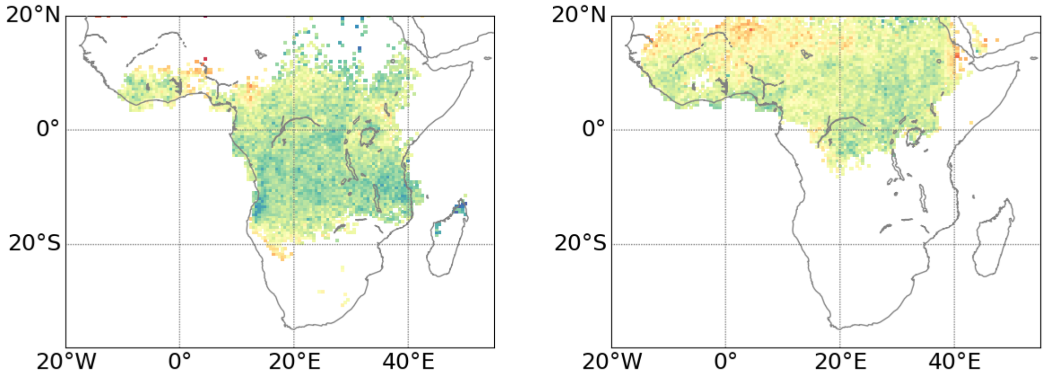

(a) March

(b) June

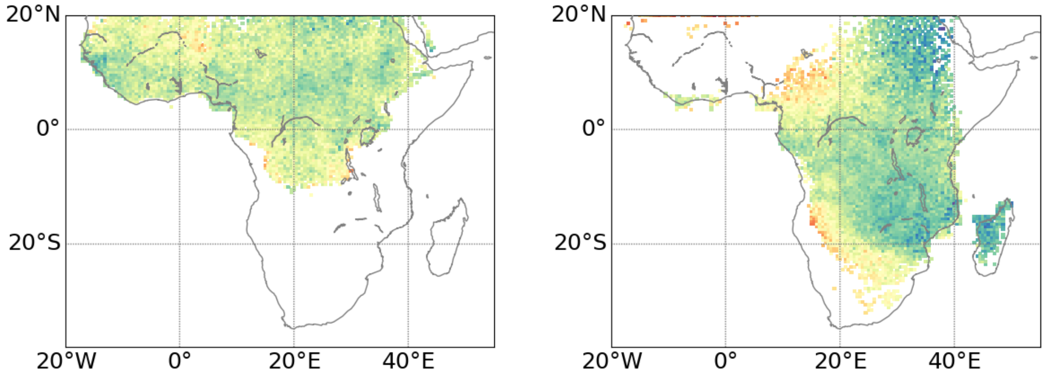

(c) September

(d) December

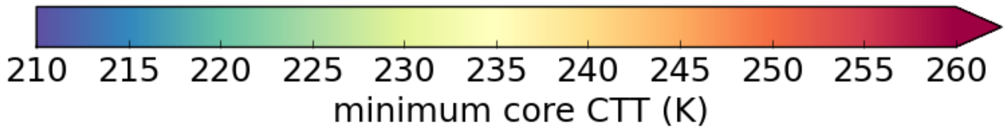

Figure 4.10: Seasonal and spatial distribution of minimum core CTT (defined as the mean minimum CTT of all cores whose centre of mass falls within a grid box) across sub-Saharan Africa during 2007. Values are shown for regions where at least 100 cores were detected during the month plotted.

initiated by strong solar insolation in the early afternoon, while the morning peak in core area may be caused by the destabilising effects of overnight radiative cooling of the atmosphere.

The diurnal cycle for convective cloud anvils shows that the horizontal area peaks overnight (Fig. 4.12). While there is a clear bimodal distribution in the diurnal cycle of core area, anvils seem to be initiated in the afternoon and persist throughout the day. There is less seasonal variation than for the area of the convective cloud cores, although there is a peak in longer-lived cloud anvils at around 10:00 LST in all months. This peak is particularly sharp in March.

Both core and anvil areas show a strong increase in both the average object area and in the magnitude of the diurnal cycle for longer-lived clouds.

The clear fall in cloud core area around noon (Fig. 4.12) is not reflected in the diurnal

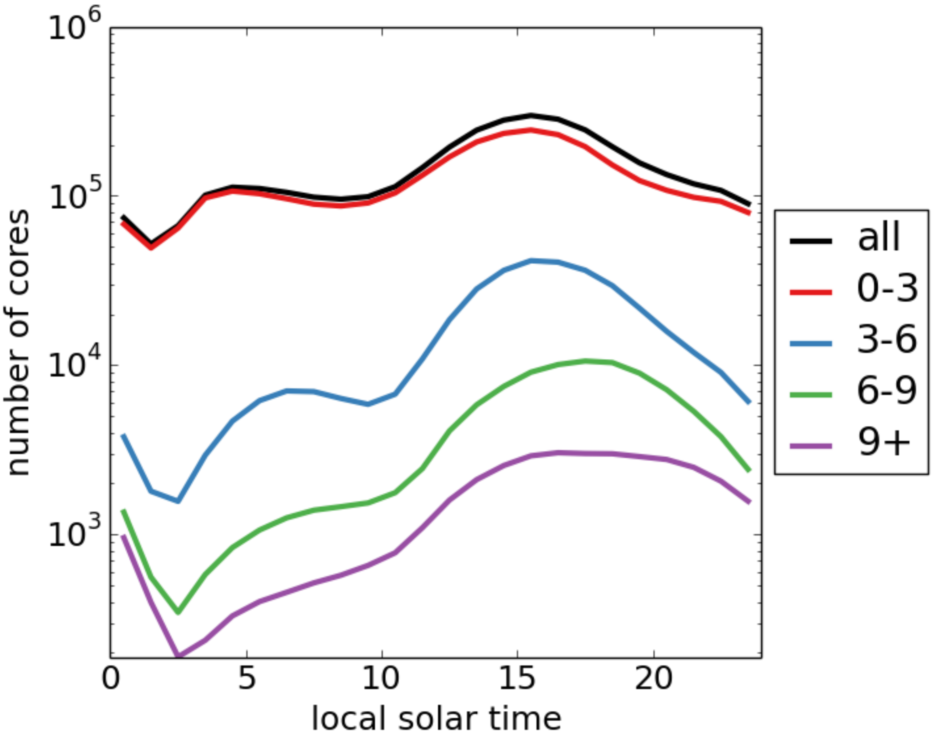

Figure 4.11: Diurnal cycle of the number of convective cloud cores detected by Cb-TRAM over land in sub-Saharan Africa during the combined months of March, June, September and December 2007. The diurnal cycle is shown separately for all tracked cores, as well as for cores which live for different periods of time.

cycle of the number of cloud cores (Fig. 4.11), as Fig. 4.12 shows the average core area per cloud core, rather than total core area over sub-Saharan Africa.

While Figure 4.12 shows the diurnal cycle in the area of individual anvil objects, it is also interesting to look at the diurnal cycle of the total anvil coverage, as it is the total amount of anvil cloud which will largely determine the radiative impact of convective cloud. While individual, long-lived clouds have been shown to have a larger anvil area, Fig. 4.13 shows that the majority of the anvil coverage comes from shorter-lived convective cloud objects. For all months, there are clear minima in the total anvil area at around 11:00 LST and clear maxima at around 18:00 LST,

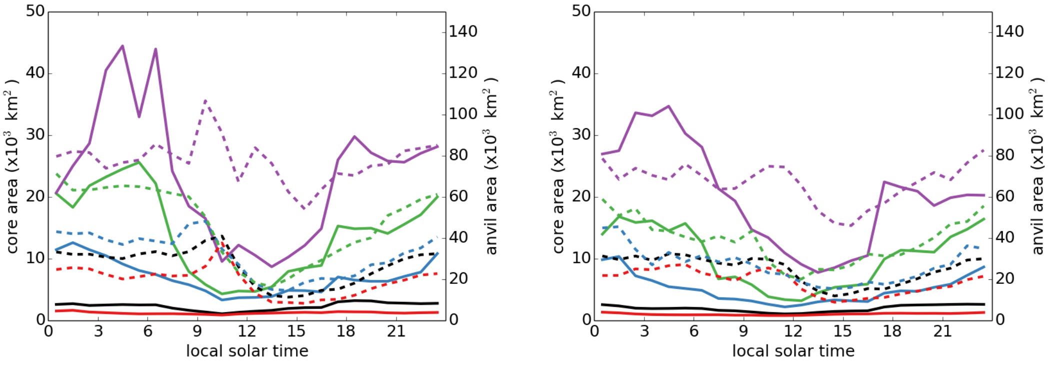

(a) March

(b) June

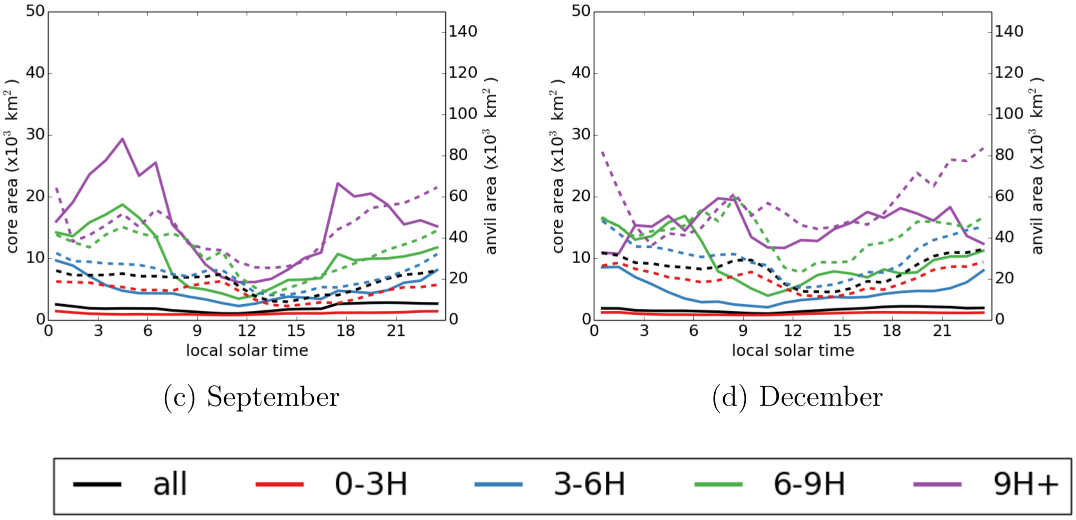

(c) September

(d) December

Figure 4.12: Diurnal cycle of the mean convective cloud core area per core (solid lines) and mean anvil cloud area per anvil (dashed lines) over land in sub-Saharan Africa during 2007. Diurnal cycles are shown separately for all tracked cores and anvils, as well as for cores and anvils which live for different periods of time.

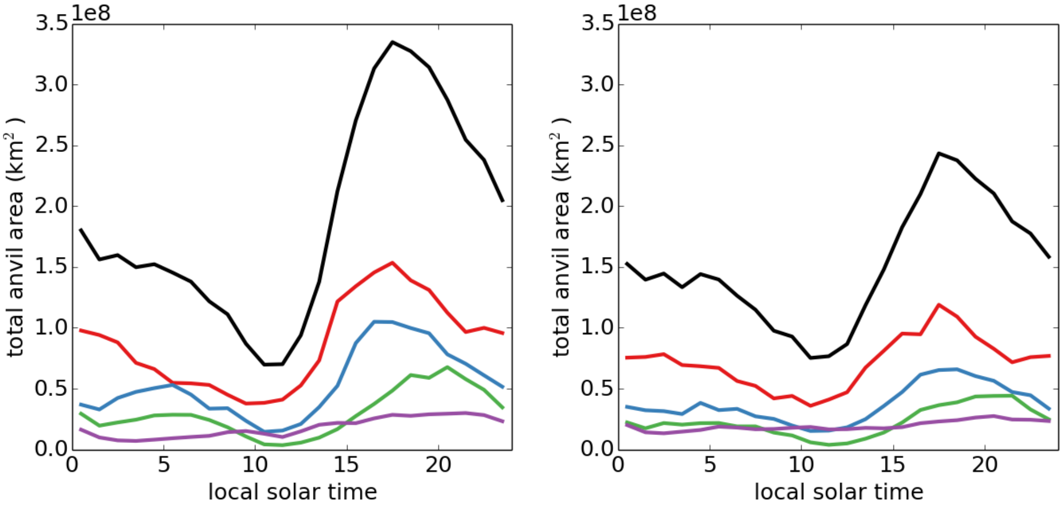

(a) March (b) June

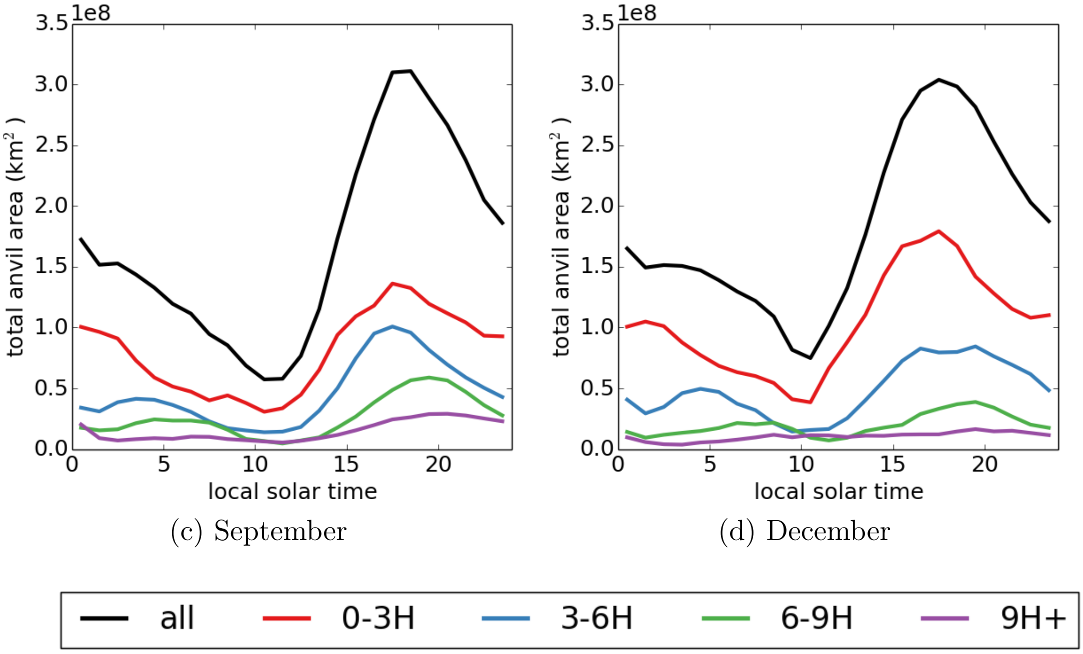

Figure 4.13: Monthly mean diurnal cycles of the total anvil area over land in sub-Saharan Africa during 2007. Diurnal cycles are shown separately for all tracked cores, as well as for cores which live for different periods of time.

although the time of maximum coverage occurs later in the day for longer-lived anvils, with the latest peak occurring at around 20:00 LST (Fig. 4.13).

The diurnal cycle of minimum convective core CTT shows the warmest CTTs occurring between 10:00 LST for shorter-lived clouds and 11:00 LST for longer-lived clouds (Fig. 4.14). The coldest CTTs are observed between 16:00 LST for the longest-lived clouds and 19:00 LST for the shortest-lived clouds. These observations

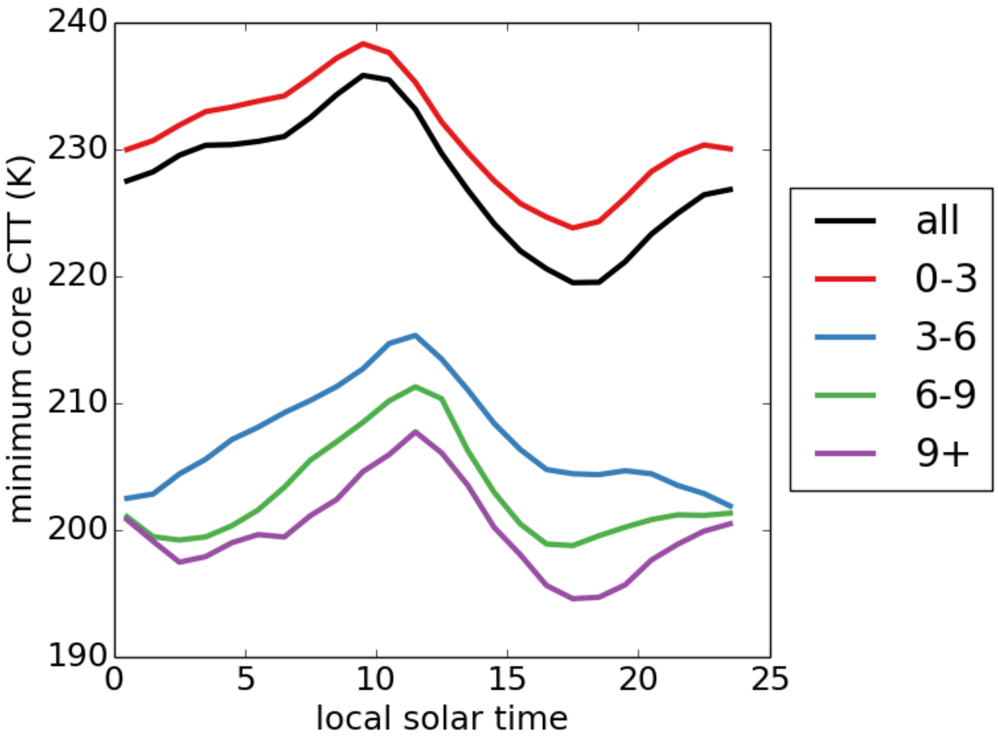

Figure 4.14: Mean diurnal cycle of the minimum convective core CTT over land in sub-Saharan Africa during the combined months of March, June, September and December 2007. Diurnal cycles are shown separately for all tracked cores, as well as for cores which live for different periods of time.

are in agreement with the timing of the seasonal mean phase of the diurnal cycle in CTT shown in Fig. 3.12.

There is a morning peak in the number of cores, at around 06:00 LST (Fig. 4.11), and a minimum in the CTT of convective cloud over central Africa from the CLAAS-2 product, at around 09:00 LST (Fig. 3.14). However, there is no clear morning minimum in the CTT for the majority of cloud cores across sub-Saharan Africa in Fig. 4.14.

There is however, a clear afternoon peak in all three figures. Cloud number peaks at around 15:00 LST (Fig. 4.11), with the minimum tracked core CTT appearing at 18:00 LST (Fig. 4.14) and the minimum in CLAAS-2 CTT over central Africa observed at 20:00 LST (Fig. 3.14).

One of the advantages of the Cb-TRAM tracking algorithm is that it allows monthly mean lifecycles of convective cloud cores and anvils to be observed. Core areas grow throughout the first half of the convective cloud lifecycle, before shrinking again (Fig. 4.15), while anvil areas generally grow throughout the lifetime of the convective cloud (Fig. 4.16. Convective cloud core areas appear to grow at a faster rate for longer-lived clouds (Fig. 4.15), although the same is not true of anvil areas, which appear to grow at a similar rate regardless of total cloud lifetime (Fig. 4.15).

One possible explanation for the shrinking in core area in the second half of the cloud lifecycle is the consumption of convective available potential energy in the immediate environment of the cloud, cutting off the supply of energy to further convective updrafts.

Figures 4.15 and 4.16 imply that longer-lived cores have larger horizontal core and anvil areas at their point of initiation. Although for both cores and anvils, while initial mean core area increases, the standard deviation is also large for longer lived convective clouds. As discussed in Section 2.2.4, this may in fact be due to the fact that new convective cloud objects splitting off from existing structures are considered to be newly initiated cloud objects at that point in time.

Following the lifecycle of observed convective core areas, the lifecycle of minimum core CTTs shows a cooling trend for approximately the first half of the cloud lifetime, followed by warming (Fig. 4.17). While the rate of change of CTT does not differ significantly between short and long-lived cores, longer-lived cores have colder minimum CTTs throughout their lifecycle, with cores that live less than three hours showing a mean CTT of around 230 K at the beginning of their lifetime, decreasing to around 215 K after three hours, and cores that live longer than three hours showing an initial CTT of around 210 K and decreasing to between 205 K for cores that persist for up to 6 hours and 195 K for cores that persist for more than 9 hours (Fig. 4.17). Although it should be remembered that, as shown in Table 4.1, only a small number of cloud cores persist for more than 9 hours.

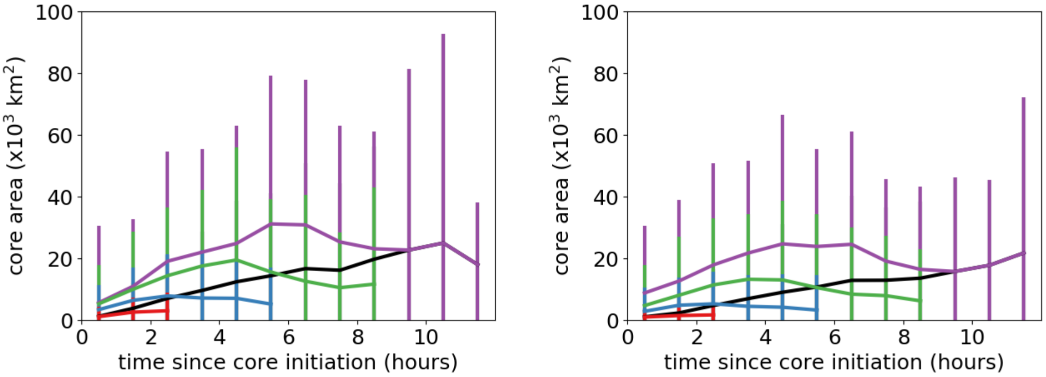

(a) March

(b) June

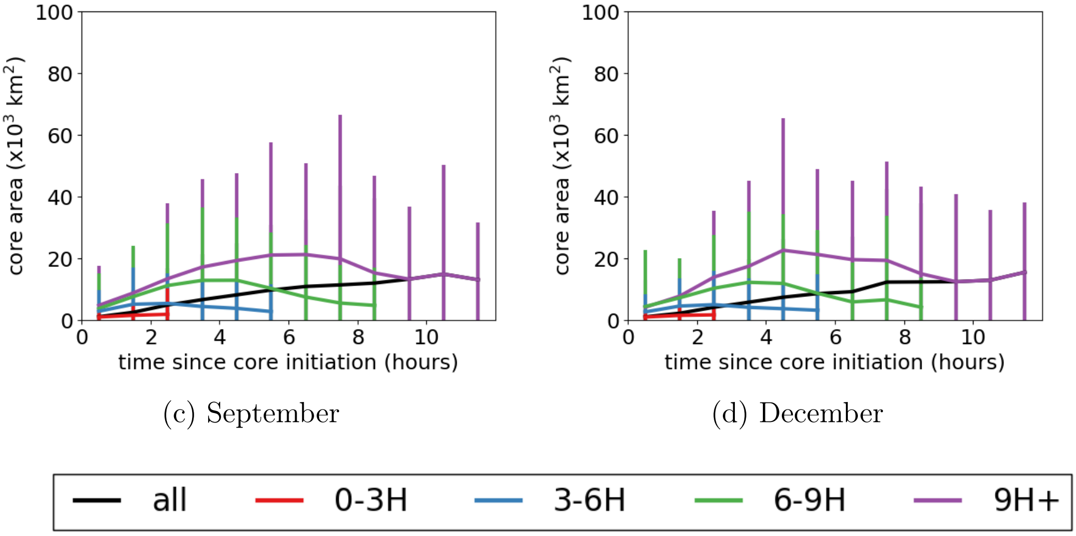

(c) September

(d) December

Figure 4.15: Monthly mean lifecycles of convective cloud core areas and associated standard deviations. Lifecycles are calculated over land in sub-Saharan Africa during 2007 and are shown separately for all tracked cores, as well as for cores which live for different periods of time.

As discussed in Section 2.2.4, this may in fact be due to the fact that new convective cloud objects splitting off from existing structures are considered to be newly initiated cloud objects at that point in time. These newly initiated objects would be expected to have a colder initial CTT than a new convective cloud core initiated independently.

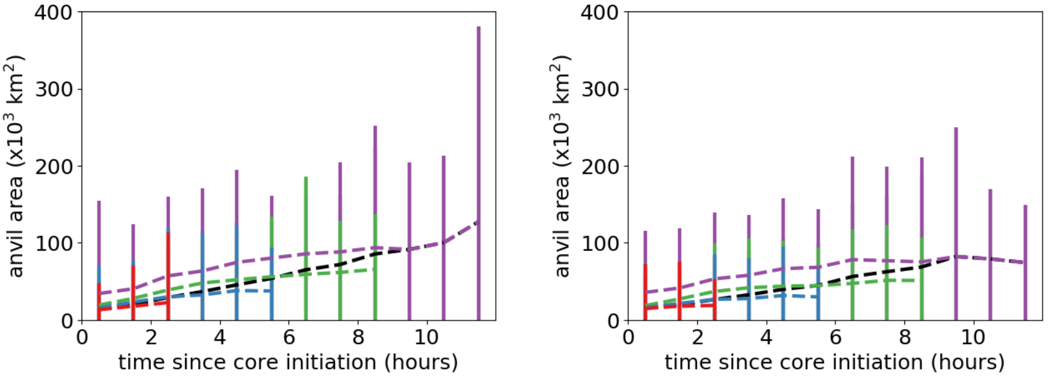

(a) March

(b) June

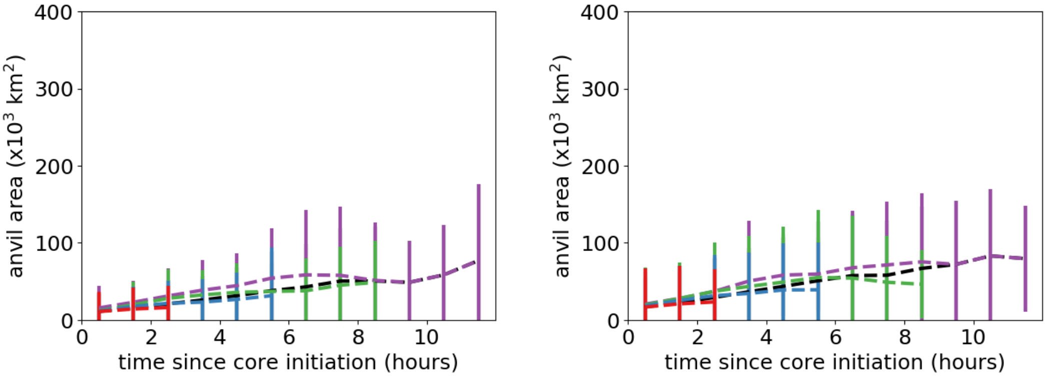

(c) September

(d) December

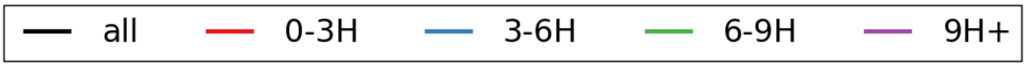

Figure 4.16: Monthly mean lifecycles of convective cloud anvil areas and associated standard deviations. Lifecycles are calculated over land in sub-Saharan Africa during 2007 and are shown separately for all tracked anvils, as well as for anvils which live for different periods of time.

4.3.3 Convective cloud lifetimes

This section will quantify the lifetime of convective cloud cores tracked by the Cb-TRAM algorithm. Plots in this section are divided by both total cloud lifetime and by month where appropriate. Although these breakdowns are not shown in cases where there is little lifetime, or seasonal-based variability in the variable shown. When considering differences in plots divided by cloud lifetime, it is important to note that, as shown in Table 4.1, the vast majority of tracked cores persist for less than three hours.

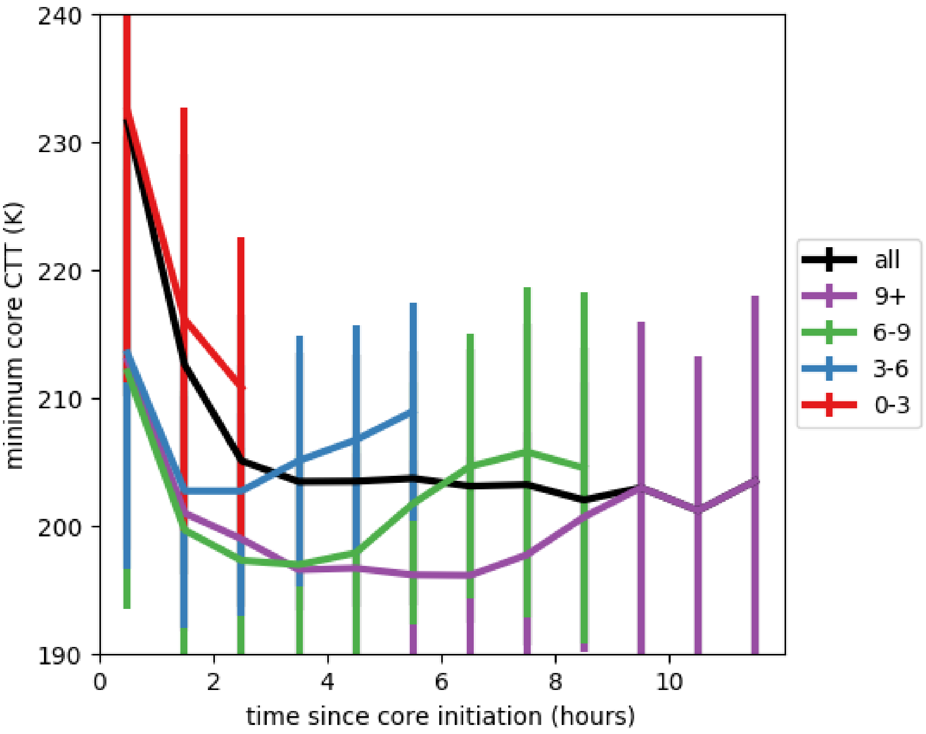

Figure 4.17: Mean lifecycle of minimum core CTT and associated standard deviations. Lifecycles are calculated over land in sub-Saharan Africa during the combined months of March, June, September and December 2007 and are shown separately for all tracked cores, as well as for cores which live for different periods of time.

The diurnal cycle of convective cloud initiation shows a bimodal peak in initiation times with peaks at around 18:00 LST and a smaller, early morning peak in initiation, which occurs earlier at around 04:00 LST for cloud which lives for three hours or less, and later, at between 06:00 and 09:00 LST for longer-lived cloud (Fig. 4.18).

The afternoon peak in initiation times is sharpest for clouds tracked in March and September, with the broadest distribution of initiation times observed in December (Fig. 4.18).

As the majority of clouds are very short lived (Fig. 4.5), the distribution of dissipation times looks very similar to the distribution of initiation times. For clouds which live for more than three hours, the peak times of dissipation occur at around 08:00 and 20:00 LST for clouds that live three to six hours, at around 11:00 and 02:00 LST for clouds that live six to nine hours and at around 16:00 and 02:00 LST for clouds that live more than nine hours (fig. 4.18).

The diurnal cycle of convective cloud initiation (Fig. 4.18) also looks similar to the diurnal cycle in the number of tracked cloud cores (Fig. 4.11). Both show a bimodal distribution with peaks in the early morning, at around 06:00 LST for the number of cores detected by the tracking algorithm and between 05:00 and 09:00 LST for the number of cores initiated at each timestep. The larger peak is in the afternoon, at between 15:00 and 17:00 LST for both the number of cores detected (Fig. 4.11) and the number of cores initiated (Fig. 4.18) at each timestep. However, Fig. 4.18 has sharper peaks than Fig. 4.11, indicating the persistence of cores after their initiation.

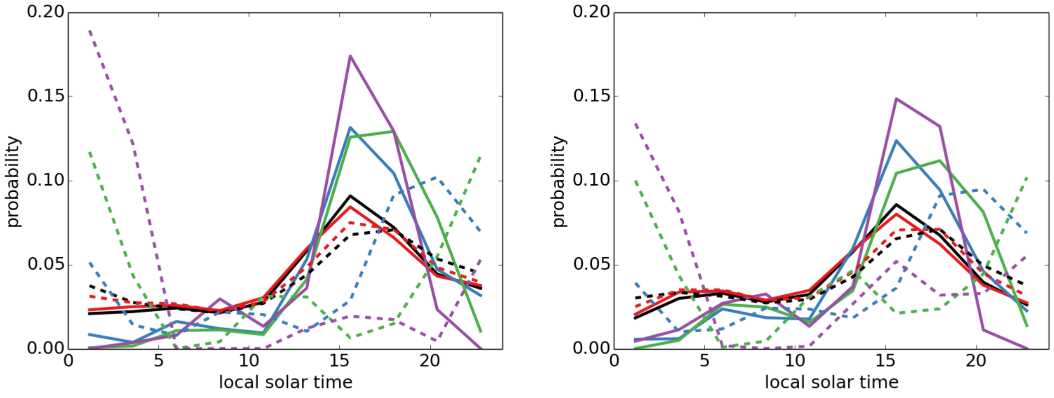

(a) March (b) June

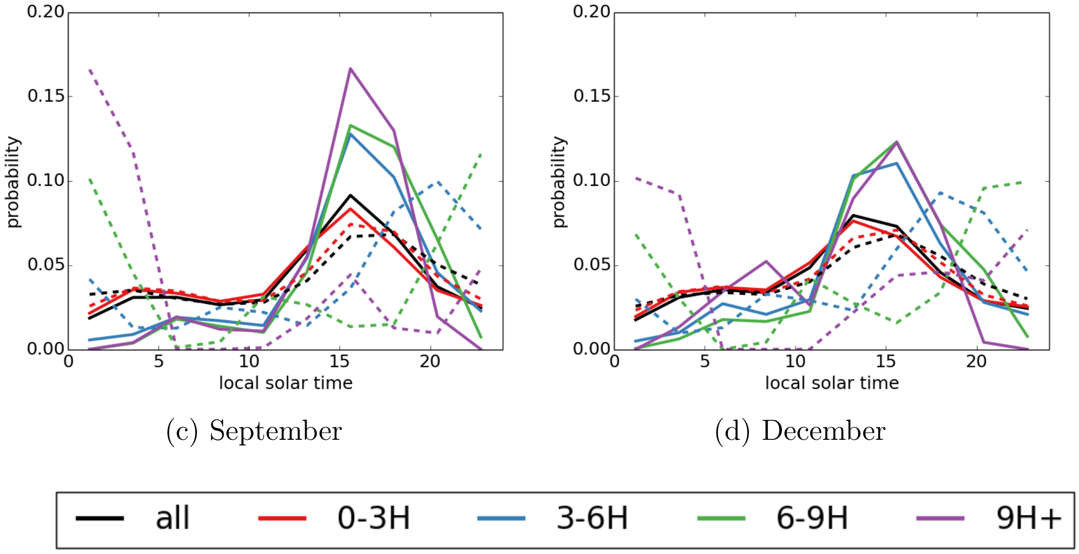

(c) September (d) December

Figure 4.18: Distribution of initiation (solid lines) and dissipation (dashed lines) times for convective clouds in sub-Saharan Africa during 2007. Distributions are shown separately for all tracked cores, as well as for cores which live for different periods of time.

Seasonal mean maps of the mean time of convective cloud initiation, and hence mean time of dissipation (Fig. 4.5), show that the most common time for the initiation of convective cloud is between 12:00 and 14:00 LST (Fig. 4.19). This is particularly true in March. However, the mean time of initiation occurs earlier, at around 10:00 LST in the region of West Africa. This is true in all months, but particularly in December (Fig 4.19). In all seasons there are regions of later convective initiation in southern and north-eastern Africa, as well as over parts of Madagascar (Fig 4.19). In all seasons, convection initiates at around 10:00 LST over Lake Victoria (Fig 4.19).

As discussed in Section 2.2.4 it should be remembered that the definitions of initiation and dissipation of convection in this dataset include the merging and splitting of convective cloud cores.

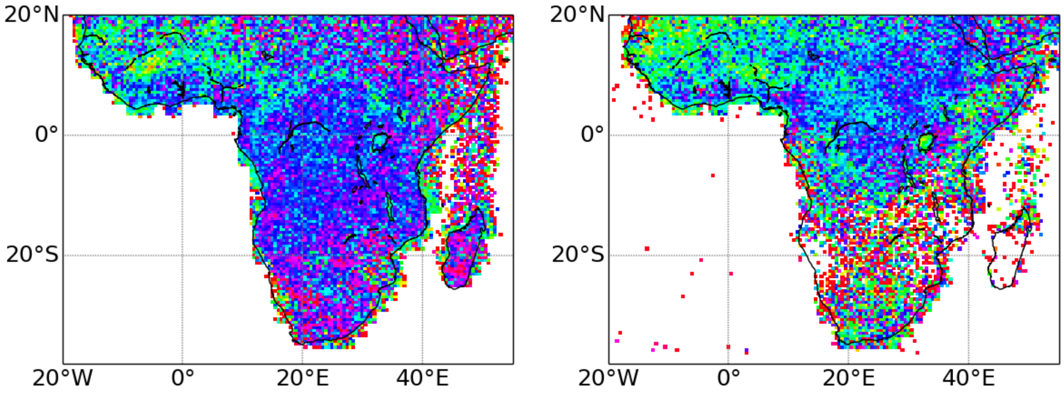

(a) March (b) June

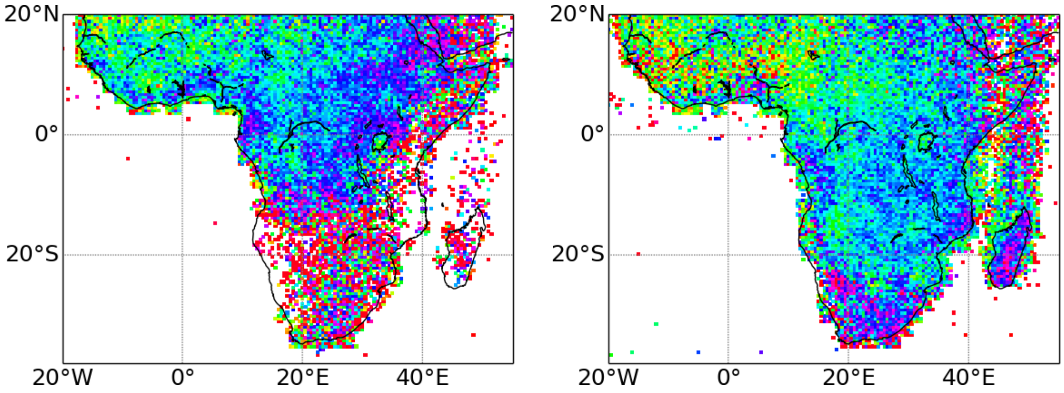

(c) September (d) December

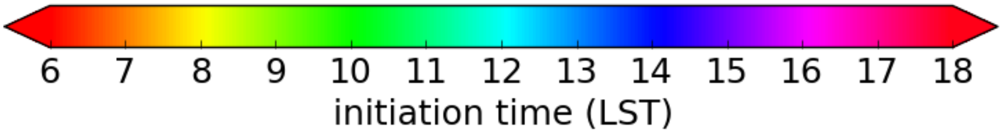

Figure 4.19: Seasonal maps of the mean time of initiation of convective cloud objects tracked by Cb-TRAM over land in sub-Saharan Africa during 2007.

4.4 Conclusions

This chapter examined the lifecycle of convective clouds in a Lagrangian framework, by individually tracking convective cloud cores and anvils. While the majority of previous studies are based on static datasets, or limited to a small area, or period of time, new convection-tracking tools, using the high time-resolution data available from SEVIRI make it possible to study the lifecycle of individual convective cloud objects.

Clouds were tracked across continental sub-Saharan Africa at 15 minute intervals, during the months of March, June, September and December 2007. The cloud tracking algorithm Cb-TRAM was used to detect and track convective cloud 'cores', where cores are defined as regions of contiguous convective updraft (Sect. 4.2). A watershedding algorithm was used in combination with information from the Cb-TRAM cloud tracker, a cloud mask from the CLAAS-2 cloud product and a brightness temperature threshold to detect 'anvils'. Anvils are therefore defined as regions of cloud colder than 260 K and associated with one of the stage three cores tracked by Cb-TRAM (Sect. 4.2).

The resulting dataset contains over one million tracked cloud cores and over 200,000 anvils. The distributions, diurnal cycles, lifecycles and spatial and seasonal cycles of a number of properties, including the number of detected convective cloud objects, horizontal core and anvil area, cloud top temperature, time of convective cloud initiation and dissipation and the time over which clouds were tracked, were quantified for this dataset.

The majority of clouds were tracked for periods of less than an hour, likely corresponding to single celled convective clouds (Galvin 2015), with a small fraction persisting for several days, likely corresponding to MCSs (Houze 2004). As found in previous studies (Tadesse and Anagnostou 2010), very few clouds were tracked for periods longer than 9 hours. Although it should be noted that these lifetimes are reflective only of the time for which Cb-TRAM was able to detect and therefore track regions of convective updraft and that convective clouds, particularly regions of anvil, may persist beyond the point detected in this dataset. Due to the short time for which the majority of the convective clouds were tracked and the fact that longer lived clouds are expected to have different properties, the analysis presented in this chapter was shown for clouds living 0-3 hours, 3-6 hours, 6-9 hours and more than 9 hours.

Horizontal core and anvil areas were shown to increase with longer cloud lifetimes, while minimum core CTT was shown to decrease with cloud lifetime. Previous studies have shown that the rate of area expansion of convective clouds is a strong indication of the expected lifetime of a convective system (Tadesse and Anagnostou 2010).

The diurnal cycle in convective activity was shown to have both a morning and an evening peak. In the morning, there is a small peak in the number of convective cores initiated between 04:00 and 09:00 LST. The number of detected cores peaks at around 06:00 LST, while mean core area per core peaks at around 05:00 LST. In the afternoon, there is a sharp peak in the number of initiating cores around 18:00 LST, although the total number of detected cores peaks at around 15:00 LST with both the horizontal core area and minimum core CTT observed at around 18:00 LST.

While many previous studies have shown a late afternoon peak in convective activity (Yang and Slingo 2001; Liu and Zipser 2005; Zipser et al. 2006; Schröder et al. 2009) over land, and an early morning peak over ocean, these studies have not generally observed the early morning peak in convective activity quantified in this study. Although a study of tracked convective cloud objects during the Tropical Composition, Clouds and Climate Coupling Experiment observed a similar secondary maxima in overshooting cloud tops in coastal land regions (Bedka et al. 2010). The observed peak may be related nighttime radiative cooling, with cooling at the cloud top and warming at cloud base creating instability and hence invigorating convection. It could also be related to the invigoration of convection formed over coastal land regions, due to an early morning land-sea breeze effect (Desbois et al. 1988), or due to the presence of MCSs persisting throughout the night (Nesbitt and Zipser 2003).

In agreement with previous studies (Nesbitt and Zipser 2003; Schröder et al. 2009), mean anvil area per cloud object is shown to begin growing in the early afternoon, peaking overnight, while the total anvil coverage reaches a minimum at around 11:00 LST, peaking at around 18:00 LST.

It was shown that the seasonal and spatial patterns of the number of tracked cloud cores mirrors that of the mean CLAAS-2 CTT retrieval shown in Fig. 3.1 across sub-Saharan Africa. These patterns are likely due to the seasonal migration of the ITCZ and hence the intensity of convective activity (Waliser and Gautier 1993; Yang and Slingo 2001; Schröder et al. 2009).

In the Sahel region, the number of detected cloud cores is highest in June and September, while the largest core and anvil areas, as well as the coldest core CTTs are seen in March. Convective clouds are initiated earlier in the day, at around 10:00 LST to the west of this region, with initiation occurring later, at around 14:00 LST to the east. There is a strong seasonal change in mean time of convective initiation, with earlier initiation times becoming more common later in the year.

Previous studies (Liu and Zipser 2005; Zipser et al. 2006; Peng et al. 2014) have shown a high incidence of intense convection in equatorial Africa. In central Africa, the number of cores detected is highest in September and December, although there is a lot of convective activity observed during all four months. Core and anvil areas, as well as core CTTs peak in March. The mean time of initiation of convection occurs in the afternoon at around 15:00 LST in March, with the mean time of initiation becoming earlier throughout the year.

In all seasons, convection initiates in the morning over Lake Victoria. Previous studies have suggested that this is due to a land-lake breeze effect, causing warmer temperatures at the lake surface, with colder overlying air, leading to instability and convective activity (Desbois et al. 1988; Yin et al. 2000; Schröder et al. 2009).

Convective activity is much less intense in southern Africa throughout the year. The number of detected cores, as well as mean core and anvil area are highest in December, but there is relatively little deep convective activity during the rest of the year. CTTs are relatively warm throughout the year, particularly in the region of the Namib desert where the warmest CTTs are observed throughout the year. Convective initiation times occur later in the day, compared to the Sahel and central Africa. Mean initiation times occur between 15:00 and 17:00 LST in March, in the morning or late evening in June, around 17:00-18:00 LST in September and between 15:00 and 17:00 LST in December.

As discussed in Section 2.3.2, the variability of convective lifecycles, including such properties as time of convective initiation, cloud lifetime and speed of development are not well characterised on the global scale. While previous studies have quantified the lifecycle of convection using data from polar-orbiting satellites, or spatially and temporally limited cloud tracking datasets, this study has attempted to quantify the properties of tracked convective cloud cores and anvils throughout their lifetime, across a large area and period of time. These results provide valuable information about avenues for future development and validation of both convective cloud process models and convective parameterisations.

5 | Summary and Conclusions

Convective clouds are one of the core building blocks of tropical weather and climate. They play important roles in large-scale atmospheric circulations, the hydrological cycle, global energy budget and transport of heat, moisture, momentum, aerosols and trace gases throughout the troposphere (Grabowski and Petch 2009). Quantifying the temporal and spatial variability of convective cloud is therefore of fundamental importance in order to understand and accurately model global weather and climate systems.

A large number of observational studies have attempted to quantify the diurnal cycle (Janowiak et al. 1994; Yang and Slingo 2001; Nesbitt and Zipser 2003; Stratton and Stirling 2012) and lifecycle (Futyan and Del Genio 2007a; Pope et al. 2008; Bedka et al. 2010; Tadesse and Anagnostou 2010; Bennartz and Schroeder 2012) of convective cloud.

However, while the broad features of the diurnal cycle and lifecycles of convective cloud, such as the phase of the diurnal cycle over land and ocean, some aspects of convective interaction with local geography, and simple models of convective cloud lifecycles are well understood, the spatial and temporal variability of convective cloud properties are not well characterised on the global scale, particularly over large areas of Africa (Washington et al. 2013). Due to the complexity of the processes involved, general circulation and numerical weather prediction models also struggle to realistically simulate the spatial and temporal variability of cloud (Yang and

Slingo 2001; Guichard et al. 2004; Grabowski et al. 2006; Stratton and Stirling 2012). In particular, they fail to capture the diurnal cycle of convection (Yang and Slingo 2001; Guichard et al. 2004; Grabowski et al. 2006; Stratton and Stirling 2012), with convection developing too early and rapidly (Guichard et al. 2004; Stratton and Stirling 2012). On the other hand, CRMs which explicitly resolve convection and have grid scales of around 1 km or less have been shown to be capable of correctly simulating the diurnal cycle (Guichard et al. 2004; Grabowski et al. 2006; Sato et al. 2009).

Observations provide insights into these processes and allow us to investigate various mechanisms by which convective cloud properties can be altered. They also give valuable information about avenues for the future development and validation of both convective cloud process models and convective parameterisations.

As spatial scales of convection range from thousands of kilometres for MCS to a few kilometres for individual convective plumes, while time scales of convective variability range from minutes through to seasons, the continuous nature of observations from geostationary satellites makes them ideal for investigating the temporal and spatial variability of convection.

This thesis used high temporal resolution data from the geostationary SEVIRI instrument to quantify spatial and diurnal variability in CTT retrieval biases, investigate seasonal and diurnal cycles of CTT and quantify the lifecycle of individually tracked convective cloud over large areas and periods of time.

5.1 Summary of work presented in previous chapters

Chapter 3 evaluated SEVIRI CTT from the CLAAS-2 dataset against CALIOP and attempted to quantify spatial and diurnal variability in retrieval biases. The amplitude and phase of the diurnal cycle in CTTs, as observed by SEVIRI, were also quantified. It was shown that diurnal variations in the retrieval bias are often of the same order of magnitude as the observed amplitude of the diurnal cycle in CTT. This indicates that observed diurnal cycles may be artefacts of retrieval bias in some regions. Areas, including much of the tropics, in which the observed diurnal cycle was likely to be an artefact of retrieval bias and areas, such as regions of desert, where there was insufficient data to calculate a diurnal cycle were identified.

In order to calculate retrieval biases, SEVIRI and CALIOP CTT retrievals were collocated for the whole year of 2007. A 60 minute collocation window and a COD threshold of 1.0 were used. Scenes containing both single and multi-layer cloud were included in the analysis. It was shown that mean errors in the SEVIRI retrieval vary from less than 5 K to more than 30 K across the SEVIRI disc. Mean errors also vary by up to 30 K between the CALIOP's daytime and nighttime overpasses. Despite the large errors in some regions, mean errors across the SEVIRI disc are observed to be small, at approximately 0.44 K with a standard deviation of 11.7 K. This highlights the importance of considering both spatial and diurnal variations in retrieval bias when using the CLAAS-2 dataset.

It was shown that a significant fraction of the biases found in this analysis may be due to the difference between the radiometric cloud tops observed by SEVIRI and the physical cloud tops observed by CALIOP. Previous studies indicate that, even for optically thick clouds, biases of less than 0.5-3.0 km (approximately 3-20 K) could be explained by this difference (Sect. 2.2.2).

It was also shown that the small negative bias observed over the southeast Atlantic Ocean is likely to be related to uncertainties introduced into the retrieval by the use of models to estimate the vertical placement of clouds in the presence of low level thermal inversions. Under these circumstances, the SEVIRI retrieval generally places the cloud top above the inversion, while the CALIOP retrieval is based on direct observations of CTH and therefore not subject to the same uncertainty.

Further biases identified in Section 3 may be due to retrieval biases included in the CLAAS-2 SEVIRI dataset, although it was outside of the scope of this study to identify any such problems.

Keeping these uncertainties in mind, the seasonal, diurnal and spatial variation of CTT were quantified across the SEVIRI disc. The seasonal mean amplitude and phase of the diurnal cycle in CTT were calculated and it was shown that SEVIRI is able to capture a detailed view of the diurnal cycle of convective cloud across several continents. Observations of the diurnal cycle in CTT are shown to be accurate in regions of stratiform cloud, where retrieval biases are small and exhibit limited spatial and temporal variability. These regions include the southeast Atlantic Ocean and much of Europe. Retrieval biases are more variable over the tropics and desert regions and it is therefore more difficult to quantify the diurnal cycle in CTT in these regions.

The relationship between the diurnal cycle of CTT and retrieval biases were examined in more detail within three regions: the southeast Atlantic Ocean, Sahara desert and central Africa. In the southeast Atlantic, retrieval biases were shown to be small enough to detect a persistent diurnal cycle of approximately 5 K. Cold cloud was observed to peak between 11:00 and 15:00 LST. However, over the Sahara, the CLAAS-2 dataset was shown to be of limited skill in measuring the diurnal cycle of CTT. This may be due to limited cloud occurrence in the region and potentially due to the dominant presence of optically thin clouds in the region. Variability in the retrieval bias appears to contribute to an excessively large observed amplitude and a large amount of spatial and seasonal variability in the phase of the diurnal cycle in CTT over the Sahara. In tropical regions such as central Africa the signal from a strong observed diurnal cycle appears to be dampened by a relatively large diurnal variability in retrieval biases. Cold cloud was consistently observed to peak between 20:00 and 22:00 LST in this area.

This study highlights the importance of considering spatial and diurnal variations in retrieval errors when using data from the CLAAS-2 CTT retrieval. However, observations from passive imagers in geostationary orbit provide valuable observations of the spatial and temporal variability of cloud on scales which are not observed by polar-orbiting satellites. The results presented in this study should therefore be seen as guidance for the observation and modelling communities when using cloud top property retrievals from SEVIRI. Particularly those studies considering the diurnal cycle of cloud top properties.

While the majority of previous studies of the lifecycle of convective clouds are based on static datasets, or limited to a small area, or period of time, new convection-tracking tools, using the high time-resolution data available from SEVIRI make it possible to study the lifecycle of individual convective cloud objects. Chapter 4 examined the lifecycle of convective clouds in a Lagrangian framework, by individually tracking convective cloud cores and anvils. The distributions, diurnal cycles, lifecycles and spatial and seasonal cycles of a number of properties were quantified.

Clouds were tracked across continental sub-Saharan Africa at 15 minute intervals, during the months of March, June, September and December 2007. The cloud tracking algorithm Cb-TRAM was used to detect and track convective cloud 'cores', where cores were defined as regions of contiguous convective updraft (Sect. 4.2). A watershedding algorithm was used in combination with information from the Cb-TRAM cloud tracker, a cloud mask from the CLAAS-2 cloud product and a brightness temperature threshold to detect 'anvils'. Anvils were therefore defined as regions of cold cloud associated with each of the stage three cores tracked by Cb-TRAM (Sect. 4.2). The resulting dataset contained over 1 million tracked cloud cores and over 200,000 anvils.

The majority of clouds were tracked for periods of less than an hour, likely corresponding to single celled convective clouds (Galvin 2015), with a small fraction persisting for up to a day, likely corresponding to MCSs (Houze 2004).

It was shown that the seasonal and spatial patterns of the number of tracked cloud cores mirrors those of the mean CLAAS-2 CTT retrieval shown in Fig. 3.1 across sub-Saharan Africa. These patterns are likely due to the seasonal migration of the ITCZ and hence the intensity of convective activity (Waliser and Gautier 1993; Yang and Slingo 2001; Schröder et al. 2009).

The diurnal cycle in convection was shown two have two peaks, in the morning and evening. In the morning, the mean core area per cloud core reaches a maximum at around 05:00 LST, while the number of cores initiated peaks between 04:00 and 09:00 LST, with the total number of cores detected peaking at around 06:00 LST. In the evening, the number of cores detected reaches a maximum at around 15:00 LST, with the number of initiating cores, as well as mean core and anvil area per cloud object, peaking at 18:00 LST.

As observed by previous studies (Nesbitt and Zipser 2003; Schröder et al. 2009), mean anvil area per cloud object begins growing in the early afternoon, peaking overnight. Total anvil coverage reaches a minimum at around 11:00 LST and peaks at around 18:00 LST.

These results are in agreement with previous studies which have observed a late afternoon peak in convection over land (Yang and Slingo 2001; Liu and Zipser 2005; Zipser et al. 2006; Schröder et al. 2009) and an early morning peak over the ocean. However, the early morning peak in convective activity quantified in this study has not generally been observed by previous studies. This peak may be related to nighttime radiative cooling, the invigoration of convection by land-sea breezes in coastal regions (Desbois et al. 1988), or the presence of MCSs which persist through the night (Nesbitt and Zipser 2003).

As discussed in Section 2.3.2, the variability of convective lifecycles, including such properties as time of convective initiation, cloud lifetime and speed of development have not been well characterised. While previous studies have quantified the lifecycle of convection using data from polar-orbiting satellites, or spatially and temporally limited cloud tracking datasets, this study has quantified the properties of tracked convective cloud cores and anvils throughout their lifetime, across a large area and period of time. These results provide valuable information about avenues for future development and validation of both convective cloud process models and convective parameterisations.

5.2 Recommendations for future work

The work presented in Section 4 measures the lifetime and the horizontal and vertical extent of deep convection. While an individual long-lived convective cloud would be expected to have a larger radiative impact than a short-lived cloud, it was observed that short-lived convective events far outnumber those which persist for several hours. This dataset could therefore be used to compare the impacts of short and long-lived convection on the global energy budget.

The effect of aerosols on convection remains a significant source of uncertainty. A number of potential mechanisms by which aerosols can interact with convective cloud have been suggested and correlations between satellite retrievals of aerosol and cloud properties observed (Twomey 1977; Andreae et al. 2004; Albrecht 1989; Rosenfeld et al. 2008; Pincus and Baker 1994). However, recent studies suggest a significant proportion of this correlation may be due to meteorological co-variation (Grandey et al. 2013; Quaas et al. 2010).

High time-resolution data from geostationary satellites, including MSG and the more advanced Himawari-8 and Geostationary Operational Environmental Satellite - R series (GOES-R) satellites provide an opportunity to examine the effects of aerosols and meteorology on convection. Himawari-8 is located over east Asia and the western Pacific. It carries the Advanced Himawari Imager, which has 16 channels with spatial resolutions ranging from 0.5-2 km and a temporal resolution of 10 minutes, as well as a rapid-scan resolution of 2.5 minutes. The GOES-R series of satellites will cover North and South America, as well as large parts of the Atlantic and Pacific Oceans. They will carry the Advanced Baseline Imager, with 16 channels, spatial resolutions ranging from 0.5 to 2 km and temporal resolutions of 30 seconds, for a 1000 by 1000 km box, 5 minutes over the continental United States and 15 minutes over the full disc. While data from MSG is useful for studying convection and aerosol-convection interactions, the higher resolution and availability of new channels of the new generation of geostationary satellites will provide opportunities for new approaches to the study of convective cloud properties. In particular, data from GOES-R may prove interesting, due to its position over the Amazon, a region with intense convective activity, high amounts of aerosol and frequent observational campaigns.

By combining these high time-resolution datasets with cloud tracking software, aerosol effects throughout the lifecycle of individual convective clouds could be examined. Cloud tracks could be used to sample data from geostationary observations of aerosol properties, as well as polar-orbiter observations of aerosol optical depth from MODIS, TRMM and Global Precipitation Measurement (GPM) precipitation products and European Centre for Medium Range Weather Forecasting (ECMWF) reanalysis datasets. By sampling data throughout the convective cloud lifecycle, it could be possible to disentangle some aspects of aerosol convection interactions from meteorological co-variation of aerosol and cloud properties. Both the Amazon and the Congo Basin, where both intense convective activity and a large amount of biomass burning aerosol have been observed could present particularly interesting case studies.

Models fail to capture many of the properties of convective cloud variability quantified in this thesis. While the focus of this work is placed on observational analysis, rather than model validation, the weakness of model representations of convection, and the need for observational studies against which to validate model predictions are a key motivation for this thesis. Lifecycle based analysis of convective cloud properties provide new data against which to test both convective cloud process models and convective parameterisations.

There is a particular lack of observations of convective cloud properties over vast regions of the African continent. The results presented in this thesis can provide useful information for the convection modelling community, particularly those focusing on improving the representation of convection over Africa.

6 References

Albrecht, B. A., 1989: Aerosols, cloud microphysics, and fractional cloudiness. *Science*, **245**, 1,227–1,230.

Andreae, M. O., D. Rosenfeld, P. Artaxo, A. A. Costa, G. P. Frank, K. M. Longo, and M. A. F. Silva-Dias, 2004: Smoking rain clouds over the Amazon. *Science*, **303**, 1,337–1,342.

Arnaud, Y., M. Desbois, and J. Maizi, 1992: Automatic Tracking and Characterization of African Convective Systems on Meteosat Pictures. *J. Appl. Meteorol.*, **31 (5)**, 443–453.

Bain, C. L., G. Magnusdottir, P. Smyth, and H. Stern, 2010: Diurnal cycle of the Intertropical Convergence Zone in the east Pacific. *J .Geophys. Res.*, **115 (D23)**.

Bedka, K., J. Brunner, R. Dworak, W. Feltz, J. Otkin, and T. Greenwald, 2010: Objective satellite-based detection of overshooting tops using infrared window channel brightness temperature gradients. *J. Appl. Meteorol. Clim.*, **49 (2)**, 181–202.

Benas, N., S. Finkensieper, G. van Zadelhoff, T. Hanschmann, M. Stengel, and J. F. Meirink, 2016: Validation Report SEVIRI cloud products Edition 2 (CLAAS-2). Tech. rep., EUMETSAT Satellite Application Facility on Climate Monitoring, in press.

Bennartz, R. and M. Schroeder, 2012: Convective Activity over Africa and the Tropical Atlantic Inferred from 20 Years of Geostationary Meteosat Infrared Observations. *J. Climate*, **25 (1)**, 156–169.

Berthier, S., P. Chazette, J. Pelon, and B. Baum, 2008: Comparison of cloud statistics from spaceborne lidar systems. *Atmos. Chem. Phys.*, **8**, 6,965–6,977.

Boer, E. R. and V. Ramanathan, 1997: Lagrangian approach for deriving cloud characteristics from satellite observations and its implications to cloud parameterization. *J .Geophys. Res.*, **102 (D17)**, 21 383.

Bony, S., et al., 2006: How Well Do We Understand and Evaluate Climate Change Feedback Processes ? *J. Climate*, **19**, 3445–3482.

Boucher, O., et al., 2013: Clouds and Aerosols. In: Climate Change 2013: The Physical Science Basis. Contribution of Working Group I to the Fifth Assessment Report of the Intergovernmental Panel on Climate Change. *The physical science basis. Contribution of Working Group I to the Fifth Assessment Report of the Intergovernmental Panel on Climate Change*, T. Stocker, D. Qin, G.-K. Plattner, M. Tignor, S. Allen, J. Boschung, A. Nauels, Y. Xia, V. Bex, and P. Midgley, Eds., Cambridge University Press, Cambridge, United Kingdom and New York, NY, USA, 1–139.

Bouniol, D., R. Roca, T. Fiolleau, and D. E. Poan, 2016: Macrophysical, microphysical and radiative properties of tropical Mesocale Convective Systems over their life cycle. *J. Climate*, **29**, 3353–3371.

Bradski, G., 2000: The OpenCV Library, Dr. Dobb's Journal of Software Tools. URL `http://opencv-python-tutroals.readthedocs.io/en/latest/py_tutorials/py_imgproc/py_watershed/py_watershed.html`.

Buckle, C., 1996: *Weather and Climate in Africa.* 1st ed., Addison Wesley Longman, Harlow, 312 pp.

Burpee, R. W., 1972: The Origin and Structure of Easterly Waves in the Lower Troposphere of North Africa. *J. Atmos. Sci.*, **29 (1)**, 77–90.

Burpee, R. W., 1974: Characteristics of North African Easterly Waves During the Summers of 1968 and 1969. *J. Atmos. Sci.*, **31 (6)**, 1556–1570.

Carbone, R. E., J. D. Tuttle, D. A. Ahijevych, and S. B. Trier, 2002: Inferences of predictability associated with warm season precipitation episodes. *J. Atmos. Sci.*, **59 (13)**, 2033–2056.

Chalon, J., G. Jaubert, F. Roux, and J. Lafore, 1988: The west african squall line observed on 23 June 1981 during COPT 81: mesoscale structure and transports. *J. Atmos. Sci.*, **45 (19)**, 20.

Chen, S. S. and R. A. Houze, 1997: Diurnal variation and life-cycle of deep convective systems over the tropical Pacific warm pool. *Q. J. Roy. Meteor. Soc.*, **123**, 357–388.

Chong, M., P. Amayenc, G. Scialom, and J. Testuf, 1987: A tropical squall line observed during the COPT 81 experiment in west africa. Part 1: Kinematic structure inferred from dual doppler radar data. *Mon. Weather Rev.*, **115**, 25.

Cook, K. H., 1999: Generation of the African Easterly Jet and Its Role in Determining West African Precipitation. *J. Climate*, **12**, 1165–1184.

Dai, A., 2001: Global Precipitation and Thunderstorm Frequencies. Part II : Diurnal Variations. *J. Climate*, **14**, 1,112–1,128.

Deng, M., G. G. Mace, and Z. Wang, 2016: Anvil Productivities of Tropical Deep Convective Clusters and Their Regional Differences. *J. Atmos. Sci.*, **73**, 3467–3487.

Derrien, M., 2013: Algorithm Theoretical Basis Document for "Cloud Products" (CMa-PGE01 v3.2, CT-PGE02 v2.2 and CTTH-PGE03 v2.2), SAF/NWC/CDOP2/MFL/SCI/ATBD/01, Issue 3, Rev. 2.1. Tech. rep., EUMETSAT Satellite Application Facility on Nowcasting and Shortrange Forecasting, 87 pp.

Desbois, M., T. Kayiranga, B. Gnamien, S. Guessous, and L. Picon, 1988: Characterization of Some Elements of the Sahelian Climate and Their Interannual Variations for July 1983, 1984 and 1985 from the Analysis of METEOSAT ISCCP Data. *J. Climate*, **1**, 867–904.

Duvel, J. P., 1990: Convection over Tropical Africa and the Atlantic Ocean during Northern Summer. Part II: Modulation by Easterly Waves. *Mon. Weather Rev.*, **118 (9)**, 1855–1868.

Fink, A. H., 2003: Spatiotemporal variability of the relation between African Easterly Waves and West African Squall Lines in 1998 and 1999. *J .Geophys. Res.*, **108 (D11)**.

Fiolleau, T. and R. Roca, 2013a: An algorithm for the detection and tracking of tropical mesoscale convective systems using infrared images from geostationary satellite. *IEEE Trans. Geosci. Remote Sens.*, **51 (7)**, 4302–4315.

Fiolleau, T. and R. Roca, 2013b: Composite life cycle of tropical mesoscale convective systems from geostationary and low Earth orbit satellite observations: Method and sampling considerations. *Q. J. Roy. Meteor. Soc.*, **139 (673)**, 941–953.

Forster, P. M., V. Ramaswamy, and Coauthors, 2007: Changes in atmospheric constituents and in radiative forcing. *Climate change 2007: the physical science basis. Contribution of Working Group I to the Fourth Assessment Report of the Intergovernmental Panel on Climate Change*, S. Solomon et al., Ed., Cambridge University Press, Cambridge, United Kingdom and New York, NY, USA, 129–234.

Futyan, J. M. and A. D. Del Genio, 2007a: Deep Convective System Evolution over Africa and the Tropical Atlantic. *J. Climate*, **20 (20)**, 5041–5060.

Futyan, J. M. and A. D. Del Genio, 2007b: Relationships between lightning and properties of convective cloud clusters. *Geophys. Res. Lett.*, **34 (15)**, 1–5.

Galvin, J. F. P., 2015: *An introduction to the meteorology and climate of the tropics*. Wiley Blackwell, Chichester, 328 pp.

Gaye, A., A. Viltard, and P. de Félice, 2005: Squall lines and rainfall over Western Africa during summer 1986 and 87. *Meteor. Atmos. Phys.*, **90 (3-4)**, 215–224.

Goyens, C., D. Lauwaet, M. Schröder, M. Demuzere, and N. P. M. Van Lipzig, 2012: Tracking mesoscale convective systems in the Sahel: relation between cloud parameters and precipitation. *Int. J. Climatol.*, **32**, 1921–1934.

Grabowski, W. W. and J. C. Petch, 2009: Deep convective clouds. *Clouds in the Perturbed Climate System*, J. Lupp and M. Turner, Eds., Massachusets Institute of Technology and Frankfurt Institute for Advanced Studies, Cambridge, Massachusetts, 1st ed., 197–216.

Grabowski, W. W., et al., 2006: Daytime convective development over land: A model intercomparison based on LBA observations. *Q. J. Roy. Meteor. Soc.*, **132**, 317–344.

Grandey, B. S., P. Stier, R. G. Grainger, and T. M. Wagner, 2013: The contribution of the strength and structure of extratropical cyclones to observed cloud aerosol relationships. *Atmos. Chem. Phys.*, **13**, 10 689–10 701.

Gray, W. M. and R. W. Jacobsen, 1977: Diurnal variation of deep cumulus convection. *Mon. Weather Rev.*, **105**, 1,171–1,188.

Grist, J. P. and S. E. Nicholson, 2001: A Study of the Dynamic Factors Influencing the Rainfall Variability in the West African Sahel. *J. Climate*, **14 (7)**, 1337–1359.

Guichard, F., et al., 2004: Modelling the diurnal cycle of deep precipitating convection over land with cloud-resolving models and single-column models. *Q. J. Roy. Meteor. Soc.*, **130**, 3139–3172.

Halladay, K., Y. Malhi, and M. New, 2012: Cloud frequency climatology at the Andes Amazon transition: 1. Seasonal and diurnal cycles. *J. Geophys. Res.*, **117 (D23)**.

Hamann, U., et al., 2014: Remote sensing of cloud top pressure/height from SEVIRI: analysis of ten current retrieval algorithms. *Atmos. Meas. Tech. Discuss.*, **7 (1)**, 401–473.

Harrison, E. F., D. R. Brooks, P. Minnis, B. A. Wielicki, W. F. Staylor, G. G. Gibson, D. F. Young, and Frederick M. Den, 1988: First estimates of the diurnal variation of longwave radiation from the multiple-satellite Earth radiation budget experiment (ERBE). *B. Am. Meteorol. Soc.*, **69 (10)**, 1144–1151.

Harrison, E. F., P. Minnis, B. R. Barkstrom, V. Ramanathan, R. D. Cess, and G. G. Gibson, 1990: Seasonal Variation of Cloud Radiative Forcing Derived From the Earth Radiation Budget Experiment. *J .Geophys. Res.*, **95703 (20)**, 687–18.

Heidinger, A. K. and M. J. Pavolonis, 2009: Gazing at Cirrus Clouds for 25 Years through a Split Window. Part I: Methodology. *J. Appl. Meteorol. Clim.*, **48 (6)**, 1100–1116.

Hendon, H. H. and K. Woodberry, 1993: The diurnal cycle of tropical convection. *J .Geophys. Res.*, **98 (D9)**.

Heymsfield, G. M., J. D. Spinhirne, and R. Fulton, 1991: Aircraft overflight measurements of midwest severe storms. Implications on geosynchronous satellite interpretations. *Mon. Weather Rev.*, 436–456.

Higgins, G., A. Kassam, J. Kowal, S. Sarraf, H. Arnoldussen, M. Frere, J. Hrabovszki, and H. van Velthuizen, 1978: Report on the agroecological zones project. Vol.1 Methodology and results for Africa. World soil resources report No 48. Tech. rep., AGLS, Food and Agriculture Organization of the United Nations, Rome, Italy.

Houze, R. a., 2004: Mesoscale Convective Systems. *Rev. Geophys.*, **42**, 1–43.

Houze, R. A., S. S. Chen, D. E. Kingsmill, Y. Serra, and S. E. Yuter, 2000: Convection over the Pacific Warm Pool in relation to the Atmospheric Kelvin-Rossby Wave. *J. Atmos. Sci.*, **57 (18)**, 3058–3089.

Houze, R. A., J., 1993: *Cloud Dynamics.* Academic Press, San Diego, California, 573 pp.

Hsieh, J.-S. and K. H. Cook, 2005: Generation of African Easterly Wave Disturbances: Relationship to the African Easterly Jet. *Mon. Weather Rev.*, **133 (5)**, 1311–1327.

Igel, M. R., A. J. Drager, and S. C. van den Heever, 2014: A CloudSat cloud object partitioning technique and assessment and integration of deep convective anvil sensitivities to sea surface temperature. *J .Geophys. Res.*, **119 (17)**, 10 515–10 535.

Igel, M. R. and S. C. van den Heever, 2015: The relative influence of environmental characteristics on tropical deep convective morphology as observed by CloudSat. *J. Geophys. Res.*, **120**, 4304–4322.

Janowiak, J. E., P. A. Arkin, and M. Morrissey, 1994: An examination of the diurnal cycle in oceanic tropical rainfall using satellite and in situ data. *Mon. Weather Rev.*, **122**, 2,296–2,311.

Kanamitsu, M. and T. N. Krishnamurti, 1977: Northern Summer Tropical Circulation During Drought and Normal Rainfall Months. *Mon. Weather Rev.*, **106**, 331.

King, M. D., D. D. Herring, and D. J. Diner, 1995: The Earth observing system: a space-based progem for assessing mankind's impact ont eh global environment. *Optics and Photonics*, **6**, 34–39.

Kniffka, A., M. Lockhoff, M. Stengel, and J. F. Meirink, 2013: Validation Report - SEVIRI cloud products, SAF/CM/DWD/VAL/SEV/CLD Issue 1, Rev. 1.2. Tech. rep., EUMETSAT Satellite Application Facility on Climate Monitoring, 88 pp.

Kohler, H., 1936: The nucleus in and the growth of hygroscopic droplets. *T. Faraday Soc.*, **32**, 1152–1161.

Kummerow, C., W. Barnes, T. Kozu, J. Shiue, and J. Simpson, 1998: The tropical rainfall measuring mission(TRMM) sensor package. *J. Atmos. Ocean Tech.*, **15 (3)**, 809–817.

Leroux, M., 1983: *The Meteorology and Climate of Tropical Africa.* 1st ed., Praxis, Chichester, 486 pp.

Levizzani, V., F. Pinelli, M. Pasqui, S. Melani, A. G. Laing, and R. E. Carbone, 2010: A 10-year climatology of warm-season cloud patterns over Europe and the Mediterranean from Meteosat IR observations. *Atmos. Res.*, **97 (4)**, 555–576.

Liu, C. and E. J. Zipser, 2005: Global distribution of convection penetrating the tropical tropopause. *J .Geophys. Res.*, **110 (23)**, 1–12.

Loeb, N. G., B. A. Wielicki, D. R. Doelling, G. L. Smith, D. F. Keyes, S. Kato,

N. Manalo-Smith, and T. Wong, 2009: Toward optimal closure of the Earth's top-of-atmosphere radiation budget. *J. Climate*, **22 (3)**, 748–766.

Lohmann, U., J. Quaas, S. Kinne, and J. Feichter, 2007: Different Approaches for Constraining Global Climate Models of the Anthropogenic Indirect Aerosol Effect. *B. Am. Meteorol. Soc.*, **88**, 243–249.

Mannstein, H., T. Zinner, A. Tafferener, C. Forster, J. Schroettle, and D. Merk, 2013: Cb-TRAM: cumulonimbus tracking and monitoring (V. 32b). DLR Oberpfaffenhofen, LMU MIM, Munich.

Mayaux, P., et al., 2003: A land cover map of Africa. Tech. rep., European Comission, 56 pp.

McCollum, J. R., A. Gruber, and M. B. Ba, 2000: Discrepancy between Gauges and Satellite Estimates of Rainfall in Equatorial Africa. *J. Appl. Meteorol.*, **39 (5)**, 666–679.

Meisner, B. N. and P. A. Arkin, 1987: Spatial and annual variations in the diurnal cycle of large-sacle tropical convective cloudiness and precipitation. *Mon. Weather Rev.*, **115**, 2,009–2,032.

Menzel, W. P., T. R. Stewart, and W. L. Smith, 1983: Improved cloud motion wind vector and altitude assignment using VAS. *J. Clim. Appl. Meteorol.*, **22**, 377–384.

Merk, D. and T. Zinner, 2013: Detection of convective initiation using Meteosat SEVIRI: implementation in and verification with the tracking and nowcasting algorithm Cb-TRAM. *Atmos. Meas. Tech.*, **6**, 1903–1918.

Minnis, P., C. R. Yost, S. Sun-Mack, and Y. Chen, 2008: Estimating the top altitude of optically thick ice clouds from thermal infrared satellite observations using CALIPSO data. *Geophys. Res. Lett.*, **35 (April)**, 1–6.

NASA, 2004: PIA04965: SRTM Data Release for Africa, Colored Height. URL `http://photojournal.jpl.nasa.gov/catalog/pia04965`.

NASA, 2013: CALIPSO: Data User's Guide - Data Product Descriptions - Lidar Level 2 Cloud and Aerosol Layer Products. URL `http://www-calipso.larc.nasa.gov/resources/calipso_users_guide/data_summaries/layer/index.php`.

Nesbitt, S. W. and E. J. Zipser, 2003: The Diurnal Cycle of Rainfall and Convective Intensity according to Three Years of TRMM Measurements. *J. Climate*, **16**, 1,456–1,475.

Nicholson, S. E., 2001: Climatic and environmental change in Africa during the last two centuries. *Clim. Res.*, **17**, 123–144.

Nicholson, S. E., 2009: A revised picture of the structure of the âĂIJmonsoonâĂİ and land ITCZ over West Africa. *Clim. Dynam.*, **32**, 1155–1171.

Nicholson, S. E., A. I. Barcilon, M. Challa, and J. Baum, 2007: Wave Activity on the Tropical Easterly Jet. *J. Atmos. Sci.*, **64 (7)**, 2756–2763.

Norris, J. R. and A. Slingo, 2009: Trends in observed cloudiness and Earth's radiative budget. *Clouds in the Perturbed Climate System*, J. Lupp and M. Tuner, Eds., Massachusets Institute of Technology and Frankfurt Institute for Advanced Studies, Cambridge, Massachusetts, 1st ed., 17–36.

Orville, R., 1981: Global Distribution of Midnight Lighting - September to November 1977. *Mon. Weather Rev.*, **109**, 5.

Peng, J., Z. Li, H. Zhang, J. Liu, and M. Cribb, 2016: Systematic Changes in Cloud Radiative Forcing with Aerosol Loading for Deep Clouds in the Tropics. *J. Atmos. Sci.*, **73 (1)**, 231–249.

Peng, J., H. Zhang, and Z. Li, 2014: Temporal and spatial variations of global deep cloud systems based on CloudSat and CALIPSO satellite observations. *Adv. Atmos. Sci.*, **31 (3)**, 593–603.

Pfeifroth, U., J. Trentmann, A. H. Fink, and B. Ahrens, 2016: Evaluating satellite-based diurnal cycles of precipitation in the African tropics. *J. Appl. Meteorol. Clim.*, **55 (1)**, 23–39.

Pincus, R. and M. B. Baker, 1994: Effect of precipitation on the albedo susceptibility of clouds in the marine boundary layer. *Nature*, **372**, 250–252.

Pope, M., C. Jakob, and M. J. Reeder, 2008: Convective Systems of the North Australian Monsoon. *J. Climate*, **21 (19)**, 5091–5112.

Posselt, D. J., G. L. Stephens, and M. Miller, 2008: CLOUDSAT: Adding a new dimension to a classical view of extratropical cyclones. *B. Am. Meteorol. Soc.*, **89 (5)**, 599–609.

Quaas, J., B. Stevens, P. Stier, and U. Lohmann, 2010: Interpreting the cloud cover aerosol optical depth relationship found in satellite data using a general circulation model. *Atmos. Chem. Phys.*, **10 (13)**, 6129–6135.

Randall, D. A., Harshvardhan, and D. A. Dazlich, 1991: Diurnal Variability of the Hydrologic Cycle in a General Circulation Model. *J. Atmos. Sci.*, **48 (1)**, 40–62.

Redelsperger, J., C. D. Thorncroft, A. Diedhiou, T. Lebel, D. J. Parker, and J. Polcher, 2006: African Monsoon Multidisciplinary Analysis: An International Research Project and Field Campaign. *B. Am. Meteorol. Soc.*, **87**, 1,739–1,746.

Reed, R. J., D. C. Norquist, and E. E. Recker, 1977: The structure and properties of African wave disturbances as observed during phase II of GATE. *Mon. Weather Rev.*, **105**, 317–333.

Rennó, N. O., et al., 2013: CHASER: An Innovative Satellite Mission Concept to

Measure the Effects of Aerosols on Clouds and Climate. *B. Am. Meteorol. Soc.*, **94**, 685–694.

Reuter, M., W. Thomas, P. Albert, M. Lockhoff, R. Weber, K.-G. Karlsson, and J. Fischer, 2009: The CM-SAF and FUB Cloud Detection Schemes for SEVIRI: Validation with Synoptic Data and Initial Comparison with MODIS and CALIPSO. *J. Appl. Meteorol. Clim.*, **48**, 301–316.

Rickenbach, T., R. N. Ferreira, N. Guy, and E. Williams, 2009: Radar-observed squall line propagation and the diurnal cycle of convection in Niamey, Niger, during the 2006 African monsoon and multidisciplinary analyses intensive observing period. *J. Geophys. Res.*, **114 (3)**, 1–8.

Rosenfeld, D., U. Lohmann, G. B. Raga, C. D. O'Dowd, M. Kulmala, S. Fuzzi, A. Reissell, and M. O. Andreae, 2008: Flood or drought: how do aerosols affect precipitation? *Science*, **321**, 1,309–1,313.

Rosenfeld, D., E. Williams, M. O. Andreae, E. Freud, U. Pöschl, and N. O. Rennó, 2012: The scientific basis for a satellite mission to retrieve CCN concentrations and their impacts on convective clouds. *Atmos. Meas. Tech.*, **5**, 2,039–2,055.

SAFNWC/MSG, 2012: Algorithm Theoretical Basis Document for "Cloud Products" (CMa-PGE01 v3.2, CT-PGE02 v2.2 and CTTH-PGE03 v2.2) SAF/NWC/CDOP/MFL/SCI/ ATBD/01, Issue 3, Rev. 2. Tech. rep., NWC-SAF.

Sato, T., H. Miura, M. Satoh, Y. N. Takayabu, and Y. Wang, 2009: Diurnal Cycle of Precipitation in the Tropics Simulated in a Global Cloud-Resolving Model. *J. Climate*, **22**, 4809–4826.

Schmetz, J., K. Holmlund, J. Hoffman, B. Strauss, B. Mason, V. Gaertner, A. Koch, and L. Van De Berg, 1993: Operational Cloud-Motion Winds from Meteosat Infrared Images. *J. Appl. Meteorol.*, **32**, 1206–1225.

Schröder, M., M. König, and J. Schmetz, 2009: Deep convection observed by the Spinning Enhanced Visible and Infrared Imager on board Meteosat 8: Spatial distribution and temporal evolution over Africa in summer and winter 2006. *J. Geophys. Res.*, **114 (D5)**, D05 109.

Seinfeld, J. H. and S. N. Pandis, 2006: *Atmospheric Chemistry and Physics: From Air Pollution to Climate Change.* 2d ed., Wiley-Interscience, New York, 1232 pp.

Sherwood, S. C., J. H. Chae, P. Minnis, and M. McGill, 2004: Underestimation of deep convective cloud tops by thermal imagery. *Geophys. Res. Lett.*, **31**, 1–4.

Smith, W. L. and C. M. R. Platt, 1978: Comparison of Satellite-Deduced Cloud Heights with Indications from Radiosonde and Ground-Based Laser Measurements. *J. Appl. Meteorol.*, **17**, 1796–1802.

Stengel, M. S., A. K. Kniffka, J. F. M. Meirink, M. L. Lockhoff, J. T. Tan, and R. H. Hollmann, 2014: CLAAS: The CM SAF cloud property data set using SEVIRI. *Atmos. Chem. Phys.*, **14**, 4297–4311.

Stephens, G. L., et al., 2002: the Cloudsat Mission and the a-Train. *Bulletin of the American Meteorological Society*, **83 (12)**, 1771–1790, doi: 10.1175/BAMS-83-12-1771, URL `http://journals.ametsoc.org/doi/abs/10.1175/BAMS-83-12-1771`.

Stratton, R. A. and A. J. Stirling, 2012: Improving the diurnal cycle of convection in GCMs. *Q. J. Roy. Meteor. Soc.*, **138 (666)**, 1121–1134.

Stubenrauch, C. J., S. Cros, A. Guignard, and N. Lamquin, 2010: A 6-year global cloud climatology from the Atmospheric InfraRed Sounder AIRS and a statistical analysis in synergy with CALIPSO and CloudSat. *Atmos. Chem. Phys.*, **10**, 7,197–7,214.

Stubenrauch, C. J., et al., 2013: Assessment of global cloud datasets from satellites: Project and database initiated by the GEWEX radiation panel. *B. Am. Meteorol. Soc.*, **94 (November 2012)**, 1031–1049.

Sylla, M. B., E. Coppola, L. Mariotti, F. Giorgi, P. M. Ruti, A. Dell'Aquila, and X. Bi, 2009: Multiyear simulation of the African climate using a regional climate model (RegCM3) with the high resolution ERA-interim reanalysis. *Clim. Dynam.*, **35**, 231–247.

Tadesse, A. and E. N. Anagnostou, 2010: African convective system characteristics determined through tracking analysis. *Atmos. Res.*, **98 (2-4)**, 468–477.

Taylor, S., P. Stier, B. White, S. Finkensieper, and M. Stengel, 2017: Evaluating the diurnal cycle in cloud top temperature from SEVIRI. *Atmos. Chem. Phys.*, **17**, 7035–7053.

Thomson, S. W., 1871: On the equilibrium of vapour at a curved surface of liquid. *Philos. Mag.*, **4**, 448–452.

Trenberth, K. E., J. T. Fasullo, and J. Kiehl, 2009: Earth's Global Energy Budget. *B. Am. Meteorol. Soc.*, **90 (3)**, 311–323.

Twomey, S., 1977: The influence of pollution on the shortwave albedo of clouds. *J. Atmos. Sci.*, **34**, 1,149–1,152.

Vaughan, M. A., et al., 2009: Fully Automated Detection of Cloud and Aerosol Layers in the CALIPSO Lidar Measurements. *J. Atmos. Ocean Tech.*, **26 (10)**, 2034–2050.

Venugopal, V., K. Virts, J. Sukhatme, J. M. Wallace, and B. Chattopadhyay, 2016: A comparison of the fine scale structure of the diurnal cycle of tropical rain and lightning. *Atmos. Res.*, **169**, 515–522.

Vondou, D. A., A. Nzeukou, and F. M. Kamga, 2010: Diurnal cycle of convective activity over the West of Central Africa based on Meteosat images. *Int. J. Appl. Earth Obs.*, **12**, 58–62.

Waliser, D. E. and C. Gautier, 1993: A satellite-derived climatology of the ITCZ. *J. Climate*, **6**, 2,162–2,174.

Wallace, J. M., 1975: Diurnal variations in precipitation and thunderstorm frequency over the contermonous United States. *Mon. Weather Rev.*, **103**, 406–419.

Washington, R., R. James, H. Pearce, W. M. Pokam, and W. Moufouma-okia, 2013: Congo Basin rainfall climatology: can we believe the climate models? *Phil. Trans. R. Soc. B*, **368**.

Wild, M., et al., 2014: The energy balance over land and oceans: an assessment based on direct observations and CMIP5 climate models. *Clim. Dynam.*, **44**, 3393–3429.

Williams, E. and S. Stanfill, 2002: The physical origin of the land-ocean contrast in lightning activity. *C. R. Phys.*, **3 (10)**, 1277–1292.

Williams, M. and R. A. Houze, 1987: Satellite-Observed Characteristics of Winter Monsoon Cloud Clusters. *Mon. Weather Rev.*, **115 (2)**, 505–519.

Winker, D. M., C. A. Hostetler, M. A. Vaughan, and A. H. Omar, 2006: CALIOP algorithm theoretical basis document. Part 1: CALIOP instrument , and algorithms overview. Tech. rep., NASA, 29 pp.

Winker, D. M., M. A. Vaughan, A. H. Omar, Y. Hu, and K. A. Powell, 2009: Overview of the CALIPSO Mission and CALIOP Data Processing Algorithms. *J. Atmos. Ocean Tech.*, **26**, 2310–2323.

Wood, R., et al., 2011: The VAMOS Ocean-Cloud-Atmosphere-Land Study

Regional Experiment (VOCALS-REx): goals, platforms, and field operations. *Atmos. Chem. Phys.*, **11**, 627–654.

Yang, G.-Y. and J. Slingo, 2001: The Diurnal Cycle in the Tropics. *Mon. Weather Rev.*, **129**, 784–801.

Yang, J., et al., 2013: The role of satellite remote sensing in climate change studies. *Nat. Clim. Change*, **3 (10)**, 875–883.

Yang, S., K.-S. Kuo, and E. A. Smith, 2008: Persistent Nature of Secondary Diurnal Modes of Precipitation over Oceanic and Continental Regimes. *J. Climate*, **21**, 4115–4131.

Yin, X., S. Nicholson, and M. Ba, 2000: On the diurnal cycle of cloudiness over Lake Victoria and its influence on evaporation from the lake. *Hydrolog. Sci. J.*, **45 (3)**, 407–424.

Yuan, J. and R. a. Houze, 2010: Global Variability of Mesoscale Convective System Anvil Structure from A-Train Satellite Data. *J. Climate*, **23 (21)**, 5864–5888.

Zinner, T., H. Mannstein, and A. Tafferner, 2008: Cb-TRAM: Tracking and monitoring severe convection from onset over rapid development to mature phase using multi-channel Meteosat-8 SEVIRI data. *Meteor. Atmos. Phys.*, **101**, 191–210.

Zipser, E., 2003: Some Views On 'Hot Towers' after 50 Years of Tropical Field Programs and Two Years of TRMM Data. *Meteor. Mon.*, **51**, 49–58.

Zipser, E. J., 1969: The role of organized unsaturated convective downdrafts in teh straucture and rapid decay of an equatorial disturbance. *J. Appl. Meteorol.*, **8**, 799–814.

Zipser, E. J., 1977: Mesoscale and Convective-Scale Downdrafts as Distinct Components of Squall-Line Structure. *Mon. Weather Rev.*, **105 (12)**, 1568–1589.

Zipser, E. J., C. Liu, D. J. Cecil, S. W. Nesbitt, and D. P. Yorty, 2006: Where Are the Most Intense Thunderstorms on Earth? *B. Am. Meteorol. Soc.*, **87 (8)**, 1057–1071.